Towards proton exchanged quantum wires and highly confining integrated circuits on LiNbO3

Oleksandr Stepanenko

Université Nice Sophia Antipolis

École Doctorale : Science Fondamentales et Appliqué (ED n°364)

Thèse

pour obtenir le titre de

Docteur en Sciences

de l'Université Nice Sophia Antipolis

dans specialité : Physique

par

Oleksandr Stepanenko

Towards Proton Exchanged Quantum Wires and highly confining Integrated Circuits on $LiNbO_3$

Thèse dirigée par Marc De Micheli

preparée au Laboratoire de Physique de la Matière Condensée

soutenue le 18 décembre 2013

Jury :

Président :	Giuseppe Leo	-	Professeur, Université Paris Diderot - Paris 7
Rapporteurs :	Henri Porte	-	Directeur de Recherche CNRS, PDG Photline Technologies (Besançon)
	Lionel Duvillaret	-	Professeur, INP Grenoble, PDG Kapteos (Le Bourget-du-Lac)
Examinateurs :	Sébastien Tanzilli	-	Chargé de Recherche CNRS, Université Nice Sophia Antipolis
	Pascal Baldi	-	Professeur, Université Nice Sophia Antipolis
Directeur :	Marc De Micheli	-	Directeur de Recherche, Université Nice Sophia Antipolis

"I will never be a physicist!"

Me at 15 years.

Acknowledgements

This work took place in the Laboratoire de Physique de la Matière Condensée in Nice during 2010-2013 years and was financed by the ANR in the frame of the phoXcry project (ANR-09-NANO-004-03).

I would like to say a great thanks to Fabrice Mortessagne, the director of the laboratory, for accepting me to the laboratory and creating such pleasant and friendly conditions for research.

I express my deep gratitude to Marc De Micheli, my research supervisor for the possibility to work in his team and research area. I would like to thank you for your patient guidance, openness to all kind of questions, enthusiastic encouragement and useful critiques. It was a great pleasure to work with you as you have become one of the few persons whose qualities inspire me.

I would like to extend my sincerest thanks and appreciation to Giuseppe Leo, Pascal Baldi and Sébastien Tanzilli for accepting the proposition to be members of the Jury and their interest to my work. I also thank Henri Porte and Lionel Duvillaret for taking the responsibility of being the referees.

This work has been done in collaboration with many people from our laboratory as well as from others. I would therefore like to say a great thanks to those who impacted their efforts, patience, inspiration and their time into this a really very active and interesting research work.

I am particularly grateful to Pascal Baldi for numerous discussions and constructive critiques during all my work here at LPMC. Sincerely, I have always thought you are my second supervisor.

What would have I done without the essential support by Pierre Aschiéri? As this work was mainly experimental, your simulation applets saved a lot of time and were indispensable.

Now, I would like to offer my special thanks to a person who worked closely with me almost every day. Emmanuel Quillier, you are one of the first who familiarized me with most of the experimental techniques and issues. You are an engineer with limitless energy, you never said “no” and helped me without any questions.

I say a great thanks to Hervé Tronche and Florent Doutre, engineers in our team, for their systematic helps during my PhD work.

I would like to express my appreciation to Sarah Benchabane from FEMTO-ST in Besançon for a close collaboration in terms of the project PhoXcry. I thank also Jérôme Bourderionnet at Thales Research and Technology for his help in characterizations of our samples.

I wish to acknowledge the help provided in X-ray characterizations of our waveguides by Maud Nemoz from CRHEA in Sophia Antipolis.

I thank our Russian colleagues, Sergey Kostritskii and his research team, for measurement of electro-optical coefficients of our samples.

I appreciate the help provided by Hervé Rigneault from Fresnel Institute for nonlinear optical characterizations.

I thank people from the secrétariat of our laboratory, Christine Boudard-Morteau, Christine Chassagneux and especially Nathalie Koulechoff for their help in administrative questions.

Also I want to thank my bureau colleagues, Geoffroy Kirstetter and Alphonse Leroux for the great working atmosphere over these three years.

I would like to express my thanks to Maryse De Micheli, not only for being a good French teacher but also for being a great person.

I express my deep gratitude to Christophe Raufaste, the kindest person I have ever met, for his support, a great studio and delicious tomatoes. Thank you for all you have done for my family.

I greatly thank my parents for giving me this nice possibility to finish my master study in France and, thus, to find this PhD proposition.

Finally, I thank Inna Krasnokutska for her enormous patience and for supporting me not only as my wife but also as a colleague.

Contents

Acknowledgements v

Résumé détaillé 1

Genesis of the realized work 7

1 Proton exchanged waveguides on $LiNbO_3$: state of the art 13
1.1 Lithium Niobate . . . 13
1.1.1 Crystallographic orientations of $LiNbO_3$ . . . 15
1.2 Proton exchange . . . 16
1.2.1 Principles and experimental techniques of proton exchange . . . 16
1.3 Variants of the proton exchange . . . 18
1.3.1 Proton Exchange . . . 18
1.3.2 Annealed Proton Exchange . . . 19
1.3.3 Soft Proton Exchange . . . 20
1.3.4 Vapor-phase Proton Exchange . . . 20
1.3.5 Reverse proton exchange . . . 21
1.4 Overview of alternative waveguide fabrication techniques on $LiNbO_3$ . . . 22
1.5 Influence of different fabrication parameters on the waveguide properties . 23
1.5.1 Influence of LB concentration on the waveguide properties . . . 23
1.5.2 Influence of temperature on the waveguide properties . . . 24
1.5.3 Kinetics of the proton exchange . . . 26
1.5.4 Influence of humidity on the waveguide properties . . . 27
1.6 Crystalline structure of proton exchanged waveguides . . . 28
1.7 Channel waveguide fabrication by proton exchange . . . 30

2 Theoretical background on nonlinear integrated optics 33
2.1 Waveguide concepts . . . 33
2.1.1 Electromagnetic modes . . . 33
2.2 Second order nonlinear interactions in proton exchanged waveguides on $LiNbO_3$ . . . 37
2.2.1 Wave equation for nonlinear optical waveguide . . . 37
2.2.2 Problem of phase-matching . . . 39
2.2.3 Quasi-Phase-Matching . . . 41
2.2.4 Measurement of SHG and SPDC efficiency . . . 42

2.2.5 Measurement of SPDC efficiency . . . 43
2.2.6 Comparison of SHG and SPDC characterization . . . 43
2.3 Calculation of the deformation induced by the proton exchange . . . 44
2.3.1 Deformations in proton exchanged layers: a quick review . . . 44
2.3.2 General definition of strain and stress . . . 45
2.3.3 Measurement of strains in PE waveguides . . . 46
2.4 Hybrid modes in waveguides fabricated on $LiNbO_3$ . . . 48

3 Highly confining waveguides on X-cut $LiNbO_3$ 51
3.1 The PhoXcry project . . . 51
3.1.1 Photonic crystal on $LiNbO_3$ . . . 52
3.1.2 Optical waveguide fabrication . . . 53
3.2 Modified proton exchange technique HISoPE . . . 53
3.2.1 Fabrication protocol . . . 53
3.3 Optical characterization of the planar HISoPE waveguides . . . 57
3.3.1 Index profile . . . 57
3.3.2 Reproducibility . . . 59
3.3.3 Hybrid modes . . . 60
3.3.4 Surface SHG characterization . . . 62
3.4 Channel HISoPE waveguide fabrication . . . 64
3.5 Optical characterization of the channel HiSoPE waveguides . . . 67
3.5.1 M-lines . . . 67
3.5.2 Propagation losses . . . 68
3.5.3 Hybrid modes in channel waveguides . . . 69
3.5.4 Transmission spectra of nanostructured micro waveguides . . . 72
3.6 Discussion and Perspectives . . . 75

4 Highly confining waveguides on Z-cut $LiNbO_3$ 77
4.1 HISoPE technique applied to Z-cut $LiNbO_3$ wafers . . . 77
4.1.1 High loss optical modes in HISoPE waveguides . . . 77
4.2 Crystalline structure of Z-cut $LiNbO_3$ waveguides . . . 80
4.2.1 SPE waveguides . . . 81
4.2.2 PE waveguides . . . 82
4.2.3 HISoPE waveguides . . . 83
4.3 Nonlinear optical characterizations of planar waveguides . . . 88
4.3.1 Surface SHG profiling . . . 88
4.3.2 SHG imaging by confocal microscopy . . . 91
4.3.3 Measurement of the electro-optical coefficient by absorption . . . 92
4.4 Channel HISoPE waveguides . . . 93
4.4.1 Propagation losses . . . 93
4.4.2 Hybrid modes . . . 93
4.4.3 SHG imaging of HISoPE channel waveguides . . . 95
4.5 Buried proton exchanged waveguides . . . 97
4.5.1 Propagation losses of the buried waveguides . . . 98
4.5.2 Near field mode observation . . . 99
4.5.3 SHG in buried waveguides . . . 100
4.5.4 Spontaneous parametric down conversion . . . 102

4.6 Kinetics of RPE 102
4.7 Discussion and perspectives 104

General conclusions **109**

A Characterization of the index profile of waveguides **111**
A.1 M-lines technique 111
A.2 Index profile reconstruction 115

B Propagation losses measurements in waveguides **117**

C Surface SHG probing technique **119**

List of abbreviations **121**

Author's references **123**

Bibliography **125**

Dedicated to my family

Résumé détaillé

Depuis les années 1970, le niobate de lithium ($LiNbO_3$) a été utilisé pour fabriquer des guides d'onde optiques avec la possibilité de réaliser des modulateurs efficaces et des convertisseurs de fréquence en utilisant l'effet électro-optique et les propriétés non linéaires du cristal.[1–5] La première technique proposée et exploitée pour fabriquer des guides d'onde sur $LiNbO_3$ était une diffusion de métal (principalement de titane), qui permet la création d'un guide d'onde à gradient d'indice à la surface du cristal avec une augmentation d'indice maximum de l'ordre de 0,02 à la longueur d'onde 633 nm.[6,7]

L'échange protonique fut proposé au début des années 1980 et a relancé la recherche en optique intégrée (Integrated Optics, IO) sur niobate de lithium.[5,8–10] Cette technique consiste à plonger le cristal dans un bain d'acide fondu pour remplacer une partie des ions lithium du cristal par des protons. Ce processus induit une augmentation de l'indice extraordinaire du substrat, qui permet de réaliser un guide d'onde optique pour cette polarisation. Selon l'acidité du bain utilisé comme source de protons, et sa température, on peut réaliser des guides d'onde avec des profils d'indice très différents.

Il a été rapidement établi, que les guides d'onde fabriqués en utilisant des sources de protons concentrées ont un profil à saut d'indice avec une augmentation d'indice extraordinaire élevé de 0,1 à la longueur d'onde de 633 nm. Ces guides ont très vite suscité un vif intérêt, puisqu'une augmentation d'indice élevé permet de réaliser des virages serrés sans trop de pertes et, donc, des circuits intégrés optiques denses. Malheureusement, ces guides présentaient également une réduction dramatique des coefficients électro-optiques et non linéaires, ce qui explique que l'intérêt a décrut.[11–15]

Néanmoins, quelques modifications du protocole de fabrication, telles que l'ajout d'un recuit après la phase d'échange protonique ou la réduction de l'acidité du bain, ont permis la réalisation de guides utiles appelés APE[16] et SPE[17,18], acronymes formés sur les noms anglais : Annealed Proton Exchange et Soft Proton Exchange. Ces guides d'onde présentent des propriétés électro-optiques et non linéaires préservées et un profil à gradient d'indice avec une variation d'indice $\approx 0{,}03$. Ils sont particulièrement adaptés pour la réalisation des dispositifs fonctionnant dans le proche infrarouge ($\lambda = 800$ nm),

car ils sont moins sensibles aux dommages photoréfractifs que les guides réalisés par diffusion de titane.[19–21]

Au LPMC, nous sommes principalement intéressés par des composants optiques non linéaires et un bon moyen d'améliorer l'efficacité de ces dispositifs est de réaliser des guides d'ondes intégrés. Cependant, les guides d'ondes de surface présentent un profil d'indice asymétrique. Le contraste d'indice entre l'air et un guide d'onde est bien plus élevé que le contraste entre le guide et le substrat de $LiNbO_3$. Un inconvénient particulier de l'asymétrie de ces guides d'onde à gradient d'indice est que les maxima d'intensités des modes à différentes longueurs d'ondes se situent à des profondeurs différentes dans le guide d'onde (figure 1).

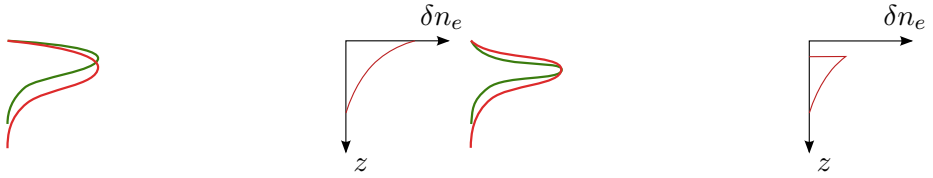

FIGURE 1: Représentation schématique de: (a) guide d'onde à gradient d'indice de surface, et (b) guide d'onde enterré.

Ceci n'est pas favorable à des interactions non linéaires, qui couplent au moins deux longueurs d'onde différentes, et dont l'efficacité est proportionnelle au recouvrement des modes en interaction. Pour symétriser les modes et, par conséquent, d'améliorer l'efficacité des interactions non linéaires on peut enterrer un guide d'onde dans le substrat. Pour ce faire, la technique d'échange protonique inverse (Reverse Proton Exchange, RPE) peut être utilisée. Elle permet de remplacer les protons présents à la surface par des ions de Lithium en plongeant le cristal dans un bain riche en Li^+.[22–24]

Pour fabriquer un guide d'onde enterré, il est donc nécessaire de réaliser un guide d'onde profond par l'échange de protons, puis "d'effacer" une partie du guide à la surface par RPE jusqu'à une certaine profondeur. Un exemple d'un tel guide d'onde est représenté sur une figure où les profils d'indice sont tracés pour un guide d'onde avant et après RPE (figure 2(b)).

Si le guide d'ondes initial est de type SPE, il présente un profil d'indice exponentiel où l'indice diminue très rapidement avec la profondeur. Ainsi, après le processus de RPE, qui reconstruit le substrat près de la surface, la variation maximale d'indice du guide d'onde enterré est assez faible. Par conséquent, dans ce cas, l'optimisation du recouvrement intermodal est obtenue au détriment du confinement optique.

Pour éviter ce compromis, nous avons proposé de commencer avec un autre type de guides faits par échange protonique. En jouant avec l'acidité du bain, on peut réaliser

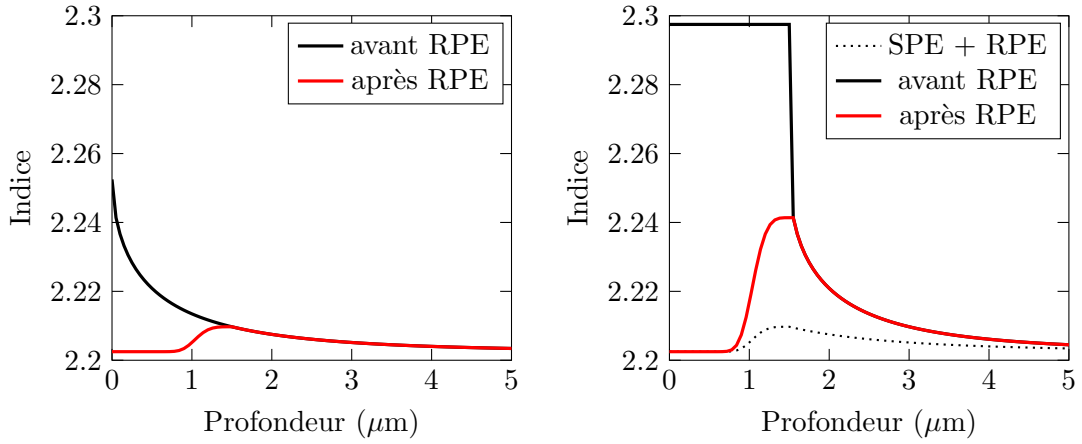

(a) RPE en combinaison avec SPE

(b) RPE en combinaison avec un profil d'indice complexe

FIGURE 2: Les profils d'indice sont tracés pour des guides d'onde avant et après RPE.

des guides d'ondes avec des profils d'indice complexes composés d'une partie à saut d'indice suivie par une partie à gradient. La partie à gradient d'indice de ces guides est similaire à calle des guides d'onde SPE, et les non-linéarités sont préservées. Grâce au procédé RPE, on est en mesure d'effacer la partie saut d'indice du profil sans modifier la partie à gradient. Il est ainsi possible de réaliser un guide d'onde enterré présentant une variation d'indice aussi élevée que dans des guides APE ou SPE (figure 2(b)).

Cependant, une analyse structurelle et optique de la couche à saut d'indice de ces guides d'onde complexes a révélé qu'ils étaient très semblables aux couches obtenues par échange en phase vapeur (Vapor phase Proton Exchange, VPE). Ces guides d'onde VPE sont les seuls guides fabriqués sur $LiNbO_3$ qui présentent une variation d'indice $\delta n_e = 0{,}1$ et des coefficients non linéaires intacts.[25–29] Cependant, cette technique c'est montré tellement peu reproductible, quil a été impossible de l'utiliser pour fabriquer des dispositifs utiles.[30]

Par contre, la première étape du processus que nous avons développé pour fabriquer des guides enterrés, est raisonnablement reproductible. La possibilité de fabriquer des guides d'ondes à fort confinement présentant des coefficients non linéaires intacts ouvre la voie à beaucoup de rêves. C'est le point de départ de ce travail de recherche consacré à l'étude d'un processus de fabrication que nous avons baptisé HISoPE pour "High Index Soft Proton Exchange".

Cest cette technique qui nous a permis de proposer et d'étudier la réalisation de fils quantiques sur $LiNbO_3$.

Tenant compte de l'anisotropie du $LiNbO_3$ le processus d'échange protonique et les applications potentielles des circuits étudiés sont très différents sur coupe X et sur coupe Z.

La coupe X du substrat est très fréquemment utilisée pour réaliser des modulateurs électro-optiques. Le travail que nous avons entrepris avait pour but d'améliorer leurs performances et de réaliser des modulateurs ultra-compacts à faible tension de commande en utilisant des cristaux photoniques (Photonic Crystal, PC). Dans les diélectriques, les PCs sont généralement obtenus en réalisant un réseau de trous d'air nanométriques et organisés périodiquement. Cette structure optique, avec une période comparable à la longueur d'onde, modifie la propagation de la lumière en raison d'interférences multiples. Suivant l'organisation et les paramètres choisis, la vitesse de groupe de la lumière peut être ralentie, voire annulée, le matériau ou le guide d'onde dans lequel le PC est réalisé présentant alors une bande interdite. Si le matériau est électro-optique, cette bande interdite peut être déplacée par un champ électrique externe ce qui permet de moduler la lumière transmise par le dispositif.

Malgré ces perspectives prometteuses, aucune réalisation expérimentale n'a présenté des performances intéressantes pratiquement. Une des difficultés principales est qu'aucune des techniques de nanostructuration connues ne permet pas de réaliser des trous suffisamment profonds pour que les réalisations pratiques se comportent conformément aux prévisions numériques. Par conséquent, les PCs ajoutent des pertes à la propagation importantes à cause de la diffusion de la lumière hors des guides d'onde.[31–33] Selon les résultats publiés, l'utilisation des faisceaux d'ions focalisés (Focused Ion Beam, FIB) est la meilleure façon de fabriquer des PCs sur $LiNbO_3$, mais elle est loin d'être idéale. Le problème principal est que la redéposition des produits de gravure limite le percement de trous d'air de petits diamètres $\approx 350\,\text{nm}$. Cet effet cause une fermeture rapide des trous, limitant leur profondeur à moins de $2\,\mu\text{m}$.

Des guides d'onde de type membrane et "ridge" ont été proposées pour améliorer la combinaison avec les PCs créés par FIB.[34,35] Ces configurations aident à l'évacuation du matériau hors des trous lors de la gravure. Mais les applications possibles de ces dispositifs sont limitées par leur fragilité, et le couplage de ces structures avec des fibres standards est problématique. Par conséquent, il existe un fort intérêt à combiner les PCs avec des guides d'onde classiques réalisés sur $LiNbO_3$. Les techniques connues, comme la diffusion de Ti, ou les échanges protoniques de type SPE ou APE fabriquent des guides où les modes ont un diamètre typique de $5\,\mu\text{m}$. Ces modes sont donc faiblement couplés avec le PC et ils voient le fond des trous, qui est une région fortement perturbée. Ces guides subissent une forte diffusion et donc des pertes à la propagation très élevées.

Des guides d'onde à fort confinement semblent d'être un bon moyen de résoudre ces problèmes.

C'est ce qui a motivé l'étude de la combinaison PCs guides HISoPE sur $LiNbO_3$ coupe X pour réaliser un modulateur d'intensité électro-optique très efficace dans le cadre du projet PhoXcry. Les pertes des guides d'onde HISoPE, de type canal, réalisés sur la coupe X sont autour de 1,7 dB/cm. Les pertes à la propagation sont principalement dues à la nature hybride des modes, induite par les déformations cristallines de la couche échangée. Cette valeur n'est pas très bonne, mais pourrait être acceptable pour des dispositifs très courts comme le modulateur envisagé, mais d'autres développements, utilisant une combinaison de plusieurs échanges protoniques, sont en cours pour tenter de réduire les pertes.

La nanostructuration des guides HISoPE ajoute environ 15 dB de pertes à la propagation sur la plage où le guide est monomode et fait apparaître une structuration de la transmission en introduisant des minima pour certaines longueurs d'onde. Comme nous ne disposons pas de simulations numériques quantitatives tenant compte de la forme réelle des trous d'air du PC, ces résultats sont insuffisants pour conclure que ses minima correspondent à des bandes interdites photoniques.

Nous avons également étudié les guides HISoPE sur les substrats de coupe Z, car le grand avantage de cette coupe est la possibilité de réaliser satisfaire des conditions de quasi-accord de phase (Quasi-Phase Matching, QPM) pour des applications optiques non linéaires en utilisant du niobate de lithium polarisé périodiquement (Periodically Poled Lithium Niobate, PPLN). Aujourd'hui, pour des expériences de SHG, l'efficacité de conversion la plus élevée, a été obtenue pour des guides d'ondes APE enterrés. Elle vaut 150 $\%\mathrm{W}^{-1}\mathrm{cm}^{-2}$.[36]

En augmentant le confinement des modes optiques il est possible d'augmenter sensiblement cette efficacité. Ainsi, la conversion normalisée théorique calculée pour des guides d'ondes "SPE enterrés" avec $\delta n_e = 0{,}03$ est égale à 300 $\%\mathrm{W}^{-1}\mathrm{cm}^{-2}$.[36,37] Dans des guides d'onde HISoPE avec des non-linéarités préservées et le fort confinement optique lié à $\delta n_e = 0{,}09$, les calculs montrent que l'efficacité de conversion non linéaire peut encore être augmentée par un facteur de trois.

L'étude des guides plans montre que les guides HISoPE obtenus sur coupe Z sont très différents de ceux obtenus sur coupe X. Dans les guides d'ondes multimodes, des modes avec des indices effectifs intermédiaires présentent des pertes de propagation élevées, tandis que le mode fondamental et les modes d'indices effectifs faibles se propagent bien. Ce problème peut être résolu en augmentant l'acidité du bain utilisé pour l'échange protonique. Nous avons ainsi réussi à produire des guides d'ondes HISoPE plans à

faibles pertes. Grâce à des expériences de génération de deuxième harmonique localisée, nous avons montré que les propriétés non linéaires de ces guides d'onde ne sont pas détruites.

Grâce aux spectres de rayons X, nous avons pu montrer que cette modification de la concentration du bain permet de réduire le signal correspondant à une couche de transition non homogène, qui apparaît entre le pic du substrat et le pic d'une couche échangée. Nous avons donc conclu que cette couche, se trouvant au milieu du guide, était responsable des pertes et on a choisi d'utiliser un bain plus acide, mais ce choix s'est avéré être problématique lorsque nous avons fabriqué des guides d'ondes canal. En effet, à l'aide d'un bain plus acide, nous avons obtenu des guides d'onde avec un taux de substitution plus élevés et donc des déformations cristallines plus importantes et contrairement à ce qui était attendu pour des raisons de symétrie, nous avons observé des modes hybrides dans ces guide. Les meilleurs guides, que nous avons fabriqué, ont des pertes à la propagation autour de 5 dB/cm. Avant de fabrique des guides sur PPLN, il faut s'assurer que la superposition de plusieurs processus permettra de produire de meilleurs guides.

Par ailleurs, HISoPE sur la coupe Z du $LiNbO_3$ a été utilisé avec succès en combinaison avec une technique d'échange inverse (RPE) afin de fabriquer des guides d'onde enterrés dans PPLN. Comme les conditions de RPE ne sont pas suffisamment optimisées, les premiers guides, que nous avons fabriqués, ont plusieurs problèmes tels que des pertes d'environ 2 dB/cm et un comportement de coupleur directionnel. Compte tenu de ces défauts, il a cependant été possible de montrer que ces guides ont une efficacité normalisé de conversion de $160\%\,\mathrm{W}^{-1}\mathrm{cm}^{-2}$, qui est égale à la meilleure valeur rapportée à ce jour, et qui permet d'espérer que la poursuite de l'amélioration de la combinaison HISoPE - RPE, permettra approcher les $300\%\,\mathrm{W}^{-1}\mathrm{cm}^{-2}$ prévus par la théorie.

Enfin, l'étude détaillée du procédé HISoPE en fonction des conditions de fabrication, a montré qu'un processus d'exodiffusion ou au moins de perte d'oxygène pouvait se superposer à l'échange. Ce phénomène pourrait permettre d'expliquer un certain nombre de résultats observés en optique nonlinéaire, mais comme cela a été découvert tout à la fin de cette thèse, ce sera étudié dans un travail futur.

Genesis of the realized work

Since the middle seventies, lithium niobate ($LiNbO_3$) has been used to fabricate optical waveguides[1–5] with the potential of realizing efficient intensity and phase modulators and nonlinear frequency converters via the electro-optic and nonlinear properties of the crystal.[38–42] The first explored technique was metal (mainly Titanium) indiffusion, which allows creating a graded index waveguide at the surface of the crystal with a maximum index increase on the order of 0.02.[6,7]

The Proton exchange method, firstly proposed in the early 1980's, gave a push to investigations of Integrated Optics (IO) on $LiNbO_3$.[5,8–10] It consists in plunging the crystal in a hot acidic melt to replace part of the lithium ions of the crystal by protons. This process induces an increase of the extraordinary index which allows realizing optical waveguides at the surface of $LiNbO_3$ crystal. Depending on the chemical reagent used as a source of protons, and the temperature of the melt, one can realize waveguides with very different index profiles.

It was rapidly verified that proton exchanged waveguides fabricated in concentrated proton sources have a step refractive index profile with a high extraordinary index change of $+0.1$ at a wavelength of 633 nm.[5] These waveguides triggered a strong interest, as a high index increase is a key property for sharp bends and therefore dense optical integrated circuits. Unfortunately these waveguides were also presenting a dramatic reduction of the electro-optic and nonlinear coefficients,[11–15] which explains that the interest dropped down.

Nevertheless, some modifications of the protocol, such as adding a post exchange annealing or reducing the acidity of the melt, allowed realizing useful waveguides called Annealed Proton Exchange (APE)[16] and Soft Proton Exchange (SPE),[17,18] respectively. Such waveguides present preserved electro-optic and nonlinear properties and a gradient index profile with reduced index change (≤ 0.03). They are particularly suitable to realize devices operating in the near IR (800 nm), as they are less sensitive to the photorefractive damage.[19–21]

At Laboratoire de Physique de la Matière Condensée (LPMC) in Nice, we are mainly interested in nonlinear components and a good way to improve the efficiency of such devices is to realize embedded waveguides. Indeed, surface waveguides present an asymmetric index profile, the index contrast between the air and the waveguide being by far higher than the contrast between the waveguide and the substrate. A particular disadvantage of these asymmetric gradient index waveguides is that the intensity maxima of the modes at different wavelengths are situated at different depths in the waveguide (figure 3).

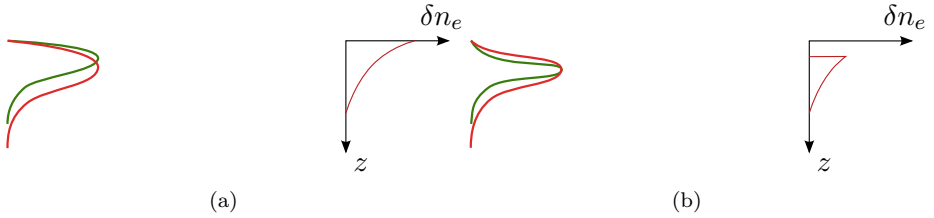

FIGURE 3: Schematic representation of: (a) the surface waveguide with the gradient index profile, and (b) the embedded waveguide.

This is not favorable to the nonlinear interactions, which couple at least two different wavelengths, and whose efficiency is proportional to the overlap of the interacting modes. To symmetrize the modes and, consequently, to improve the efficiency of nonlinear interactions, one can bury the waveguide into the substrate. Reverse Proton Exchange (RPE), which allows replacing protons by Li^+ ions in the crystal by plunging it in a Li-rich bath, can be used for this purpose.[22–24]

To fabricate a buried waveguide it is therefore necessary to realize a deep waveguide by proton exchange, and then to 'erase' it, down to a certain depth, to reconstruct $LiNbO_3$ at the surface by RPE. An example of such a waveguide is represented in figure 4(a) where the index profiles are plotted for the waveguide before and after RPE. The initial SPE waveguide has an exponential index profile where the index drops quickly with the depth. Thus, after the RPE process, which reconstructs the substrate near the surface, the maximum index change of the buried waveguide is quite small. Consequently, in this case, the optimization of the intermodal overlap is obtained at the expense of the optical confinement.

To avoid this trade off, we proposed to start with a different kind of Proton Exchanged waveguides. Indeed, playing with the acidity of the bath in a way that we will describe later on in section 3.2, allows realizing waveguides with complex index profiles composed of a step section followed by a gradient one.

The gradient part of these waveguides is similar to that of SPE waveguides, in which nonlinearities are preserved. Using an appropriate RPE process, one should be able to

erase the step section of the index profile without modifying the gradient one. It should then be possible to realize buried waveguides presenting maximum index increase as high as APE or SPE surface waveguides (figure 4(b)).

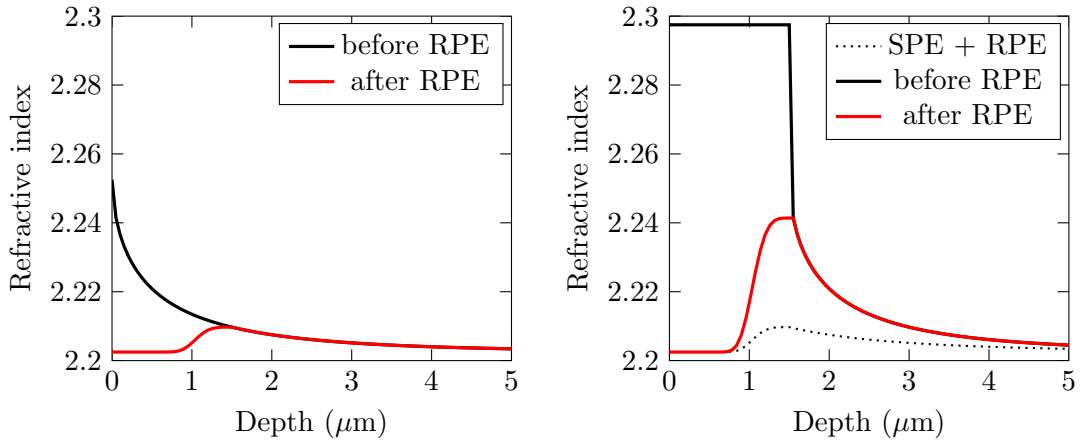

(a) RPE in combination with SPE

(b) RPE in combination with hybrid profile

FIGURE 4: Index profiles of planar waveguides before and after RPE.

However, the structural analysis of the step layer of the complex waveguides realized during the first fabrication step revealed that they were very similar to the layers obtained by Vapor-phase Proton Exchanged (VPE). In the literature it is reported that VPE waveguides[25–29] are the only waveguides fabricated on $LiNbO_3$ with $\delta n_e = 0.1$ and preserved nonlinear coefficients. Nevertheless, it was impossible to use this technique to fabricate useful devices as the reproducibility reveals to be very poor.[30] On the contrary, the process that we developed to fabricate the initial waveguide is reasonably reproducible.

The possibility to fabricate with a reproducible process, highly confining waveguides with preserved nonlinear coefficients, opens the way to a lot of dreams.

This is the starting point of this research work devoted to the study of the fabrication process we call High Index Soft Proton Exchange (HISoPE). In the following report, I will first discuss the state of the art concerning waveguide fabrication by Proton Exchange in $LiNbO_3$. In the second chapter, I will present the necessary theoretical backgrounds. I will present the nonlinear interactions in waveguides and in periodically poled materials as well as the propagation of hybrid modes (modes with coupled TE and TM polarization) in highly stressed guiding layers. Then, taking into account the anisotropy of $LiNbO_3$, the approach and the potential applications are very different on X-cut and Z-cut substrates. The last part of the report with results and discussion will then be separated into two parts.

In the third chapter I will present the highly confining waveguides realized on X-cut $LiNbO_3$ substrates which are very convenient to design electro-optical modulators.[12,43] The external control electric field can be delivered by a couple of electrodes simply deposited aside the waveguides.

Another reason of interest for the X-cut substrates concerns the coupling of highly confining waveguides with photonic crystals (Photonic Crystal, PC) for realization of ultra-compact modulators with low driving voltage.[44] PCs are usually composed of nanometric air holes periodically placed in the dielectric. This optical structure, with a period comparable to the wavelength, affects the motion of light due to multiple interferences. The group velocity of the light in this resonant optical system can be slowed down. PC in an optical waveguide realized in an electro-optical material introduces an optical band gap that can be modulated by an external electric field. Theoretically, PC band modulators can be very short and very efficient.[44]

Despite all these promising perspectives, no successful experimental realization have been reported yet on $LiNbO_3$. The main difficulty is that all the known nanostructuring techniques are unable to realize PC of good quality on $LiNbO_3$. As a result, the PC adds significant propagation losses, diffusing light out of the waveguide.[31–33] According to published results, Focused Ion Beam (FIB) milling is the best way to fabricate PC in $LiNbO_3$, but obtained PCs are far from being ideal.[45] The problem is that the redeposition of $LiNbO_3$ limits the milling of air holes of small diameters ($\sim 350\,\mathrm{nm}$). This results in a rapid 'closing' of the holes when moving from the surface to the depth. Consequently, the holes have a conical shape and a limited depth ($< 2\,\mu\mathrm{m}$).

Membrane[34] and ridge[35] waveguides $LiNbO_3$ were proposed to improve the FIB milling results. These configurations help evacuating the material off the holes during etching. But the possible applications of such devices are limited by their fragility, and coupling these structures to standard fibers remains an issue. Therefore there is a strong interest to couple PC with more classical waveguides realized in the material. The known techniques, like Ti-indiffusion, SPE or APE, produce waveguides that support modes which are $5\,\mu\mathrm{m}$ in diameter. These modes are therefore weakly coupled with the PC and see the holes' bottom, which is a strongly perturbed region, and thus experience strong diffusion and propagation losses. Highly confining waveguides appear to be a good way to solve these problems.

Within the scope of the project PhoxCry, I started to study the HISoPE process in order to obtain guided modes with diameters smaller than the hole depth and hopefully without degraded nonlinear and electro-optic coefficients. I will describe all the fabrication details as well as the first attempts to combine HISoPE waveguides with PCs in Chapter 3.

The great advantage of the Z-cut orientation of $LiNbO_3$ is the possibility to realize Periodically Poled Lithium Niobate (PPLN) to achieve Quasi-Phase Matching (QPM) conditions (sections 2.2.3) for nonlinear optical applications.[46–49] Today, the best reported conversion efficiency for Second Harmonic Generation (SHG) for buried PPLN waveguides is $150\%\,\mathrm{W}^{-1}\mathrm{cm}^{-2}$ while the theoretically calculated normalized conversion efficiency for buried waveguides with $\delta n_e = 0.03$ (figure 4(b)), assuming an ideal first-order QPM grating and a preserved nonlinearity, is $300\%\,\mathrm{W}^{-1}\mathrm{cm}^{-2}$.[36,37]

The possibility, using HISoPE waveguides, to benefit from preserved nonlinearity combined with high confining ability ($\delta n \geq 0.09$) allows increasing further the nonlinear conversion efficiency by a factor of three. In Chapter 4 I will describe how I have adapted the HISoPE technique to Z-cut $LiNbO_3$ aiming to find the best optical properties of the waveguides. Unfortunately we found that HISoPE technique is not as easy to apply to Z-cut as to X-cut surface orientation, with which it worked quite well. Therefore we investigated in parallel buried waveguides, for which the complex index shape of the HISoPE waveguides is a good starting point.

Chapter 1

Proton exchanged waveguides on $LiNbO_3$: state of the art

1.1 Lithium Niobate

Before outlining waveguide fabrication issues on lithium niobate, I will describe the material and its physical properties. Lithium niobate ($LiNbO_3$) is a synthetic crystal, first grown in the early 1960s using the Czochralski technique.[50] Further deep investigation of $LiNbO_3$ crystal at Bell Laboratories in the late 1960's[51–55] resulted in the use of this material for signal processing chips for cable television. With the improvement of the material quality, $LiNbO_3$ crystals have been widely used for the fabrication of high speed optical modulators, gyroscopic chips, optical wavelength converters, optical parametric amplifiers, etc.[56] Today, concurring with indium phosphide (InP) and gallium arsenide (GaAs), $LiNbO_3$ remains one of the most attractive electro-optic material offering better modal overlap with standard optical fibers and higher nonlinear coefficients.

Lithium niobate is an uniaxial birefringent crystal with ordinary n_o and extraordinary n_e refractive indices. It is also a transparent over a wide wavelength range extending from 340 to 4600 nanometers. Some other physical and optical properties are given in the following table 1.1.

At room temperature, which is much lower than T_{Curie}, $LiNbO_3$ is a ferroelectric material consisting of planar sheets of oxygen atoms in a distorted hexagonal close-packed configuration.

The octahedral interstices formed in this structure are one-third filled by lithium atoms, one-third by niobium atoms, and one third by vacancies.[58] The displacement of the Li and Nb ions (see figure 1.1(b)) relative to the mass center, or simply speaking to the

TABLE 1.1: Physical and optical properties of congruent $LiNbO_3$ crystal proposed commercially by Crystal Technology Inc.

Congruent composition	48.38 mol%Li_2O
Congruent melting point	$\approx 1250°C$
Curie temperature (T_C)	$1142.3 \pm 0.7°C$
Point group	$3m$
Space group	$R3c$
Lattice constants (hexagonal)	$a_h = 5.151$ Å
	$c_H = 13.866$ Å
Density	$4.65\,g/cm^3$
Optical transmission	UV cutoff($1/e$): 340 nm
	IR cutoff($1/e$): 4600 nm
Refractive index at 633 nm	$n_o = 2.2866$
	$n_e = 2.2028$
Nonlinear optical coefficients ($\lambda = 1.06\,\mu m$)	$d_{22} = 3$ pm/V
	$d_{31} = -5$ pm/V
	$d_{33} = -33$ pm/V

Electro-optic coefficients (pm/V at 633 nm)

	r_{13}	r_{22}	r_{33}	r_{51}	r_z
clamped	10	7	33	33	18
unclamped	9	3	31	28	19

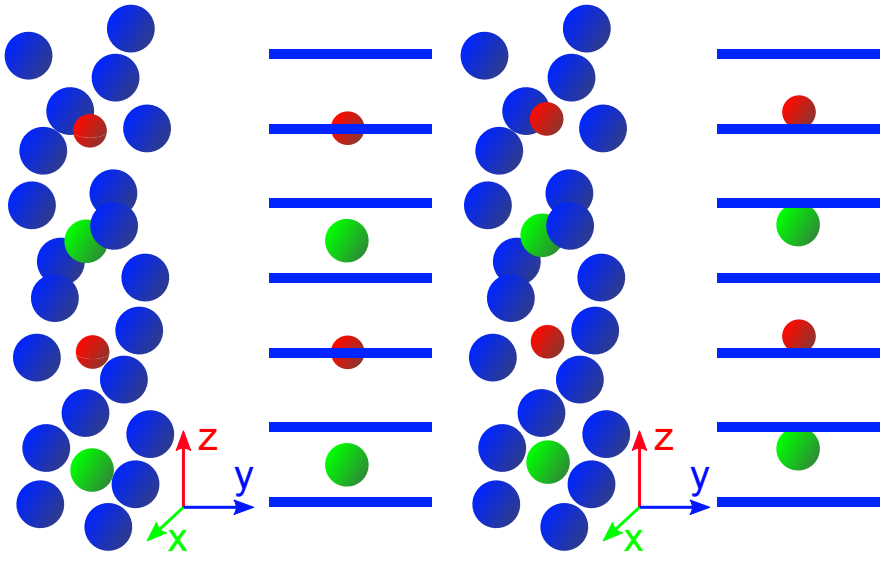

(a) $T \geq T_c$ (b) $T \leq T_c$

FIGURE 1.1: Representation of the unit cell of $LiNbO_3$: positions of the lithium (red color) and the niobium (green color) atoms with respect to the oxygen layers (blue color) in the (a) paraelectric and (b) ferroelectric phases.[55,57]

oxygen layers, is responsible for the spontaneous polarization along the Z axis (see figure 1.1). This broken centrosymmetry actually causes the unique piezoelectric, optical and photo-elastic properties of the $LiNbO_3$.

For integrated optics fabrication, three crystal orientations are commercially available: Z-, X- and Y-cut lithium niobate wafers.

1.1.1 Crystallographic orientations of $LiNbO_3$

One should remember the relation between two coordinate systems, which are often used with $LiNbO_3$ crystal. While crystallographic planes within a three-dimensional crystal are described by Miller indices hkl, a Cartesian coordinate system is used to describe the physical tensor properties of the $LiNbO_3$. To describe the physical properties of the crystal, it is more convenient to use the orthogonal coordinate system, in which we can represent a unit cell as a cylinder with an exact hexagon as a base (figure 1.2).

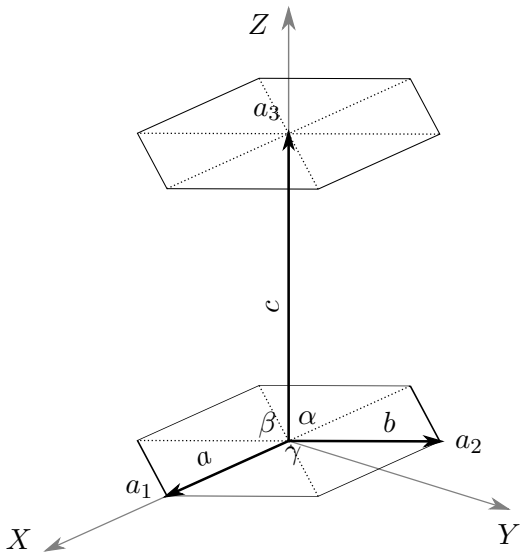

FIGURE 1.2: Crystallographic orientations of $LiNbO_3$.

In this base, we have $a = b \neq c$, $\alpha = \beta = 90°$ and $\gamma = 120°$. For simplicity we will name the crystallographic axes as a_1, a_2 and a_3 as it is shown on the figure 1.2, or simply 1, 2 and 3.

The Cartesian coordinate system is chosen in such a way that the axis Z is parallel to the optical axis. In our case, Z is parallel to a_3 and perpendicular to a_1 and a_2. Axis X coincides with a_1 and is parallel to mirror plans of the crystal symmetry. The axis Y completes the coordinate system. Relation between the lattice constants for these two

different coordinate systems is

$$a_x = a = b = a_h \qquad a_y = \frac{\sqrt{3}}{2} a_h \qquad a_z = c. \tag{1.1}$$

1.2 Proton exchange

1.2.1 Principles and experimental techniques of proton exchange

Such an attractive material as $LiNbO_3$ can be and is used in free space optic configuration. But the possibility to confine light in a waveguide is more than interesting because integrated optical devices win not only in compactness but also in efficiency of non linear interactions.

The waveguide fabrication technique known as proton exchange was firstly proposed by Jackel, Rice and Veselka in the early 1980's.[8] The main advantage of this process lies in the fact that it is relatively simple to be implemented.

The idea of the proton exchange technique is to change the refractive index at the surface of the $LiNbO_3$ crystal by immersing it in a source of protons, usually week organic acid (e.g. benzoic acid, palmitic acid, stearic acid, cinnamic acid, and related mixtures).[59–65] The melt is heated with the crystal to a temperature around 200°C depending on the melting point of the proton source. When the crystal is dipped into the melt, protons start to enter the crystal and to substitute part of the lithium. The process is described by the following equation:

$$LiNbO_3 + xH^+ \Longleftrightarrow Li_{1-x}H_xNbO_3 + xLi^+. \tag{1.2}$$

The exchange rate x mainly depends on the acidity of the proton source and the temperature of the melt. For waveguide fabrication, there is no interest in total exchange rate as it leads to a dramatic crystal symmetry change compared to the original $LiNbO_3$ hexagonal structure to the cubic structure of $HNbO_3$. This new symmetry cancels all nonlinear properties of the material and induces very strong stresses between the exchanged layer and the substrate. During the exchange, dramatic relaxation processes take place and destroy the surface layer preventing any waveguide fabrication. To avoid this, and be able to fabricate actually waveguides, one has to keep $x < 0.7$.[66]

The refractive index change is not isotropic for the proton exchange. This chemical method increases significantly the extraordinary index and decreases the ordinary one, with maximal achievable values of $\delta n_e = 0.12$ and $\delta n_o = -0.04$. Consequently, optical

waveguides fabricated in such a way support only one type of polarization modes: TE-modes are guided in proton exchanged X- and Y-cut $LiNbO_3$ and TM-modes in Z-cut $LiNbO_3$.

Depending on the concentration of protons in the source, one can vary the refractive index profile. A step-like profile with $\delta n_e \geq 0.1$ at $\lambda = 633\,\text{nm}$ can be obtained using pure acids. This value of the refractive index variation guarantees a very good optical confinement for most applications in integrated optics based on $LiNbO_3$. However, these waveguides are mainly composed of layers presenting a high substitution ratio, $0.5 < x < 0.7$.[67,68] That means a dramatic degradation of the nonlinear and electro-optical coefficients and rather high propagation losses ($> 1\text{dB/cm}$). The way out can be found by changing the acid, or by adding lithium salts into the proton sources (diluted proton sources), or by using a post exchange annealing process.

In our work, the proton source we used is a mixture of benzoic acid (BA) and lithium benzoate (LB). This acid has a low toxicity and is relatively inexpensive. Its melting point $T_m \approx 122°\text{C}$ and boiling point $T_b \approx 249°\text{C}$ allow also working within a large temperature range. This range can be further increased by using sealed ampules, which allow to go above the boiling point up to 350°C (for example, see figure 1.3). All these advantages make benzoic acid one of the most commonly used proton sources.

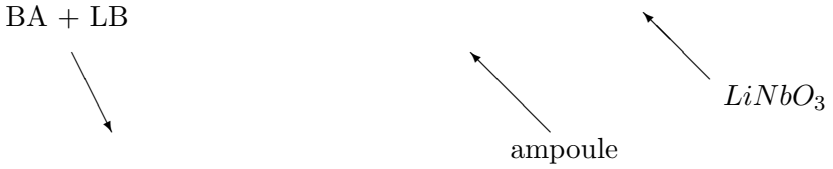

FIGURE 1.3: Schematics of sealed ampule with a sample of $LiNbO_3$ crystal inside.

To fabricate these ampules, we start with an open glass tube with a narrow constriction in the middle of it to separate the sample from the melt. After the powders and the crystal have been introduced inside the ampule, it is evacuated to a vacuum of the order of $10^{-4}\,\text{mbar}$. The tube is then sealed with a brazing torch. Subsequently, this ampule is placed into an oven and heated up to the desired temperature above the melting point, as a rule between 150°C and 300°C. The experience showed that at temperatures above 300°C the ampules frequently don't stand the pressure and start to leak. When the acid is melted, the ampule is turned upside-down such that the crystal plunges into the melt. The proton exchange starts and is carried out during a certain time calculated to obtain

the desired waveguide depth. To stop the process, the ampule is turned again, taken out of the oven, allowed to cool down and broken to take the sample out.

1.3 Variants of the proton exchange

Despite an apparent simplicity, the proton exchange technique requires a lot of handling precautions to realize waveguides with optimal properties. This explains why this method is still a subject of research with the objective to reach the best compromise between increasing the confinement and preserving the nonlinear and electro-optical properties. Since the early 80's, many variants of the proton exchange were proposed and developed.

One way to change the properties of the waveguide is to play with the concentration of LB in the proton source (figure 1.4). This allows to fabricate the optical waveguides with different index profiles (figure 1.5) and different maximal index changes.

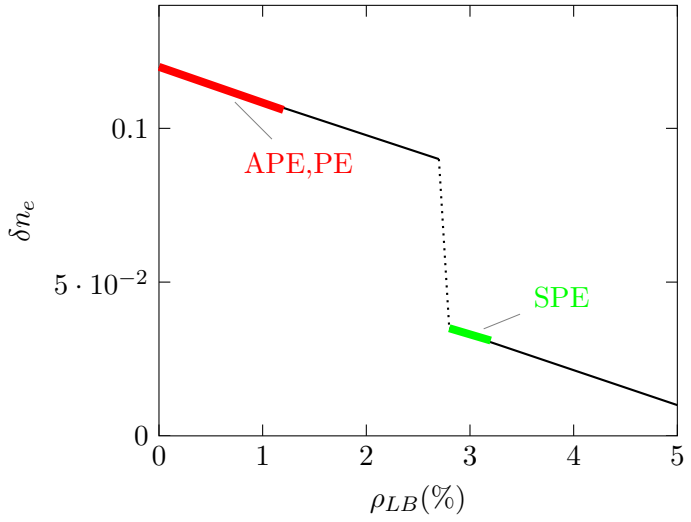

FIGURE 1.4: Working concentration intervals for waveguide fabrication on Z-cut $LiNbO_3$ at the temperature $T = 300°C$.

But also different types of the waveguides vary in their nonlinear optical properties. We will now make a quick overview of the various proton exchange techniques developed so far.

1.3.1 Proton Exchange

In this manuscript, I will call Proton Exchange (PE) the processes which use a highly acidic bath for the melt and produce a waveguide with a step-like index profile and a high index increase (figure 1.5). During the 80's, this high value of δn_e was considered

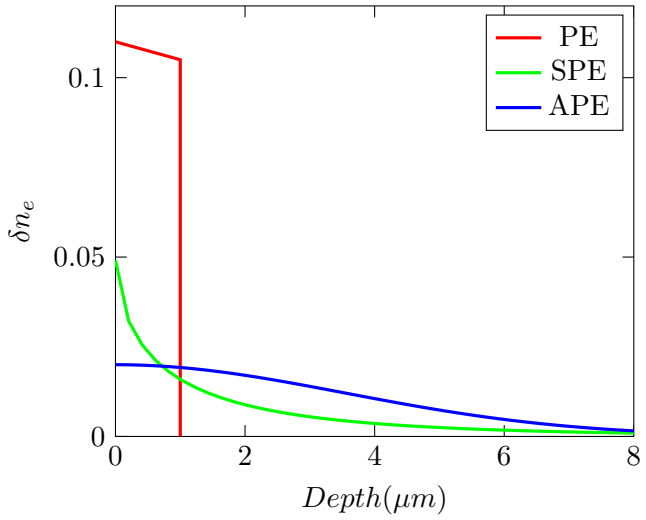

FIGURE 1.5: Typical index profiles at λ=633 nm of PE (red), APE (blue) and SPE (green) waveguides fabricated on lithium niobate by proton exchange.

to be a great advantage of PE waveguides,[8] but the interest decreased when it was established that the nonlinear and electro-optical coefficients were significantly reduced for this type of waveguides.[14]

These waveguides are obtained with pure BA or with light concentration of LB[69] ($\rho_{LB} \lesssim 1.2\%$). The presence of LB allows to improve the linear optical properties of the waveguides, however it is not sufficient to preserve the initial nonlinearities of the bulk $LiNbO_3$ crystal.

1.3.2 Annealed Proton Exchange

APE is a technique used commercially to fabricate integrated optical circuits.[11,16,70,71] The waveguides are fabricated in a two step process. A thin exchanged layer is formed using the PE process. Then the protons are redistributed into the crystal by an annealing[72] performed at a higher temperature. Indeed, thanks to a higher activation energy, the protons move into the depth of the crystal forming a low proton concentration layer which results in a gradient waveguide showing preserved nonlinear and electro-optical coefficients. Annealing is carried out at temperatures around 350-400°C in oxygen rich atmosphere to prevent Li_2O outdiffusion. The typical δn_e increase for APE waveguides is $\approx$0.02 (figure 1.5). Beside the weak optical confinement, another disadvantage of this technique is that if the PE process is made using a pure acid, the first thin layer formed after the exchange has permanently lost its nonlinear properties.[73,74] Cracks at the surface are common due to strains induced by the high substitution ration obtained at the end of the exchange.

1.3.3 Soft Proton Exchange

SPE technique involves diluted proton sources with relatively high amount of added Li ions.[17,75] The relatively high concentration of LB in the melt reduces the diffusion rate and also the kinetic of the exchange. Usually 3 days at 300°C in a 3% melt are necessary for the fabrication of a monomode waveguide at 1.5 μm. But in contrast to APE, this method proposes only one fabrication step and does not damage the crystal surface. The SPE waveguides have a gradient exponential index profile, which is comparable to APE δn_e (see figure 1.5). The choice of the working concentration of LB is subtle. First of all, the concentration must be higher than ρ_t. However, by moving far from the threshold, we decrease δn_e, which is weak. Usually SPE waveguides are therefore fabricated in melts of BA and LB with a ρ chosen to be as close as possible to ρ_t. In these conditions, a lot of controls are necessary to reach a good reproducibility.

1.3.4 Vapor-phase Proton Exchange

Another variant, VPE, consists of fabricating the waveguides in BA vapors using a sealed ampule.[28] This technique showed an ability to produce high index waveguides ($\delta n_e = 0.1$) without reduction of the nonlinear properties.[26,30] But a big problem for VPE stands as the reproducibility. The depth of the VPE waveguides is very difficult to control.[30] For this reason, even with such interesting results in nonlinearities and δn_e, VPE method is useless when the aim is to realize high quality nonlinear or electro-optical integrated devices.

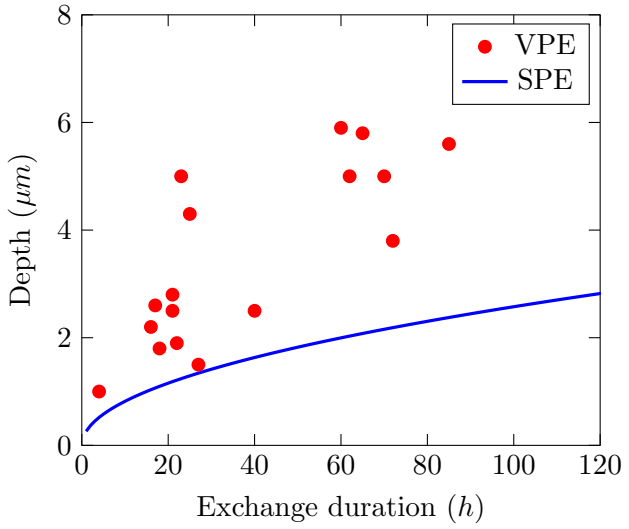

FIGURE 1.6: Kinetics of vapor-phase proton exchange (VPE) compared to soft proton exchange (SPE) (redrawn from Chanvillard[30]).

1.3.5 Reverse proton exchange

One of the characteristics of the proton exchange reaction 1.2 is that it is reversible. The initial surface of the $LiNbO_3$ crystal can be reconstructed in a similar way by immersing the crystal into a Li ions rich melt. This procedure allows producing buried waveguides and is called Reverse Proton Exchange (RPE).[22,76,77]

An example of the buried waveguide index profile is shown in figure 1.7. The initial SPE waveguide profile is modified by RPE. The depth of reconstructed substrate is 1.5 μm.

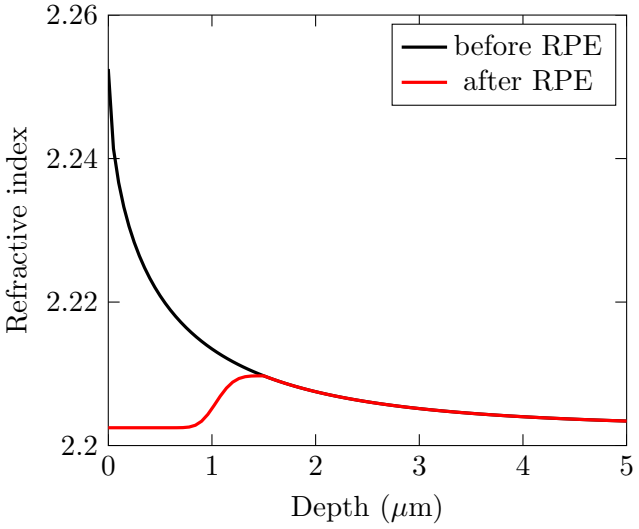

FIGURE 1.7: Index profile of the waveguide before and after RPE.

The refractive index contrast between the air and the waveguide at the surface is by far higher than the contrast between the waveguide and the substrate. This leads to a decrease of nonlinear interactions because of non-optimized overlap integral for optical modes at different wavelengths (see figure 1.8(a)).

The interest in buried waveguides is great. By embedding the waveguide into $LiNbO_3$ substrate, one can symmetrize the optical modes of different wavelengths (see figure 1.8(b)). If the distance between the surface and the waveguide is sufficient, the maxima of the intensities of the guided modes are placed practically at the same depth. As a result, we obtain an optimized overlap integral and, consequently, augmented efficiencies of the nonlinear interactions.

The mode symmetrization is the main advantage of buried waveguides. This improves both the nonlinear optical interactions performances and the coupling efficiency with optical fibres.

Another advantage of buried waveguides is a significant reduction of the propagation losses due to surface imperfections. A simple scratch on the surface can dramatically

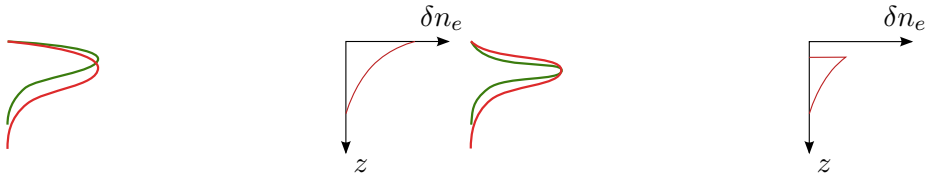

FIGURE 1.8: Symmetrization of waveguide by RPE technique.

increase them as the depth of the waveguide is only a few microns depending on the value on δn_e. Consequently, the crystal volume above the buried waveguide serves as a protecting layer.

Concerning the fabrication procedure, RPE is usually carried out in a melt of KNO_3 : $NaNO_3$: $LiNO_3$ with a proportion ratio 1:1:0.1, respectively. The RPE procedure at temperatures higher than the direct proton exchange is complicated by the annealing effect, i.e. the protons start again to diffuse into the substrate, modifying the shape of the initial index profile. Thus, it is recommended to use the same temperature for both direct and reverse proton exchange.

1.4 Overview of alternative waveguide fabrication techniques on $LiNbO_3$

Many waveguide fabrication techniques have been proposed aside the proton exchange.[2] Lithium oxide (Li_2O) outdiffusion,[78–80] titanium-indiffusion[81–85] and ion-implantation[86] are among them. More recently, the direct ultraviolet writing technique has also been proposed.[87] Titanium-indiffusion and proton exchange methods are however the only ones to be used for commercial devices.

Li_2O outdiffusion technique is based on the fact that the extraordinary refractive index of $LiNbO_3$ depends on the crystal stoichiometry,[88,89] increasing when the lithium concentration is reduced. The ordinary index is quasi not affected by the process. Thus, an optical guiding layer can be formed by heating a $LiNbO_3$ crystal at typical temperatures > 800°C in vacuum,[78,79] which results in Li_2O outdiffusion from the surface. The maximum index change δn_e achievable using this technique lies between 10^{-2} and 10^{-3}.

Metal-indiffusion method involves a coating step of the $LiNbO_3$ during which a thin metallic film is deposited on the surface. More often it's titanium,[81] and heating between 850°C and 1150°C for a few hours allows the metal oxide formed on the surface diffusing into the substrate. This method permits to increase both n_e and n_o with no degradation of the electro-optical effect. Maximum index changes are $\delta n_e = 0.025$ and $\delta n_o = 0.01$.

The main disadvantage of this technique is the dramatic photorefractive effect which occurs at visible wavelengths.

The second problem comes from the fact that the diffusion temperature is close to T_{Curie} which explains that it induces a domain reversal when performed on the C+ face. It is therefore quite complicated to superimpose with periodic poling.[90]

Ion-implantation technique involves implanting light ions (usually He^+) into $LiNbO_3$ substrate. Where they stop, the ions form a buried layer with a lower refractive index than that of the bulk crystal. The depth of the waveguide depends on the ion energy while the ion dose determines the refractive index change. Usually the fabrication procedure includes a post-fabrication annealing that removes the damages induced in the surface layer and reduces the propagation losses. However, this technique suffers from reduced electro-optical coefficients[91] and requires very complicated masking techniques to realize channel waveguides.

Combinations of the methods are also possible. For example, we find the proton exchange combined with Ti-indiffused $LiNbO_3$ producing so-called TIPE waveguides,[92] or ion-implantation in pair with Ti-indiffusion.[93]

In spite of this variety of methods there is no definite winner. However among all the proposed techniques, proton exchange is one of the most attractive and has several advantages, such as reduced photorefractive effect[9] and potential for high confinement.

1.5 Influence of different fabrication parameters on the waveguide properties

1.5.1 Influence of LB concentration on the waveguide properties

By adding Li ions in the proton source, we can significantly reduce the acidity of the melt and modify the concentration of the protons inside the $LiNbO_3$ substrate. This tends to lower the δn_e of the produced waveguides and to reduce the effect of the process on the nonlinear and the electro-optical properties of the crystal. Hence, the control of the LB concentration is very important. It is defined by the ratio ρ:

$$\rho = \frac{m_{LB}}{m_{LB} + m_{BA}}. \tag{1.3}$$

In our fabrication runs we changed ρ from 0 to 5%. The relation between the refractive index change and the concentration of LB is not a linear function. As we can see from

figure 1.9, there is a threshold concentration ρ_t above which the refractive index change δn_e drops immediately from about 0.09 to 0.03.

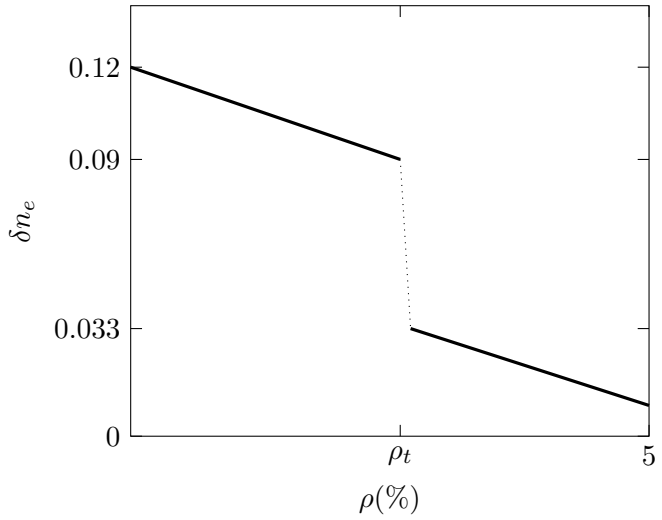

FIGURE 1.9: Influence of LB concentration on the maximal δn_e increase in final waveguides.

This behaviour is explained by the crystallographic structure of the waveguide and will be detailed in section 1.6. Some crystallographic phases $Li_{1-x}H_xNbO_3$, which give a high increase of δn_e, only appear when low LB concentrations are used. And ρ_t is a limit concentration at which these phases can be formed. The concentration ρ_t is about 2.6% at $T = 300°C$, but can slightly vary depending on other fabrication parameters or conditions.

1.5.2 Influence of temperature on the waveguide properties

An appropriate temperature regime is very important in the proton exchange fabrication procedure. The temperature is generally responsible for ρ_t position. As we can see on figure 1.10, ρ_t moves towards lower concentration of LB with the temperature increase.

By changing the temperature, we modify the diffusion rate of the protons. Thus, higher temperatures allow to reduce the fabrication time of a waveguide for a given depth. However, it is not the only interest to work with relatively high temperatures.

An infrared (IR) absorption characterization of proton exchanged waveguides in figure 1.11 shows a non-polarized peak, which reduces with the temperature increase. There is only one narrow absorption peak, polarized perpendicularly to the optical axis due to *O-H* bonds lying in the oxygen planes, but at lower temperatures, a second broad, unpolarized absorption band appears that we attribute to randomly oriented *O-H* bonds.

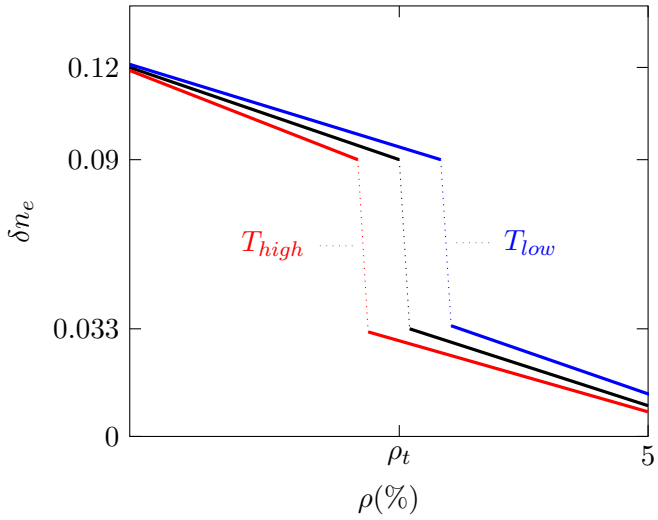

FIGURE 1.10: Influence of the temperature on the ρ_t position.

The presence of the latter is not surprising in layers presenting an important disorder. Consequently, the higher temperature ($\sim 350°C$) favours a better crystallographic organization in the waveguides and, thus, reduces the propagation losses due to light diffusion.[94]

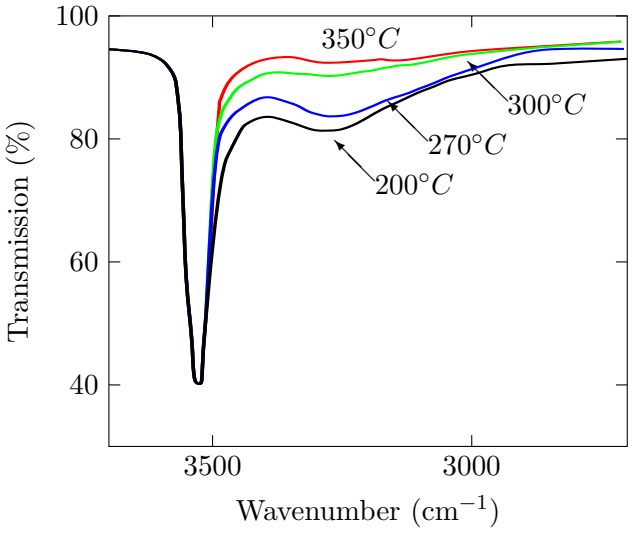

FIGURE 1.11: IR absorption spectra for the waveguides fabricated at different temperatures.[95]

In addition the Rutherford Backscattering (RBS) spectra confirm this conclusion by showing the crystal disorder induced by the proton exchange at low ($\sim 200°C$) temperature (figure 1.12).

But higher temperature also complicates the experimental part of the question. For example, sealed quartz ampules (fig.1.3) allow to fabricate optical waveguides at temperatures up to 300°C. But at 350°C the glass ampules do not stand the high vapor

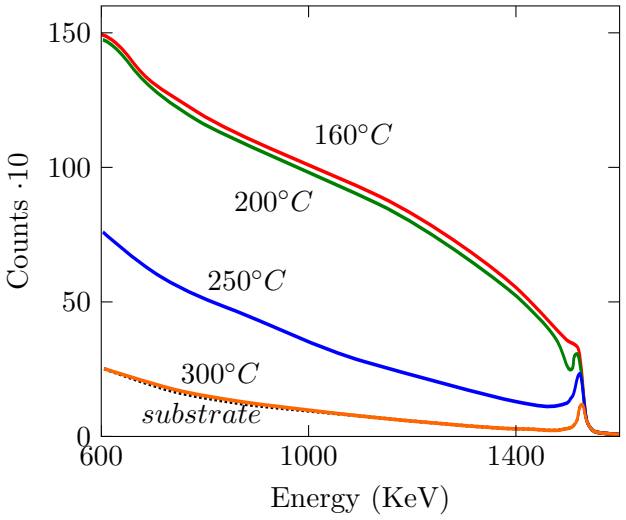

FIGURE 1.12: Rutherford backscattering of PE waveguides realized in pure BA at different temperatures.[95]

pressure of BA. This is the main reason why $T = 300°C$ was chosen as the most convenient temperature from the practical point of view. Besides, the difference seems to be not very important between 300°C and 350°C as we can see from the IR spectra.

1.5.3 Kinetics of the proton exchange

The diffusion constants for benzoic acid as well as for many other proton sources can be found in the literature. However, the values depend on the stoichiometry of the $LiNbO_3$ crystal. Moreover kinetics of the proton exchange strongly depends on the technique of fabrication used.

The diffusion coefficient of APE and SPE waveguides can be well predicted by Arrhenius equation:

$$D = D_0 e^{-\frac{E_a}{kT}}, \tag{1.4}$$

where T is the temperature of the exchange and k is the Boltzmann constant. E_a is the activation energy and D_0 is a maximum diffusion coefficient at $T = \infty$. This equation can be rewritten as:

$$\log D = -\frac{E_a}{kT} \log e + \log D_0. \tag{1.5}$$

On the other hand the waveguide depth can be described by the following function:

$$\log d = \alpha \log t + \beta. \tag{1.6}$$

And, thus, diffusion coefficients can be established from plots of optically estimated diffusion depths versus time.

Speaking about the time of the exchange, we should mention that no influence on the maximal δn_e was noticed with long-lasting proton exchange. Only the waveguide depth is changed. This fear was based on assumption of possible annealing effects.

1.5.4 Influence of humidity on the waveguide properties

The amount of the dissociated protons in the pure melted BA is relatively small. On the contrary, lithium benzoate salt totally dissociates in the acid. Therefore a small amount of the LB is sufficient to decrease significantly the proton exchange rate between the melt and the substrate. For this reason the concentration of LB in BA is not high (between 0 and 5%) but can change essentially the properties of the waveguide.

Thus the proton exchange is very sensible to the presence of water in the proton source, i.e experience showed that even atmospheric variation of the humidity can make the fabrication process completely irreproducible. In other words, the realized waveguides have different properties even if the fabrication temperature and the proton source composition are the same. There is no clear point of view on this problem. But the current hypothesis is that the presence of small amount of water (or humid air) can significantly change the dissociation rate of the benzoic acid. This results in different ratios between Li ions and the protons.

Thus even a good precision of weighting of the BA and LB powders becomes useless if we do not control the humidity during the fabrication procedure. The wet powders or ampule or even the atmospheric humidity can add the extra H_2O to the source, which can finally change the ratio between Li and the protons in quite dramatic manner. Consequently the proton exchange rate between the substrate and the source is modified too.

This affects the reproducibility of the proton exchange technique and, therefore, demands the strict control of the humidity during the fabrication procedure.

1.6 Crystalline structure of proton exchanged waveguides

Structural analysis of proton exchanged waveguides was found to be essential. The reason is that the optical waveguides may have similar index profiles but very different propagation losses or nonlinear properties. Knowledge of the crystalline properties of the exchanged layer is necessary to understand these differences. However, even after more than 30 years of research and development of this technique there is still some lack of knowledge concerning the correlations between structural and optical properties of proton exchanged waveguides.

Replacement of Li ions by the protons leads to a deformation of the initial crystalline structure of $LiNbO_3$. Lattice parameters a and c of the relaxed $Li_{1-x}H_xNbO_3$ are bigger compared to the substrate ones.[96] Such modifications can be measured by X-ray diffraction method (more details are given in section 2.3).

Indeed, proton exchanged waveguides can be composed of several different crystallographic phases with their specific parameters a and c different from the bulk crystal.[97] After the analysis of many waveguides fabricated with different exchange and annealing parameters, seven crystallographic phases, α, κ_1, κ_2, β_1, β_2, β_3, β_4, of $Li_{1-x}H_xNbO_3$ were found possible in single-crystal proton-exchanged waveguides. Under certain fabrication parameters one, two or even three single crystalline $Li_{1-x}H_xNbO_3$ phases, organized as individual layers, can be present in the waveguide[98]. They can have very different optical properties and besides that, the strain and stresses present at the interfaces, are modifying the waveguide properties. I will describe how to calculate the strains induced by the proton exchange in the the paragraph dedicated to the crystalline deformations in chapter 2. But now let us concentrate on the optical properties of different crystalline phases.

Figures 1.14 and 1.13 show the phase diagrams of X- and Z-cut $LiNbO_3$, which are the plots of the maximum index change measured at $\lambda = 633\,\text{nm}$ as a function of deformation ε normal to the crystal surface, i.e. a change of the spacing d between crystallographic planes parallel to the surface of the substrate. The deformation in this case is defined as $\varepsilon = (d - d_0)/d_0$, where d_0 is the spacing between the planes in the unmodified $LiNbO_3$ and d is the spacing in a given exchanged layer.

The α phase presents the weakest δn_e and strain. This crystallographic phase can be obtained by SPE or APE. The corresponding waveguides have very low loss $< 0.5\,\text{dB/cm}$. The nonlinear and electro-optic coefficients are practically identical to that of the substrate.

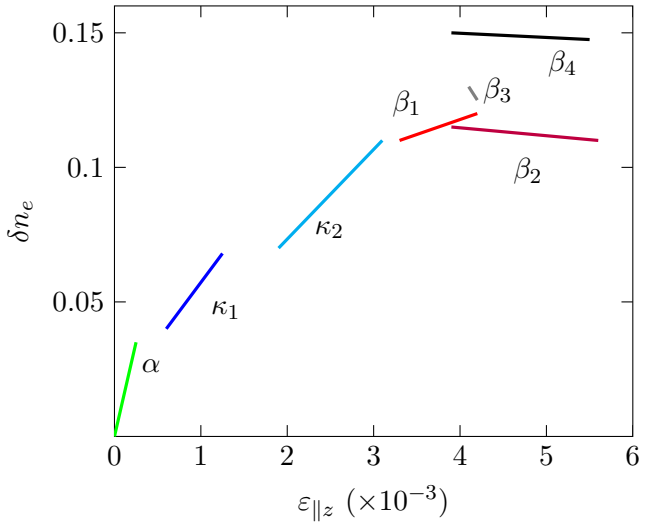

FIGURE 1.13: Phase diagram for Z-cut $LiNbO_3$.[99]

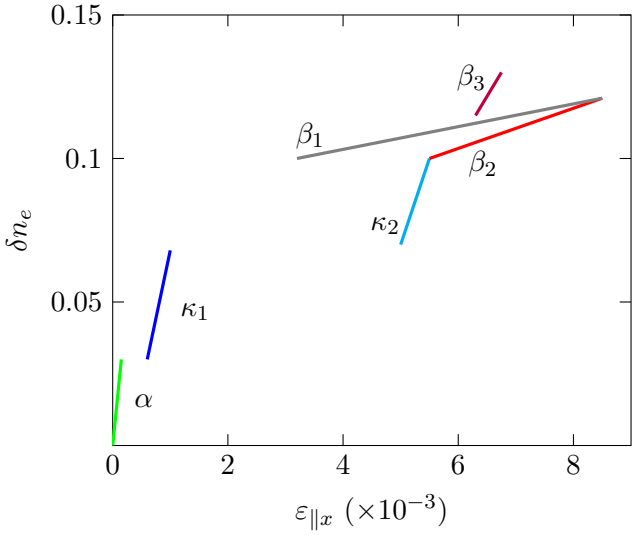

FIGURE 1.14: Phase diagram for X-cut $LiNbO_3$.[100]

The greatest increase of δn_e is common for β phases (figure 1.13). This family of crystallographic phases introduces high deformation in exchanged layer due to lattice mismatch. Phases β_2, β_3 and β_4 were found to have an extremely low nonlinear coefficient d_{33} while β_1 demonstrates much higher nonlinearity: $d_{33}(\beta_1) \approx 0.55 d_{33}$.

The phases β_3 and β_4 can be obtained by using different from BA proton sources for fabrication (pyrophosphoric acid for example).[98,99] As we are working with BA only, these phases are of no interest. Using only benzoic acid melts for waveguide fabrication, only β_1 and β_2 can be obtained. The propagation losses vary from 0.5 dB/cm in the pure β_1 to 1 dB/cm in β_2 with an increase of the strains.

An unclear question is about phases κ_1, κ_2, which are positioned between α and β phases. They are characterized by lower deformation ε_{33} than β phases and have δn_e

in the range between 0.04 and 0.01. It was reported in the literature[98] that these phases cannot be obtained by a direct proton exchange and can be found in exchanged waveguides only after annealing. Another way to fabricate the waveguides directly with κ phases is VPE.[25] As we have already mentioned, VPE waveguides were of interest as they demonstrated maintained nonlinear properties and high optical confinement at the same time. However, an absence of reproducibility is the reason why no functional devices have been reported to date. In this work we clearly show that the crystallographic phase κ_2 can be obtained by direct exchange. However, this involved a development of a new fabrication technique and was actually a part of the subject of this research work.

As we have seen on the phase diagram, some $Li_{1-x}H_xNbO_3$ phases, such as κ_2, β_1, β_2, may show very close values of δn_e. However, their optical properties are very different. That means that the waveguides should be characterised carefully and index profile measurements cannot give a definite answer about the optical quality of the waveguide. Thus a complex analysis of structural and optical characteristics is needed.

1.7 Channel waveguide fabrication by proton exchange

Before starting with channel waveguides, we first dealt with planar waveguides where the fabrication procedure requires a simple immersion of the crystal into the melt of BA+LB. But as far as it concerns the fabrication of integrated optical devices, the light confined in channel waveguides brings more advantages. Finally, with the stripe waveguides we are able to realize more complicated and advanced optical devices on the crystal surface.

A photolithography technique known as lift-off[101] is used to fabricate channel waveguides by proton exchange technique. This involves the deposition of a mask on the surface of the crystal, which serves to prevent the exchange to take place in the covered zones. The different variants of proton exchange can be carried out and the waveguides are formed only through the openings of the mask.

The technological process of the channel waveguide fabrication is represented in figure 1.15. The first step is the deposition of a thin layer of photoresist on the clean surface of $LiNbO_3$. Photoresist is a special light-sensitive material in which a pattern can be written using ultraviolet (UV) light. Generally photoresist materials are divided into two groups: positive and negative resists. This classification is determined by the way the resist reacts to light exposure. A positive photoresist material exposed to light becomes soluble in a certain chemical developer while unexposed material remains attached to

the surface of the crystal. On the contrary, a negative photoresist becomes insoluble in the developer when it has been exposed to light.

The pattern in the resist is created by its exposition to UV light through an optical mask (figure 1.15(b)). This mask is fabricated in advance and is an opaque pattern (can be chrome) deposited on a transparent substrate (quartz). In the case of a negative photoresist, exposed regions become insoluble in the developer. Thus after chemical development only thin stripes of resist remain at the surface of the crystal (figure 1.15(c)). After that, a thin layer of silica is deposited on all the surface. The thickness of the SiO_2 should be lower than the thickness of the photoresist. Then, using another chemical solvent (remover) allows washing out all the rest of the photoresist and the SiO_2 film lying above it (figure 1.15(e)). Now we have an $LiNbO_3$ crystal ready for the proton exchange. The film of SiO_2 is resistant to the benzoic acid. The procedure of waveguide fabrication is identical to fabrication of planar waveguides. The crystal is immersed into a BA+LB melt and the channel waveguides are formed by the proton exchange through the windows opened in the SiO_2 mask (figure 1.15(f)). The last step consists in removing the SiO_2 from the surface if needed (figure 1.15(g)).

(a) Deposition of photoresist on $LiNbO_3$ substrate

(b) Alignement of mask to substrate and UV illumination

(c) Wet chemical development

(d) SiO_2 thin film deposition

(e) Removing photoresist with SiO_2 above

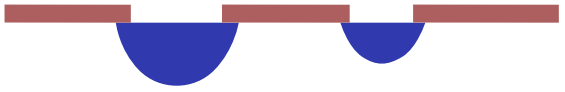

(f) The PE waveguide fabrication

(g) Removing of the SiO_2 thin film

FIGURE 1.15: Main steps of channel waveguide fabrication using photolithography technique.

Chapter 2

Theoretical background on nonlinear integrated optics

2.1 Waveguide concepts

As the main subject of this work are optical waveguides, it is appropriate at this stage to give some important definitions.

A waveguide can be defined as any structure capable of guiding the flow of electromagnetic energy in a direction parallel to its axis, while substantially confining it to a region either within or adjacent to its surface. An optical waveguide consists of a core, in which the refractive index is higher than the cladding. At this condition, the light coupled to the end face of the waveguide can be confined in the core by the total internal reflection.

Then the critical angle for the total internal reflection can be expressed from the Snell's law as $\sin\theta_c = n_{core}/n_{cladding}$. However, even if the angle θ is smaller than the critical angle, the light rays of arbitrary angles are not able to propagate in the waveguide. Each mode is associated with light rays at a discrete angle of propagation, as given by electromagnetic wave analysis.[102]

2.1.1 Electromagnetic modes

Let us consider a losseless linear dielectric planar waveguide for which the structure is infinite. Schematically it is represented in figure 2.1 where n_1, n_2 and n_3 are refractive indices. Maxwell's equations in such medium are written in terms of the electric and magnetic fields:

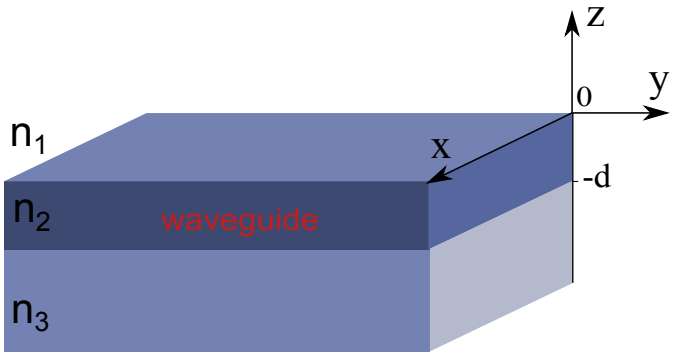

FIGURE 2.1: Schematic representation of planar waveguide

$$\vec{\nabla} \times \vec{H} = n^2 \varepsilon_0 \frac{d\vec{E}}{dt} \tag{2.1}$$

$$\vec{\nabla} \times \vec{E} = -\mu_0 \frac{d\vec{H}}{dt} \tag{2.2}$$

$$\vec{\nabla} \cdot \vec{E} = 0 \tag{2.3}$$

$$\vec{\nabla} \cdot \vec{H} = 0 \tag{2.4}$$

$$\vec{B} = \mu_0 \vec{H} \tag{2.5}$$

$$\vec{D} = \varepsilon \vec{E} \tag{2.6}$$

where $\vec{E}$ is the electric field vector, $\vec{B}$ the magnetic field vector, $\vec{H}$ the magnetic induction vector, and $\vec{D}$ the electric displacement vector.

Let us take the y-axis as the direction of propagation. The solutions are of the form:

$$\vec{E} = \vec{E} \exp i(\omega t - \vec{k} \cdot \vec{r}) = \vec{E} \exp i(\omega t - \beta y) \tag{2.7}$$

$$\vec{H} = \vec{H} \exp i(\omega t - \vec{k} \cdot \vec{r}) = \vec{H} \exp i(\omega t - \beta y) \tag{2.8}$$

As the waveguide is infinite in Ox direction there is no dependence on x ($\frac{\partial}{\partial x} = 0$).

An electromagnetic field can be considered as a sum of two polarized fields, corresponding to Transverse Electric (TE) modes with $\vec{E}$ parallel to Ox and Transverse Magnetic (TM) where $\vec{H}$ is parallel to Ox.[103]

For TE modes, one can write from Maxwell's equations:

$$\begin{cases} \dfrac{\partial^2 E_x}{\partial z^2} + (k^2 n^2 - \beta^2) E_x = 0 \\ H_z = -\dfrac{\beta}{\omega \mu_0} E_x \\ H_y = -\dfrac{1}{i\omega\mu_0} \dfrac{\partial E_x}{\partial z} \\ H_x = 0 \end{cases} \tag{2.9}$$

and for TM modes, it comes:

$$\begin{cases} \dfrac{\partial^2 H_x}{\partial z^2} + (k^2 n^2 - \beta^2) H_x = 0 \\ E_z = -\dfrac{\beta}{\omega \mu_0} H_x \\ E_y = -\dfrac{1}{i\omega\mu_0} \dfrac{\partial H_x}{\partial z} \\ E_x = 0 \end{cases} \tag{2.10}$$

Therefore, the problem comes to solving the Helmholtz's equation:

$$\frac{\partial^2 F}{\partial z^2} + (k^2 n^2 - \beta^2) F = 0, \tag{2.11}$$

where $F = E$ of H depending on polarization.

The precedent equation 2.11 for TE modes has the following forms:

$$\begin{cases} \dfrac{\partial^2 E_x}{\partial z^2} - q^2 E_x = 0, & z \geq 0 \\ \dfrac{\partial^2 E_x}{\partial z^2} + h^2 E_x = 0, & 0 \geq z \geq -d \\ \dfrac{\partial^2 E_x}{\partial z^2} - p^2 E_x = 0, & z \leq -d \end{cases} \tag{2.12}$$

where

$$q^2 = \beta^2 - k^2 n_1^2 \tag{2.13}$$

$$h^2 = k^2 n_2^2 - \beta^2 \tag{2.14}$$

$$p^2 = \beta^2 - k^2 n_3^2 \tag{2.15}$$

The constant β is called the propagation constant and is defined as $\beta = kN = kn \sin\theta$. N is the effective index of the guided mode. The guiding condition imposes the existence of a sinusoidal solution within the central layer n_2 ($h^2 \geq 0$), with evanescent waves into mediums n_1 and n_3:

$$kn_2 \geq \beta \geq kn_3 \geq kn_1 \tag{2.16}$$

Assuming boundary conditions the electric field E_x has a form:

$$E_x(z) = C \begin{cases} \exp(-qz), & 0 \leq z \leq \infty \\ [\cos(hz) - (q/h)\sin(hz)], & -d \leq z \leq 0 \\ [\cos(hd) + (q/h)\sin(hd)]\exp(p(z+d)), & -\infty \leq z \leq -d \end{cases} \tag{2.17}$$

where C is a constant. Knowing the constants of propagation β, this system of equations allows to determine the electric field profile of each guided mode.

The dispersion equation of the TE guided modes can be represented as:

$$hd = \arctan\left(\frac{q}{h}\right) + \arctan\left(\frac{p}{h}\right) + m\pi \tag{2.18}$$

where $m \geq 0$ is an integer, which defines the guided mode order.

For TM modes, we have $\vec{H} = (0, H_x, 0)$ and $\vec{E} = (E_z, 0, E_y)$. Analogically as with TE modes, the magnetic field H is given by:

$$H_x(z) = C \begin{cases} -(h/\overline{q})\exp(-qz), & 0 \leq z \leq \infty \\ [-(h/\overline{q})\cos(hz) + \sin(hz)], & -d \leq z \leq 0 \\ -[(h/\overline{q})\cos(hd) + \sin(hd)]\exp(p(z+d)), & -\infty \leq z \leq -d \end{cases} \tag{2.19}$$

with a dispersion equation:

$$dh = \arctan\left(\frac{q}{h}\frac{n_2}{n_1}\right) + \arctan\left(\frac{p}{h}\frac{n_2}{n_3}\right) + m\pi \tag{2.20}$$

The propagation constant $\beta = kN$ and thus the effective index N characterize the guided modes. The effective index is an important parameter in the characterization of optical waveguides as it can be measured directly. The thickness of the waveguide is also an important parameter that defines the optical properties of the waveguides, in particular the number of guided modes.

2.2 Second order nonlinear interactions in proton exchanged waveguides on $LiNbO_3$

The response of any material can be described as a Taylor expansion of the polarization in powers of the electric field:

$$\vec{P} = \epsilon_0(\overleftrightarrow{\chi}^{(1)}\vec{E} + \overleftrightarrow{\chi}^{(2)}\vec{E}\vec{E} + \overleftrightarrow{\chi}^{(3)}\vec{E}\vec{E}\vec{E} + ...), \tag{2.21}$$

where ϵ_0 is the vacuum permittivity and $\chi^{(n)}$ the tensor of the n-th order corresponding respectively to nonlinear process of the n-th order. Among others, the coefficient $\chi^{(1)}$, which is a linear susceptibility, is the only non negligible term at low powers of the electric field $\vec{E}$. For materials having centrosymmetric structure, the even terms are equal to zero.

Lithium niobate is a noncentrosymmetric nonlinear optical material, so $\chi^{(2)}$ is the first nonlinear term of equation 2.21. Let's have a look on the second term, which is responsible for nonlinear phenomena of the second order. We will write this term separately as follows:

$$\vec{P}^{NL} = \overleftrightarrow{\chi}^{(2)}\vec{E}\vec{E}. \tag{2.22}$$

2.2.1 Wave equation for nonlinear optical waveguide

The propagation of a light field in optical media is often described by the following propagation equation:

$$\vec{\nabla}\left(\vec{\nabla}\cdot\vec{E}\right) - \vec{\nabla}^2\vec{E} + \frac{\epsilon_r}{c^2}\frac{\partial^2\vec{E}}{\partial t^2} = -\frac{1}{\epsilon_0 c^2}\frac{\partial^2\vec{P}}{\partial t^2}. \tag{2.23}$$

In a linear isotropic source-free media, the first term of the left-hand side of this equation vanishes because the Maxwell equation $\nabla\cdot\vec{D} = 0$ implies that $\nabla\cdot\vec{E} = 0$. In a nonlinear media, this term is generally nonzero even for isotropic materials, but, fortunately, it can be dropped off for cases of interest [104]. From now on, we consider this term to be zero. Taking the Fourier transformation of equation 2.23 and using equation 2.22 for nonlinear polarization, we have:

$$\vec{\nabla}^2\vec{E} + \frac{\omega^2}{c^2}\epsilon_r\vec{E} = -\omega^2\vec{P}^{NL}. \tag{2.24}$$

Second harmonic generation (SHG) as well as spontaneous parametric down conversion (SPDC) are the three-wave-mixing nonlinear interactions. As we are working with the proton exchanged waveguides supporting only one polarization, let us consider three interacting waves at frequencies ω_1, ω_2 and ω_3 polarized along the z-axis. Taking y-axis as a direction of the light propagation, we can pass from the tensor form and write a projection of the nonlinear polarization:

$$P_z^{NL}(\omega_1) = 2\chi_{zzz}E_z(\omega_2)E_z(\omega_3). \tag{2.25}$$

The coordinate system was chosen to be the same as the orthogonal system used to define the crystallographic directions. We consider the conditions of slowly varying envelopes for guided modes

$$E_j = A_j(y)F_j(z,x)e^{-i(\omega_j t-\beta_j y)}, \tag{2.26}$$

where $A_j(y)$ is the amplitude, $F_j(z,x)$ is the amplitude of transverse part of the guided modes, k_j is the wavevector at ω_j, $j = 1,2,3$. Equation 2.24 can be written as:

$$\frac{\partial A_1(y)}{\partial y} = -\alpha_1 A_1 - i\xi\chi_{zzz}I_1 A_2(y)A_3(y)e^{i\Delta\beta y} \tag{2.27}$$

$$\frac{\partial A_2(y)}{\partial y} = -\alpha_2 A_2 - i\xi\chi_{zzz}I_2 A_1(y)A_3^*(y)e^{-i\Delta\beta y} \tag{2.28}$$

$$\frac{\partial A_3(y)}{\partial y} = -\alpha_3 A_3 - i\xi\chi_{zzz}I_3 A_1(y)A_2^*(y)e^{-i\Delta\beta y} \tag{2.29}$$

with the overlap integral between the interacting waves being:

$$I_j = \frac{\iint 2F_1(z,x)F_2(z,x)F_3(z,x)\mathrm{d}z\mathrm{d}x}{\iint F_j(z,x)F_j(z,x)\mathrm{d}z\mathrm{d}x}. \tag{2.30}$$

Here, $\Delta\beta = \beta_1 - \beta_2 - \beta_3$ is a mismatch vector. A coupling constant ξ is determined by the following expression:

$$\xi = \frac{1}{\epsilon_0 c}\sqrt{\frac{\omega_1\omega_2\omega_3}{N_1N_2N_3}}, \tag{2.31}$$

where N_1, N_2 and N_3 are the effective indices of the corresponding modes.

In particular cases for:

1. **SHG** we have $\omega_2 = \omega_3 = \omega$ and $\omega_1 = 2\omega$. For this reason the number of equations 2.27-2.29 reduces to two. The conservation of energy is defined by $2\omega = \omega + \omega$. Two input photons of the same frequency are combined to provide a third unique photon at the doubled frequency.

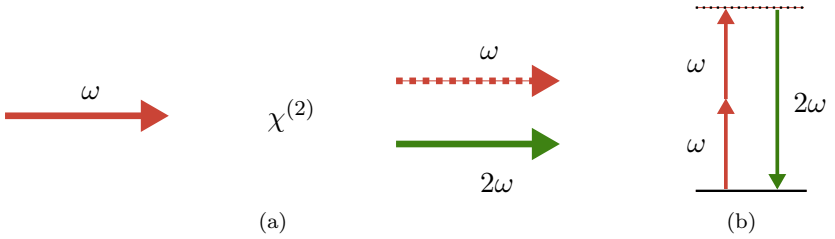

FIGURE 2.2: SHG in nonlinear material: (a) field arrangement and (b) energy-level diagram.

2. **SPDC** we have $\omega_1 = \omega_p$, $\omega_2 = \omega_s$ and $\omega_3 = \omega_i$. A pump photon can couple to a quantum state and be converted in two photons *signal* and *idler*. The energy conservation $\omega_p = \omega_s + \omega_i$ and the conservation of momentum $\beta_p = \beta_s + \beta_i$ are the conditions.

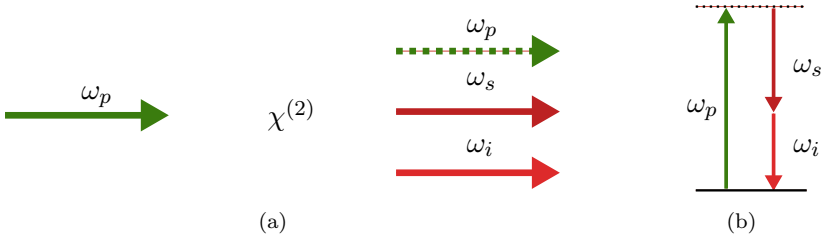

FIGURE 2.3: SPDC in nonlinear material: (a) field arrangement and (b) energy-level diagram.

2.2.2 Problem of phase-matching

We will discuss the problem of phase-matching regarding the example of SHG (see figure 2.2). Let us consider a mismatch vector equal to zero:

$$\Delta\beta = \beta_{2\omega} - 2\beta_{\omega} = 0 \tag{2.32}$$

Assuming the input field to be constant, which is reasonable if the conversion into the SH field is not too large, the amplitude of the signal 2ω increases linearly as function of the propagation distance y. In other words, we have the condition of perfect phase matching. Equation 2.32 can be rewritten as

$$\frac{2\pi n_{2\omega}}{\lambda_{2\omega}} - \frac{4\pi n_{\omega}}{\lambda_{\omega}} = 0, \tag{2.33}$$

or, remembering that $2\lambda_{2\omega} = \lambda_{\omega}$, we get the condition

$$n_{2\omega} = n_{\omega}. \tag{2.34}$$

So, if we want the most effective conversion efficiency, the refractive index of the nonlinear material should be the same at both ω and 2ω. For most optical materials, as well as for $LiNbO_3$, the refractive index increases with the increase of the frequency (figure 2.4).

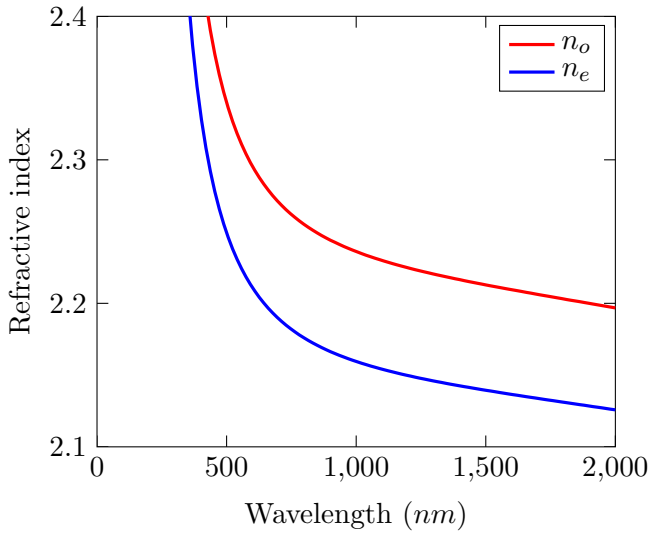

FIGURE 2.4: Ordinary and extraordinary refractive indices of $LiNbO_3$ at room temperature as a function of wavelength.

This means that the phase matching condition cannot be satisfied. The amplitude of the second harmonic field is then given by integrating equation 2.27 from $y = 0$ to $y = L$, where L is the propagation length in the considered nonlinear media.

The relation between the intensity and field amplitude is given by the following expression:

$$I_i = \frac{1}{2} n_i \epsilon_0 c \left|A_i\right|^2, \qquad i = 1, 2, 3. \tag{2.35}$$

Therefore, the intensity at ω_s is proportional to

$$I_i \sim \left|\frac{e^{i\Delta\beta L} - 1}{i\Delta\beta}\right|^2 = L^2 \frac{\sin^2(\Delta\beta L/2)}{(\Delta\beta L/2)^2} \equiv L^2 \operatorname{sinc}^2\left(\frac{\Delta\beta L}{2}\right). \tag{2.36}$$

Naturally, after the maximum of the intensity at $\Delta\beta = 0$ we have a destructive interference after a characteristic distance called the coherence length, which is defined

as

$$L_c = \frac{2\pi}{\Delta\beta} \tag{2.37}$$

2.2.3 Quasi-Phase-Matching

One of the most efficient way to achieve the phase matching is based on a periodic inversion of the nonlinear coefficient along the propagation axis. In practice, this is ensured by a periodical inversion of the polarisation of $LiNbO_3$, leading to so-called periodically poled lithium niobate (PPLN). In figure 2.5 we can see a channel waveguide fabricated on a PPLN crystal. The domains polarized along the z-axis, but with opposite directions form the grating structure with a period Λ.

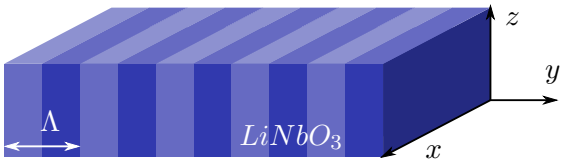

FIGURE 2.5: PPLN waveguide designed to achieve QPM condition.

The main advantages of QPM are that we can use the highest nonlinear coefficient, we can work at any desired temperature and, in principle, we can achieve quasi-phase-matching (QPM) for any wavelength limited only by the transparent range of the crystal.

The PPLN grating is created on purpose to compensate the phase mismatch. The period of this grating relates to the coherence length as $\Lambda = 2L_c$. Thus, every time when the field amplitude of the generated wave is about to decrease after the coherence length, the sign of the nonlinear coefficient changes to the opposite and, therefore, the field amplitude continues to grow.

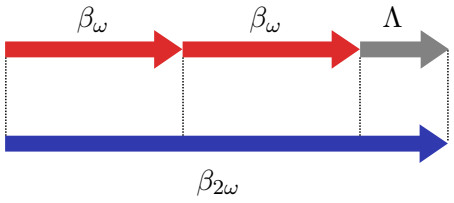

FIGURE 2.6: Compensation of the phase mismatch for SHG interaction, i.e. for achieving the momentum conservation condition.

In figure 2.7, we present a comparison of the spatial variation of the amplitude of the generated wave as a function of the propagation distance in the nonlinear optical material.

We have three conditions: perfect phase-matching, QPM and phase mismatch. We have a linear increase of the amplitude with the distance when $\Delta k = 0$ and, so, interacting

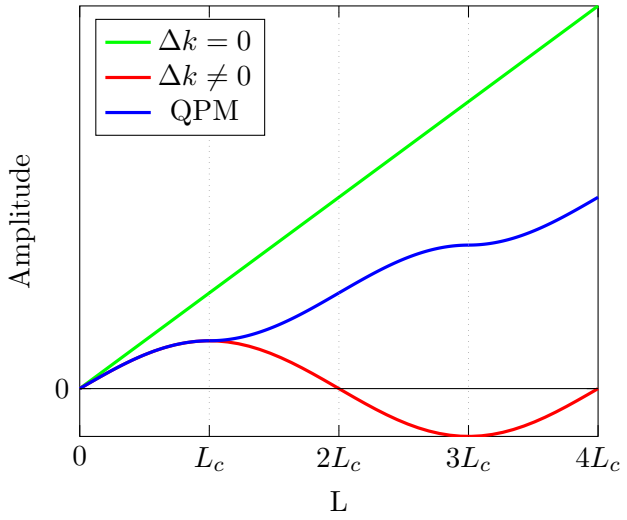

FIGURE 2.7: The variation of the field amplitude with the distance of wave propagation.

waves are in phase. When $\Delta k \neq 0$, the amplitude oscillates periodically without any average augmentation. But if the orientation of the optical axis c (on the fig.2.5 it is parallel to z) is changed periodically with the period of $2L_c$, the field amplitude is growing monotonically.

2.2.4 Measurement of SHG and SPDC efficiency

We have already mentioned that the efficiency of the desired nonlinear interaction in the nonlinear media strongly depends on the phase-matching conditions. Also in many cases, the overlap integral (equation 2.30) between the interacted waves plays a great role in the conversion efficiency. If we want to measure quantitatively the ability of the nonlinear optical system to convert the pump photons into signal, we can use a following dimensionless expression

$$\eta = \frac{P_{2\omega}(L)}{P_{\omega}(0)}, \tag{2.38}$$

which defines the total conversion efficiency. Therefore, experimentally we have to measure with accuracy the injected fundamental power and the power of the generated second harmonic.

The efficiency of SHG interaction increases linearly with the pump intensity and quadratically with the interaction length as stated by equation 2.36. Thus, we can normalize equation 2.38 in following manner:

$$\eta = \frac{P_{SHG}}{P_p^2 l^2}. \tag{2.39}$$

By measuring both P_{SHG} and P_p we can estimate the conversion efficiency.

2.2.5 Measurement of SPDC efficiency

Analogically with SHG, we can rewrite expression 2.38 for SPDC:

$$\eta = \frac{P_s}{P_i P_p l^2}, \tag{2.40}$$

where $P_{s,i,p}$ are the powers of the signal, idler and pump fields, respectively.

2.2.6 Comparison of SHG and SPDC characterization

The SHG power is defined by following expression:

$$P_{SHG} = 4\omega_p^2 P_p^2 l^2 \frac{\mu_0 \chi_{eff}^2}{c S_{eff} n_p^2 n_{SHG}}, \tag{2.41}$$

where χ_{eff} is the nonlinear coefficient, S_{eff} is an effective area through which the interaction takes place. They are related by

$$\frac{\chi_{eff}^2}{S_{eff}} = \frac{\left(\iint 2\chi F_p^2(x,y) F_{SHG}(x,y)\mathrm{d}x\mathrm{d}y\right)^2}{\left(\iint F_p^2(x,y)\mathrm{d}x\mathrm{d}y\right)^2 \iint F_{SHG}^2(x,y)\mathrm{d}x\mathrm{d}y}, \tag{2.42}$$

where $F_{p,SHG}$ are transverse distributions of the amplitudes of both the pump and SH modes.

On the other hand, we can express the signal power for SPDC as

$$P_s = 4\omega_s^2 P_p P_i l^2 \frac{\mu_0 \chi_{eff}^2}{c S_{eff} n_p n_s n_i} \tag{2.43}$$

where

$$\frac{\chi_{eff}^2}{S_{eff}} = \frac{\left(\iint 2\chi F_p(x,y) F_s(x,y) F_i(x,y)\mathrm{d}x\mathrm{d}y\right)^2}{\iint F_p^2(x,y)\mathrm{d}x\mathrm{d}y \iint F_s^2(x,y)\mathrm{d}x\mathrm{d}y \iint F_i^2(x,y)\mathrm{d}x\mathrm{d}y}. \tag{2.44}$$

Here, $F_{p,s,i}$ are the transverse distributions of the amplitudes of the pump, signal and idler modes. P_i is the idler power and $n_{p,s,i}$ are the corresponding effective indices. From equation 2.42 and 2.44 we can compute the following relation:

$$\frac{P_s}{P_p P_i l^2} = \frac{P_{SHG}}{P_p^2 l^2} \tag{2.45}$$

2.3 Calculation of the deformation induced by the proton exchange

2.3.1 Deformations in proton exchanged layers: a quick review

In planar waveguides a thin surface layer of several microns is modified and every unit cell in this exchanged layer tends to broaden in all directions due to the lattice constants mismatch. This leads to induced crystalline stresses and strains.

If the depth of protonated layer is negligibly thin we can consider all the deformations to be elastic in the plane of the surface. The crystal lattice in the waveguide cannot relax laterally as it is restrained by the substrate. The only possibility is to deform the surface direction as it is shown on the figure 2.8. Consequently this can lead to a deformation of the initial symmetry of the crystal.

Depending on the crystallographic directions, the resulting influence of the strains on the crystallographic symmetry of the waveguide is different. The lattice parameter c is changed for Z-cut $LiNbO_3$ while a remains unaffected. So the initial hexagonal cylinder, as we can imagine a unit cell of $LiNbO_3$, extends along the Z-axis. In this case the uniaxial symmetry of the crystal is preserved for Z-cut waveguide in spite of the modified constant c. Another situation is for X-cut where the exchanged layer is a biaxial material (figure 2.8(a)). The strains induced by proton exchange force the unit cell to stretch the hexagon vertically and the symmetry is broken.

We can define the modified crystalline unit cell constants for Z-cut $LiNbO_3$ as:

$$a'_x = a_x = a_h \qquad a'_y = a_y = \frac{\sqrt{3}}{2} a_h, \tag{2.46}$$

and for X-cut as follows:

$$c' = c \qquad a'_y = a_y = \frac{\sqrt{3}}{2} a_h. \tag{2.47}$$

As we can see from the figure 2.8, $a'_x \neq a_x$ for X-cut and $c' \neq c$ for Z-cut.

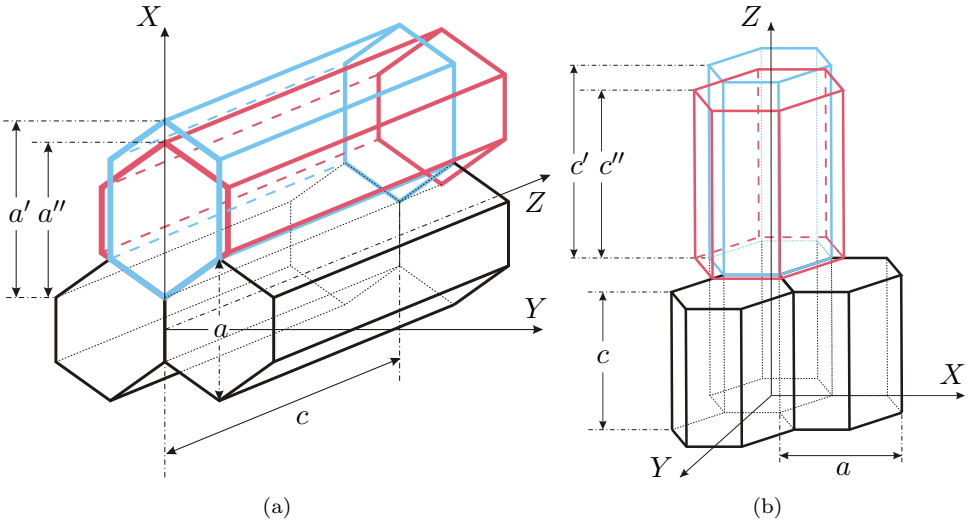

FIGURE 2.8: Mechanism of deformation for (a) X-cut and (b) Z-cut $LiNbO_3$.

2.3.2 General definition of strain and stress

Generally, all the lattice constants of the crystalline material can be calculated using Bragg's law:

$$n\lambda = 2d\sin\theta, \tag{2.48}$$

where d is the spacing between the crystallographic planes of a given family, θ is the angle of the diffracted beam measured with the help of X-Ray Diffractometer (XRD), λ is the wavelength of the incident X-ray radiation used for the measurements. The relation between the inter-planar distances and the lattice constants are well known. For a trigonal crystallographic system, we have the following relation:

$$\frac{1}{d_{hkl}^2} = \frac{4}{3a^2}\left(h^2 + k^2 + hk\right) + \frac{l^2}{c^2}, \tag{2.49}$$

where h, k, l are the Miller indexes, a and c are the lattice constants.

If d' is the distance between atomic planes in strained volume of the material, we can measure experimentally the strain normal to these planes by measuring the diffraction peak position θ. If we know d for the unstrained volume of the material, the strain can be defined as:

$$\varepsilon = \frac{d' - d}{d} \tag{2.50}$$

So, the deformation normal to the surface can be measured by a simple comparison of the inter-planar spacing of strained and unstrained materials. In case of planar proton exchanged waveguides, we have a thin layer of several microns in depth. A penetration depth of X-ray radiation is usually slightly higher ($\sim 20\,\mu$m for $LiNbO_3$) and, therefore, this permits to register the diffraction peaks for unstrained substrate and strained waveguiding layer at once.

In a strained material, the stress is at any point linearly proportional to the strain, assuming that the strain is small. The most general linear relation between the stress and the strain tensor is given by the following Hook's law:

$$\boldsymbol{\sigma} = \mathbf{C}\boldsymbol{\varepsilon}, \tag{2.51}$$

where $\boldsymbol{\sigma}$ and $\boldsymbol{\varepsilon}$ are the stress and strain tensors, qnd C is the so-called stiffness tensor. In the case of $LiNbO_3$, this law can be rewritten in tensor form considering an appropriate hexagonal crystallographic symmetry:

$$\begin{pmatrix} \sigma_1 \\ \sigma_2 \\ \sigma_3 \\ 2\sigma_4 \\ 2\sigma_5 \\ 2\sigma_6 \end{pmatrix} = \begin{pmatrix} c_{11} & c_{12} & c_{13} & c_{14} & 0 & 0 \\ c_{12} & c_{11} & c_{13} & -c_{14} & 0 & 0 \\ c_{13} & c_{13} & c_{33} & 0 & 0 & 0 \\ c_{14} & -c_{14} & 0 & c_{44} & 0 & 0 \\ 0 & 0 & 0 & 0 & c_{44} & c_{14} \\ 0 & 0 & 0 & 0 & c_{14} & c_{66} \end{pmatrix} \begin{pmatrix} \varepsilon_1 \\ \varepsilon_2 \\ \varepsilon_3 \\ 2\varepsilon_4 \\ 2\varepsilon_5 \\ 2\varepsilon_6 \end{pmatrix} \tag{2.52}$$

The values of the coefficients are well known for $LiNbO_3$ and can be found in the literature.[105–107] Unfortunately, this is not the case for the $Li_{1-x}H_xNbO_3$ phases.

2.3.3 Measurement of strains in PE waveguides

Now we will try to characterize the deformations in the exchanged thin layer of the crystal. The measurement of the strains is an essential characterization step as it helps defining the crystalline phases present in proton exchanged waveguides.

Before we will make some simplifications. The first assumption is that the crystal was exchanged on both sides, i.e. the slab waveguides of the same depth were fabricated on all the surface of the crystal and there are no strain or deformations caused by a curvature of the crystal. And last, we suppose that the interface between the exchanged layer and the substrate is parallel to the surface. These considerations allow to reduce

the number of equations 2.51 to three, because the terms corresponding to shear strains are negligible, i.e. $\varepsilon_4 = \varepsilon_5 = \varepsilon_6 = 0$.

Assuming the deformations to be small we can redefine the expression 2.50 for the crystalline strains by deriving the Bragg's law (equation 2.48):

$$\varepsilon = \frac{\Delta d}{d} = -\Delta\theta \cot\theta \tag{2.53}$$

For simplicity, we now use a 'native' hexagonal coordinate system with axes 1, 2 and 3 (section 1.1.1). Differentiating equation 2.49 and considering expression 2.53, we have a more general relation between the deformations (along axes 1, 2 and 3) and d_{hkl}:

$$\begin{aligned} -\frac{\Delta\theta_{hkl}}{d_{hkl}^2 \cdot \tan\theta_{hkl}} = &-\frac{4}{3\sqrt{3}a^2}\left(h^2 + k^2 + hk\right)\Delta\phi + \\ &+\frac{4}{3a^2}\left(h^2\varepsilon_1 + k^2\varepsilon_2 + \frac{hk}{2}(\varepsilon_1 + \varepsilon_2)\right) + \frac{l^2}{c^2}\varepsilon_3, \end{aligned} \tag{2.54}$$

where $\Delta\phi$ is a possible change of the angle between the crystallographic axes 1 and 2. For the initial nonmodified crystal symmetry, the angle ϕ is equal 120°. The values $\varepsilon_1 = \Delta a_1/a_1$, $\varepsilon_2 = \Delta a_2/a_2$ and $\varepsilon_3 = \Delta a_3/a_3$ are the deformations along the corresponding crystallographic axes. If $\Delta\phi$ is known for three atomic plans (hkl), we can successfully determine all strains ε_1, ε_2 and ε_3 .

Now, let's take a look to particular cases. We are interested in two crystal orientations: Z-cut and X-cut.

The crystal symmetry is not modified for Z-cut $Li_{1-x}H_xNbO_3$ crystal as we have seen from the deformation model (figure 2.8) and, thus, $\phi = 120°$ or $\Delta\phi = 0$. The atomic planes (00.12), (108) and (11.12) can be chosen for determination of the strains. For the planes (00.12), which are parallel to the surface, we have the simplest case

$$\varepsilon_3 = -\frac{\Delta\theta_{00.12}}{\tan\theta_{00.12}} = -\Delta\theta_{00.12} \cdot \cot\theta_{00.12}. \tag{2.55}$$

For the two others we have

$$\frac{4}{3a^2}\varepsilon_1 + \frac{64}{c^2}\varepsilon_3 = -\frac{\Delta\theta_{108} \cdot \cot\theta_{108}}{d_{108}^2}, \tag{2.56}$$

$$\frac{2(\varepsilon_1 + \varepsilon_2)}{a^2} + \frac{144\varepsilon_3}{c^2} = -\frac{\Delta\theta_{11.12} \cdot \cot\theta_{11.12}}{d_{11.12}^2}. \tag{2.57}$$

Measuring $\Delta\theta$ of the proton exchanged layer with the help of X-ray diffraction method, we can can calculate all the deformations. For X-cut $Li_{1-x}H_xNbO_3$ crystal we have $\Delta\phi =\neq 0$. In addition the basic x-plane is not perpendicular to any crystallographic axis. The deformations can be determined from the following expressions

$$\frac{5\varepsilon_2 + \varepsilon_1}{6} = -\Delta\theta_{220} \cdot \cot\theta_{220}, \tag{2.58}$$

$$\frac{4\varepsilon_2 - \varepsilon_1}{3} = -\Delta\theta_{030} \cdot \cot\theta_{030}, \tag{2.59}$$

$$-\frac{\Delta\theta_{220}\cot\theta_{220}}{d^2} + \frac{36\varepsilon_3}{c^2} = -\frac{\Delta\theta_{226} \cdot \cot\theta_{226}}{d_{226}^2}. \tag{2.60}$$

This is the general method allowing to measure all the deformations in the crystal.

However in most cases, information about the deformation normal to the surface is sufficient to distinguish all the crystallographic phases present in the exchanged waveguides.

2.4 Hybrid modes in waveguides fabricated on $LiNbO_3$

As we know the PE waveguides support only one polarization because the proton exchange increases only the extraordinary refractive index and decreases the ordinary one. For this reason the PE waveguides work also as polarizing filters.

The relative permittivity tensor of $LiNbO_3$ has the form:

$$\boldsymbol{\epsilon_r} = \begin{pmatrix} \epsilon_{11} & 0 & 0 \\ 0 & \epsilon_{11} & 0 \\ 0 & 0 & \epsilon_{33} \end{pmatrix}, \tag{2.61}$$

where $\epsilon_{11} = n_o^2$ and $\epsilon_{33} = n_e^2$. Proton exchange modifies this tensor in the exchanged volume of the crystal in two ways. The composition modification modifies the values of n_o and n_e and the stresses induced by the lattice deformation are transformed in index variations through the elasto-optic effect and a combination of the piezo-electric and the electro-optic effects.

This second part of the variation of the permittivity in function of the deformation is given by:

$$\Delta\boldsymbol{\epsilon_r} = \mathbf{PS} - \mathbf{R}(\boldsymbol{\epsilon_r}\mathbf{P_{pz}}\mathbf{S}), \tag{2.62}$$

where $\mathbf{S}$ is the strain tensor and $\mathbf{P}$ the elasto-optic tensor, $\mathbf{R}$ the electro-optic tensor, and $\mathbf{P_{pz}}$ the piezoelectric tensor of $LiNbO_3$. Considering the symmetries of Z-cut waveguides, we can deduce the following relations : $S_4 = S_5 = S_6 = 0$ and $S_1 = S_2$. The resulting $\Delta\boldsymbol{\epsilon_r}$ matrix has the form:[108]

$$\Delta\boldsymbol{\epsilon_r} = \begin{pmatrix} \Delta\epsilon_{11} & 0 & 0 \\ 0 & \Delta\epsilon_{11} & 0 \\ 0 & 0 & \Delta\epsilon_{33} \end{pmatrix}, \tag{2.63}$$

while for X-cut waveguides $S_4 = S_5 = S_6 = 0$ is still valid, but $S_1 \neq S_2$, therefore

$$\Delta\boldsymbol{\epsilon_r} = \begin{pmatrix} \Delta\epsilon_{11} & 0 & 0 \\ 0 & \Delta\epsilon_{22} & \Delta\epsilon_{23} \\ 0 & \Delta\epsilon_{32} & \Delta\epsilon_{33} \end{pmatrix}. \tag{2.64}$$

We see that the exchange influences both permittivities of the waveguide. Moreover, in the case of X-cut crystals, we see that it appears some nondiagonal elements , due to strain and stresses. This indicates that the coordinate system now does not coincide with the optical axes of the waveguide, i.e. the optical axes of the exchange layer are rotated relatively to the coordinate system of the bulk crystal. This is not a surprise if we remember that the PE X-cut $LiNbO_3$ on the surface becomes a biaxial material.

Therefore waveguides realized on these two crystal orientations can behave quite differently. On Z-cut substrate the waveguide remains uniaxial, with principal axis identical to those of the substrate. Ordinary and extraordinary polarized fields are independent, and waveguides support TM modes only.

On the contrary, the ordinary and extraordinary polarizations are not independent for waveguides on X-cut crystals where the exchanged layer is biaxial and its principal axis (no longer determined by the crystallographic axes) are rotated in relation to the substrate axis. The modes supported by such waveguides are called hybrid modes and have both ordinary and extraordinary components.[108–112]

Therefore hybrid modes behave differently depending on the value of their effective indices.

If the effective index of a given mode is higher than the ordinary index of $LiNbO_3$ ($N_{eff} > n_o > n_e$), the mode propagates without any problems as both polarizations are perfectly guided.

When the effective index of the propagating mode is between the ordinary and extraordinary idices ($n_o > N_{eff} > n_e$), the waveguiding condition is satisfied only for one polarization: TE for X-cut waveguide. Since the TE and TM polarizations are not independent, the mode radiates into the substrate.

Hybrid modes are not desired in the waveguides as they add extra propagation losses due to the mode radiation.[113] This effect becomes more significant when fabricating the PE wavegiudes with high δn_e.[114] These waveguides are usually characterized by rather high concentration of the protons and, consequently, the induced strains. Therefore the crystalline symmetry in such waveguides is strongly modified and leads to increased coupling between the polarizations.

Chapter 3

Highly confining waveguides on X-cut $LiNbO_3$

In this part of the work I will present a new fabrication technique based on proton exchange, which aims at producing highly confining nonlinear waveguides with preserved electro-optic and nonlinear properties. We refer to this technique as High Index Soft Proton Exchange (HISoPE). Part of this work was carried out, in the frame of the phoXcry project (ANR-09-NANO-004-03).

3.1 The PhoXcry project

The phoXcry project was aiming at demonstrating the remarkable potential lying behind the integration of micro- and nano-structures into active integrated optical devices made on $LiNbO_3$, an appealing material owing to its particularly high acousto-optic, electro-optic, piezoelectric, and optical nonlinear properties.

The project was run by three French laboratories and one industrial partner: FEMTO-ST in Besançon, IEMN in Lille, LPMC in Nice and Thales Research and Technology (TRT). At LPMC we concentrated our efforts on one of the objectives of phoXcry, which was to design, fabricate and test a highly efficient electro-optic modulators based on $LiNbO_3$ photonic crystals. The typical design of an intensity modulator is given in figure 3.1. The idea here was to take advantage of slow-light phenomena linked to the periodicity of the nano-structure to obtain ultra-compact, large bandwidth modulators with low driving voltages.

This chapter presents the development of the new waveguide fabrication technique that was studied to optimize the coupling between the optical circuit and the photonic crystal, as well as the optical characterization of the produced circuits and test devices.

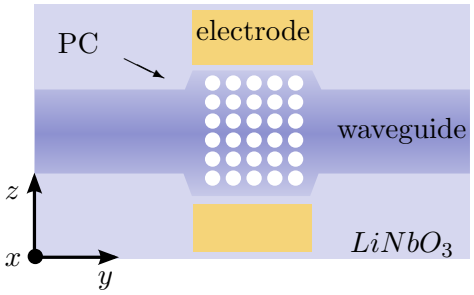

FIGURE 3.1: Schematic design of a compact EO intensity modulator on X-cut $LiNbO_3$.

3.1.1 Photonic crystal on $LiNbO_3$

Nanostructuration of $LiNbO_3$ is not easy at the submicron scale. Focused ion beam (FIB) etching[115], e-beam lithography followed by wet etching[116], reactive ion etching (RIE)[117] and femto-second laser ablation[118] are used to structure $LiNbO_3$. All these processes are limited by redeposition phenomena and the form factor (depth/diameter) is limited by the maximum angle that one can reach. For RIE, this limit angle is around 73° for a hole diameter of 6 μm (figure 3.2(b)). FIB milling is considered to be the most efficient way to produce nanoscale holes in $LiNbO_3$. However, as we can see in figure 3.2(a), the maximum depth of the holes with apertures around 300 nm is 1.5 μm which is small compared with the size of the modes of the waveguides realized in $LiNbO_3$ with commercial techniques (titanium in-diffusion or APE, see chapter 1).

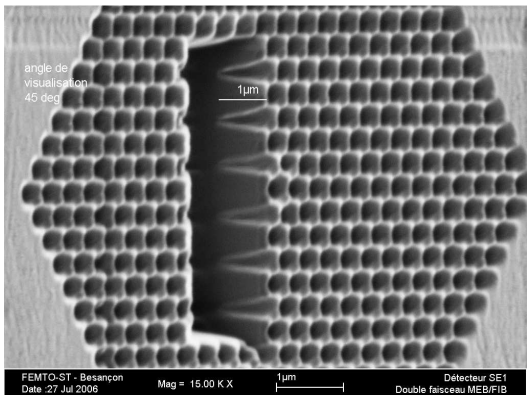

(a) FIB milling on X-cut surface

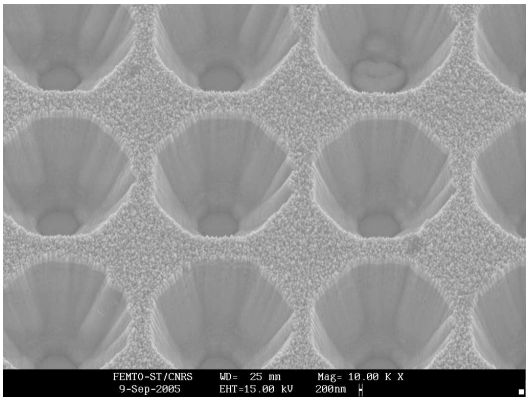

(b) RIE on Y-cut surface

FIGURE 3.2: Scanning electron microscope (SEM) images of nanostructured $LiNbO_3$ (made at FEMTO).

3.1.2 Optical waveguide fabrication

In order to solve this problem, we proposed to realize an optical waveguide that confines the light in the direction perpendicular to the surface in a layer thinner than the depth of the holes of the achievable photonic crystals. APE and SPE techniques are not able to do that due to the small value of the index change they produce, $\delta n_e \leqslant 0.03$. The so-called PE waveguides can confine the mode at telecom wavelength in a layer thinner than one micron. But, as we have mentioned, the PE waveguides suffer from severe reduction of the nonlinear and electro-optical coefficients.[17,74,99,119–121] VPE waveguides which present $\delta n_e = 0.1$ without total degradation of the nonlinear and electro-optical coefficients could have been an excellent way out. But the dramatic lack of reproducibility we observed[30] makes this technique useless. We therefore proposed to use the HISoPE fabrication process.

As the obtained waveguides have some similarities with the waveguides produced by the VPE process, I will first describe the fabrication procedure and analyze the influence of the different parameters on the reproducibility. Then I will discuss the linear and nonlinear optical properties of planar and channel waveguides fabricated using the HISoPE technique.

3.2 Modified proton exchange technique HISoPE

3.2.1 Fabrication protocol

The HISoPE technique allows achieving a high value of $\delta n_e \geq 0.09$ but with a proton exchange process which is softer than for standard PE waveguides and therefore introduces less strains into the waveguiding layer.

It consists in performing a proton exchange using a BA+LB melt with a percentage of lithium benzoate ρ_{LB} as high as possible but satisfying the relation: $\rho_{LB} < \rho_t$, as it is shown in figure 3.3. The idea is to 'move' far from PE waveguide concentration, but not to pass the threshold above which SPE waveguides are realized.

The rest of the procedure is similar to what is reported in section 1.2.1 but instead of using Pyrex ampules I used a zirconium container with different sample holders designed specially for the proton exchange process. Zirconium is known for its chemical resistance, notably to organic acids.[122] The advantage of a reusable container offering the possibility to process small samples as well as 3 inch wafers is obvious. In addition, the rigidity of this container allows to work with temperatures higher than the one possible with Pyrex ampules which brake above 300°C because of the vapor pressure of the benzoic acid.

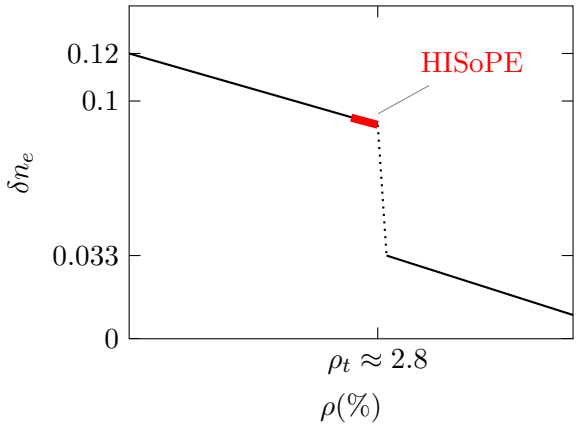

FIGURE 3.3: Working concentration for X-cut HISoPE waveguide fabrication at $300°C$. The threshold concentration for X-cut $LinNbO_3$ for this temperature is around 2.8%.

In order to reach the desired reproducibility, I have modified the fabrication procedure, which now consists of the following steps:

1. Preparation of the sample

   When small samples are suitable for systematic preliminary experimental tests, a diamond wire saw is used to cut the wafer in small pieces. Ethanol and distilled water are used to clean the surface of the samples. An ultrasonic bath helps to make the cleaning procedure more efficient.

2. Preparation of the benzoic acid and lithium benzoate powders

   BA and LB powders are dried under vacuum at 30°C during 1 hour. Then the bottles with powders are rapidly closed and placed in a glove box with controlled atmosphere where BA and LB are mixed with the needed percentage using a precision balance.

3. Assembling the container with a sample and chemical reagents

   The part of the container are also dried and placed in the glove box as well as the sample to process. The container is filled with the powder mixture and the samples are fixed in the holder which allows maintaining them in the top part of the container, out of the powder. All the assembling procedure are carried out in the glove box (figure 3.4). Finally, the two parts of the container are attached by clamps using an Al sealing ring for pressure tightness (figure 3.5).

4. Pumping the container

   A primary vacuum pump is then used to create the vacuum inside the container while the container is heated up to 50°C to accelerate the process. When a vacuum of 10^{-4} mbar is reached, we wait for one hour before closing the stop valve of the container.

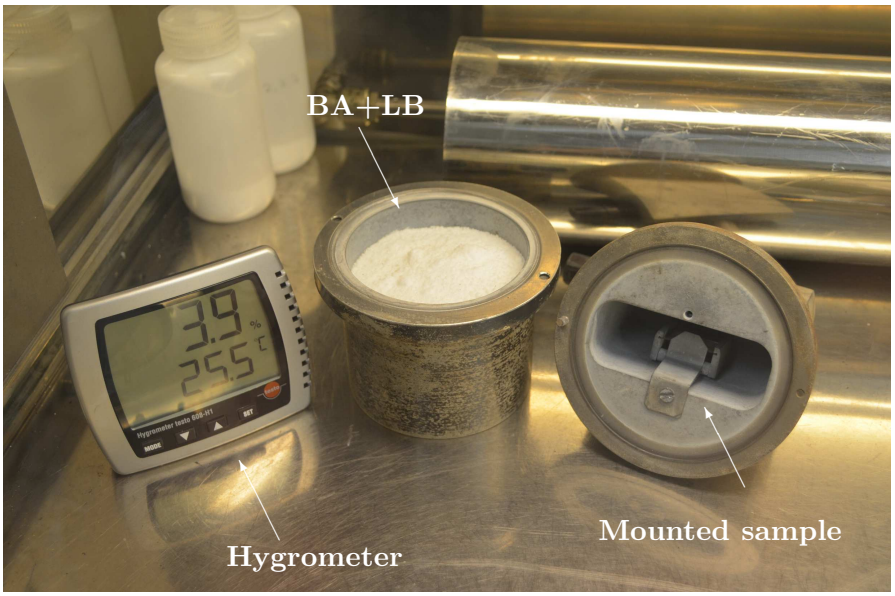

FIGURE 3.4: Assembling the container with the sample in a glove box for further proton exchange procedure. Air humidity is always controlled by hygrometer.

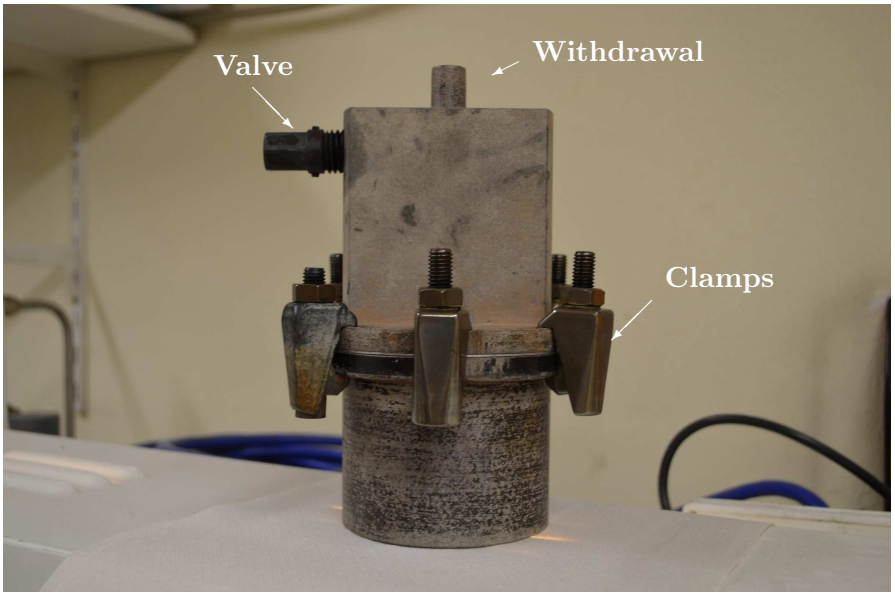

FIGURE 3.5: Assembled container ready for the proton exchange procedure. Two parts of the container are fixed by the stainless steel clamps. The valve is used to open and close the air withdrawal while pumping the container.

FIGURE 3.6: Creating vacuum inside the container. The container is placed into a heating bath to favor the powder drying.

5. Preliminary heating of the container

   Once closed, the container is placed in a furnace heated up at the exchange temperature. We wait 30 minutes to allow the powder to melt and all the system to reach the temperature balance.

6. Proton exchange

   The container is then turned upside down in the furnace to immerse the sample into the melt and the exchange starts to take place.

At the end of the proton exchange time the container is taken out of the furnace and rotated to the initial position. Thus the acid flows down and the sample, which is fixed, remains in the upper part of the container, out of the melt. The cooling is carried out at ambient temperature until it is possible to open the container and to release the samples.

All the samples fabricated in this work were made following this protocol. A strict observance of the fabrication protocol is necessary as the reproducibility of the fabrication technique is a quality to be verified.

3.3 Optical characterization of the planar HISoPE waveguides

3.3.1 Index profile

The m-lines technique is widely used to characterize planar waveguides on $LiNbO_3$ crystal. This technique permits to measure the effective indices N_{eff} of the optical modes of the waveguides. Then, using the values of the measured N_{eff}, one can calculate the index profile of the fabricated waveguides. Both the m-lines technique and the method of the index profile calculation are described in details in Appendix A.

Note that we use a two prisms coupling set-up for our m-lines characterizations. This configuration allows monitoring the propagation of the light in the waveguide as well, which gives qualitative indication about the optical quality of the waveguide.

Here, I will study a deep HISoPE waveguide. A 2.8 cm long sample was fabricated at $T = 300°C$ during 48 hours. The concentration of LB is $\rho_{LB} = 2.7\%$. The planar waveguide fabricated in these conditions has 5 optical modes at $\lambda = 633\,nm$. The calculated index profile for this sample waveguide is given in figure 3.7.

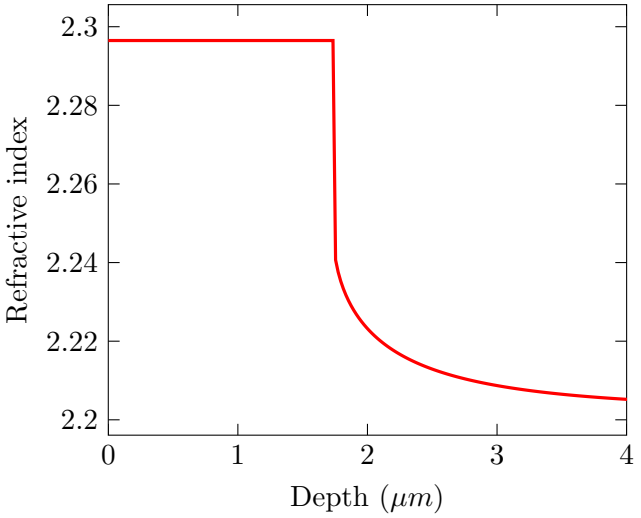

FIGURE 3.7: Index profile of planar HISoPE waveguide fabricated with $\rho_{LB} = 2.7\%$ at $T = 300°C$ during 48 hours.

The comparison of the m-lines of the 5 different modes in the sample is given in figure 3.8. Every mode was excited by adjusting the incident TE polarized laser beam. And then the light propagation in the waveguide was characterized. A photo of the propagation of the light in the waveguide sample was taken for each excited mode as well.

At the output, the m-line corresponding to excited mode consists of a luminous thin line with a much brighter spot in the center. This shape of the line corresponds to

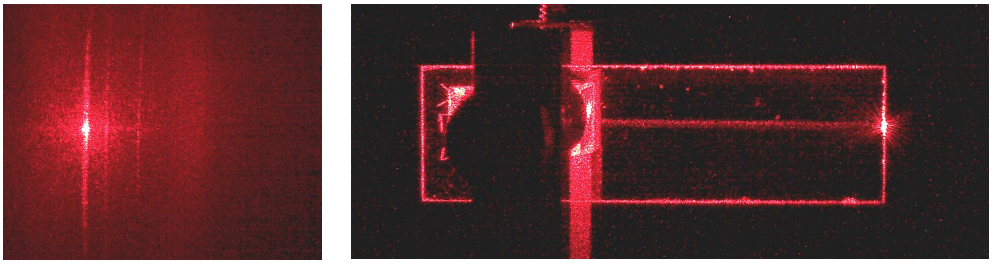

(a) TE0 mode ($N_{eff} = 2.2901$)

(b) Propagation trace of TE0 mode

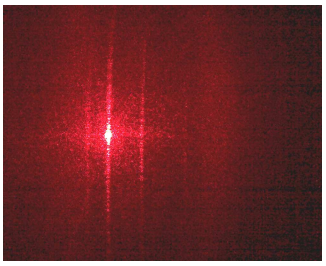

(c) TE1 mode ($N_{eff} = 2.2723$)

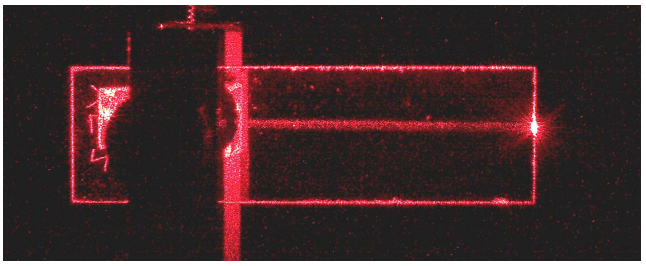

(d) Propagation trace of TE1 mode

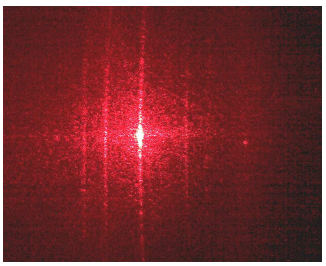

(e) TE2 mode ($N_{eff} = 2.2439$)

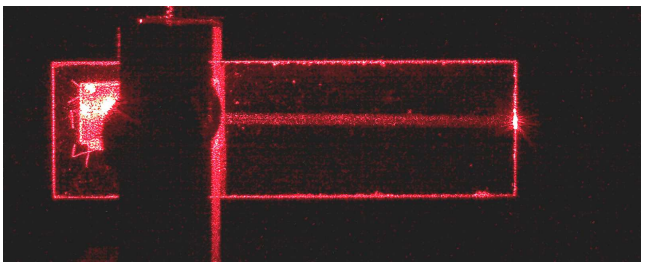

(f) Propagation trace of TE2 mode

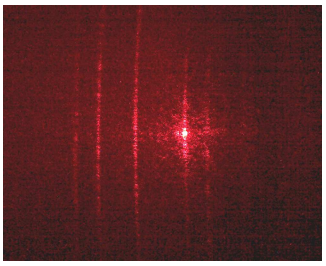

(g) TE3 mode ($N_{eff} = 2.2118$)

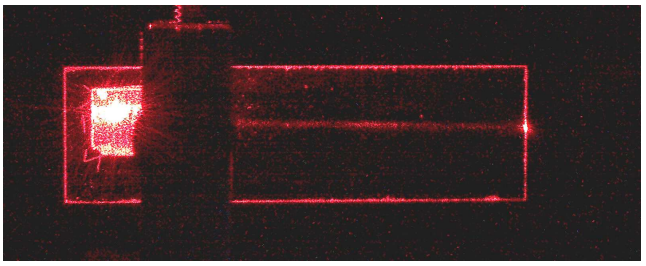

(h) Propagation trace of TE3 mode

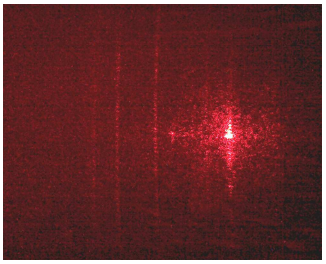

(i) TE4 mode ($N_{eff} = 2.2048$)

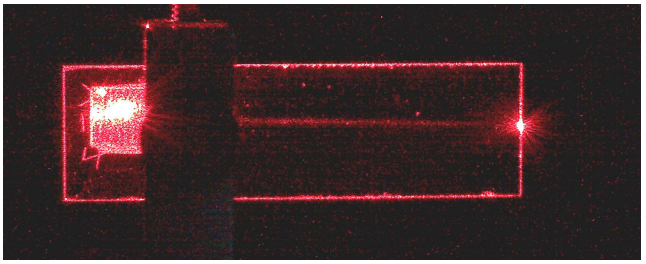

(j) Propagation trace of TE4 mode

FIGURE 3.8: M-lines characterization of HISoPE planar waveguide realized on X-cut $LiNbO_3$. A 10 mW He-Ne laser ($\lambda = 633$ nm) was used for characterization of the 2.8 cm long sample, which was fabricated at $T = 300°C$ during 48 hours at a temperature 300°C.

a good quality waveguide. But the propagation losses in the waveguide are not zero. That is why one can see the trace of the light along the direction of the propagation in the waveguide (figure 3.8). The intensity variation of this trace can give an idea of the value of the losses. In our sample the attenuation of the trace is hardly seen along the propagation length, which indicates that in this planar waveguide there are no big problems due to light scattering and we can conclude a good optical quality of the HISoPE waveguides.

3.3.2 Reproducibility

To evaluate the reproducibility, let us compare HISoPE waveguides, which were fabricated with the same fabrication conditions but at different dates. We carried out this study on planar waveguides as they are more suitable for rapid and systematic optical characterizations. The m-line measurement technique allows to calculate the maximum index change δn_e as well as the depth of the waveguide (for more details see Appendix A.2). Studying these two optical parameters of the waveguide is enough to make a conclusion about the reproducibility of the fabrication procedure.

In table 3.1 a series of six HISoPE samples is collected. All the samples were plunged in a melt with $\rho_{LB} = 2.7\%$ and heated up to a temperature of 300°C during 24 hours.

The values of δn_e as well as the waveguides depths were calculated. There is a variation in depth and in δn_e, though all the fabrication steps were strictly observed. The value of δn_e ranges from 0.091 to 0.095. The depth varies also between 0.7 and 1 μm for the studied samples (table 3.1).

The samples represented in the table have three modes at $\lambda = 633\,\text{nm}$. Such a limited number of modes does not allow to calculate δn_e and the depth with a great precision. Therefore, it is better to compare the measured effective index N_{eff} of the fundamental modes, which are the most sensible to the maximal index change in the waveguide and its dimensions. The variation of the index is around $4 \cdot 10^{-3}$.

Note that with the SPE technique the N_{eff} of the TE00 mode can be controlled with a precision of $4 \cdot 10^{-4}$.[30,123] But compared to SPE, HISoPE waveguides show an index change δn_e three times higher.

The variation of the effective index of the fundamental mode of $4 \cdot 10^{-3}$ can be considered to be a rather good value. One can notice from table 3.1 that the effective indices of the mode TE00 are practically the same for samples fabricated within two days (samples #5 and #6). This indicates that the fabrication procedure is extremely stable in a short period of time.

TABLE 3.1: Effective indices and calculated profile parameters of planar waveguides fabricated on X-cut $LiNbO_3$ at different times. Fabrication conditions are the same for all samples ($\rho_{LB} = 2.7\%$, $T = 300°C$, $t = 24$ hours).

#	Sample	N_{TE00}	δn_e	Depth (μm)	Date of fabrication
1	XA10	2.2775	0.095	0.9	09/09/2010
2	XC9	2.2792	0.093	1.0	01/12/2010
3	XC6	2.2771	0.093	0.9	13/12/2010
4	W2.5	2.2766	0.092	0.7	02/01/2011
5	XE6	2.2723	0.091	0.8	20/09/2011
6	XE1	2.2721	0.091	0.8	22/09/2011

The temperature of the melt and the duration of the exchange are controlled with a high enough accuracy to exclude their influence on the reproducibility. However, it is difficult to totally control the influence of the humidity of the proton exchange, though most of the fabrication steps are organized to minimize this effect. One of the reasons is that only a part of the fabrication cycle is carried out in the controlled atmosphere in the glove box. Therefore, a slight deviation of the waveguide parameters in the samples fabricated in different months or even seasons can be observed due to different climatic conditions and, consequently, due to different atmospheric humidity.

Nevertheless, HISoPE technique allows to fabricate planar waveguides with a precision of $\pm 0.1\,\mu$m in depth and with $\delta n_e = 0.093 \pm 0.002$, using a LB concentration $\rho_{LB} = 2.7\%$ and a temperature $T = 300°C$. This is a much better reproducibility than that obtained with the VPE technique. Besides, the difference between waveguides fabricated within the same week is not measurable. Thus one can make a test waveguide, measure its characteristics and then adjust the duration of the exchange to fabricate a sample with a desired index profile.

Finally we can conclude that HISoPE is a well reproducible technique and now we will discuss a more detailed study of the optical modes propagation in planar HISoPE waveguides.

3.3.3 Hybrid modes

The problem of hybrid modes is very specific to X-cut waveguides. As we have mentioned in section 2.4, the exchanged layer at the surface of X-cut $LiNbO_3$ substrate becomes biaxial due to the deformations induced by the proton exchange process. The optical axes of the biaxial layer are no longer linked to the crystallographic axes and are therefore free to rotate with respect to the substrate axes. A consequence of this rotation is that the two polarizations TE and TM are no longer independent, i.e. the modes propagating in the waveguide have both ordinary and and extraordinary components.

Thus if the effective index of the propagating mode is situated between the ordinary and the extraordinary indices of the substrate, $n_o \geq N_{eff} \geq n_e$, the ordinary part of the light will radiate into the substrate. This results in propagation losses and a special far field and m-lines spectra. An example is shown in figure 3.9. A He-Ne laser with wavelength $\lambda = 633\,\text{nm}$ was used for measurements. At this wavelength the characterized waveguide sample has three propagating modes. The extraordinary components of the modes are observed as three bright lines on the right hand side of the image.

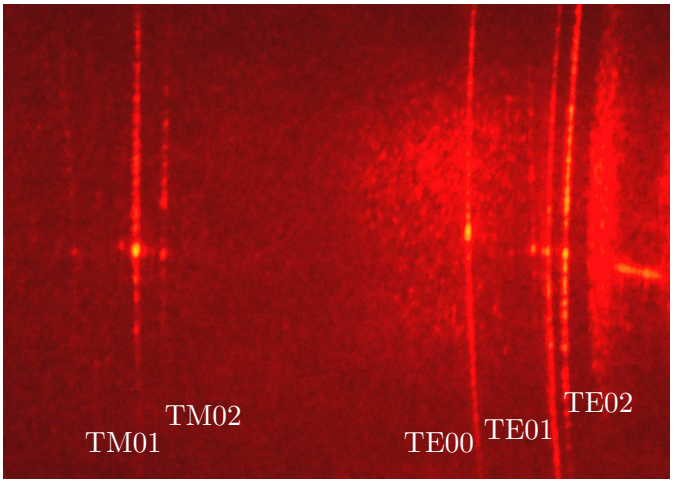

(a) M-lines corresponding to TE and TM modes

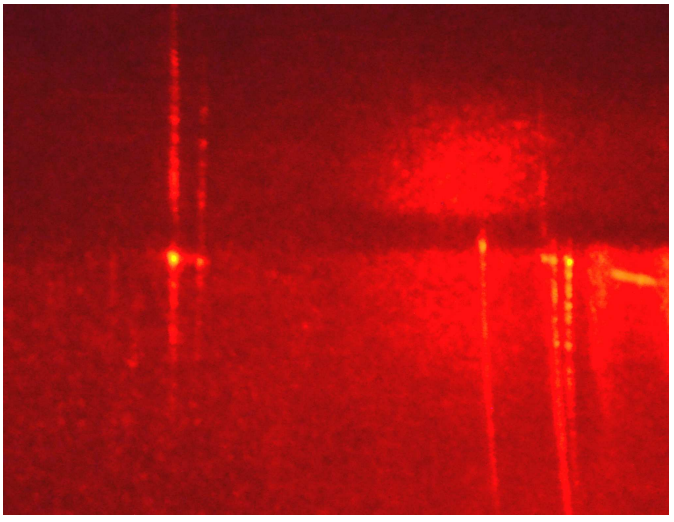

(b) A polarizing card was placed in front of the screen to illustrate the different polarization of the m-lines

FIGURE 3.9: Observation of the m-lies of HISoPE X-cut planar waveguide fabricated in 2.7% melt at 300°C during 24 hours. The waveguide has three propagating modes at $\lambda = 633\text{nm}$.

In addition to these three m-lines, one can see two orthogonally polarized lines on the left side. Only two modes are observed, which means that the third mode has an effective index greater than the ordinary index of the substrate, i.e. $N_{eff} > n_o > n_e$. Therefore both components of this mode are guided.

An interesting characterization should be m-lines at 1.5 μm wavelength for monomode waveguide. Indeed, if the effective index of the fundamental mode is above the ordinary index of the substrate at this wavelength, the hybrid nature of the mode is no longer a problem. Unfortunately, with the equipment at our disposition we had a problem to visualize m-lines at this wavelength.

The conclusion of the m-lines characterization is that one should remember the mechanism of propagation losses due to hybrid modes when designing and/or fabricating waveguide on X-cut $LiNbO_3$. In channel waveguides the deformations will not be the same as in planar waveguides. Thus it is difficult to say at this stage what propagation properties we can expect in the channel waveguides.

3.3.4 Surface SHG characterization

The nice linear optical properties of the obtained proton exchanged waveguides with high δn_e is not a surprise. For example PE waveguides with low losses can be fabricated, but they have very degraded $\chi^{(2)}$ properties. But our goal is to fabricate highly confining waveguides in $LiNbO_3$, with preserved properties of the bulk crystal such as nonlinear and electro-optical coefficients. So let us focus on $\chi^{(2)}$ in HISoPE waveguides.

Surface scanning SHG technique were used to probe the modification of $\chi^{(2)}$ in the proton exchanged waveguides. It is a rather simple experimental technique, but it allows to compare directly $\chi^{(2)}$ in the waveguide and in the substrate.[73] The experimental set-up as well as the principle of the technique are described in details in Appendix C.

Briefly, the principle of the method consists in observing and comparing the reflected SHG signal from the different areas of the $LiNbO_3$ crystal. A laser beam, powerful enough to generate the second harmonic, is focused on the polished facet. The reflected SHG and fundamental signals are measured at the same time while the sample is being moved through the beam. In particular, we used the configuration when the laser beam is focused on the polished end facet of planar waveguide sample (see figure 3.10). The waveguide under test is moved in the vertical direction, from the surface to the substrate (figure 3.10), by changing the position of the sample with the help of a piezo-electric translator.

The amplitude of the translation is high enough to start in the air above the sample, then scan through the waveguide where the $\chi^{(2)}$ can be affected by the proton exchange, and finally reach the unmodified substrate where the nonlinear coefficient has the original bulk value, which is used as a reference. An example of SHG surface probing of an X-cut HISoPE waveguide is given in figure 3.11. When the beam is over the sample,

the intensity of the reflected fundamental is zero. Then, the sample is moved up using the piezo-electric stage. When the beam starts to hit the surface, the fundamental curve rises. The index profile is plotted in the same figure to have an idea about the depth of the waveguide.

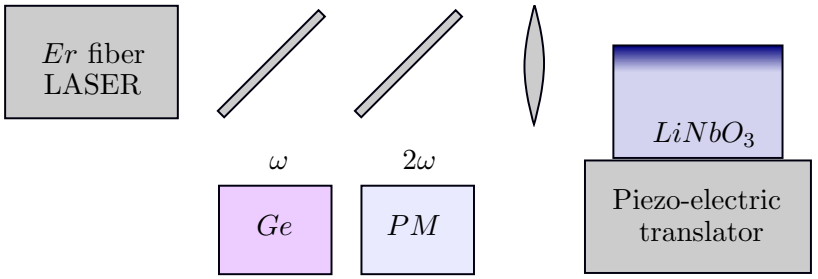

FIGURE 3.10: Schematics of reflection SHG measurement set-up. *Er* fiber laser wavelength is 1550 nm.

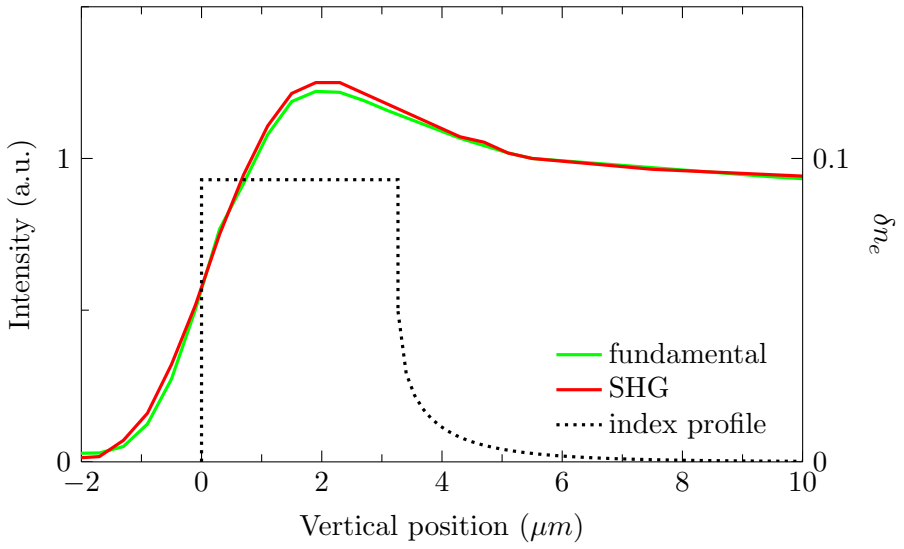

FIGURE 3.11: Surface SHG profiling of HISoPE waveguide and the corresponding index profile for a wavelength λ=0.633 μm. The sample was fabricated in 2.5% melt of BA and LB at 300°C during 3 days.

The SHG signal has the same shape as the fundamental. The important thing here is that SHG intensity is not reduced in the waveguiding layer. The intensity curves in figure 3.11 coincide perfectly with the waveguide depth as well as in the bulk $LiNbO_3$. Therefore, surface SHG measurements do not point out any reduction of the nonlinear coefficient $\chi^{(2)}$ as far as we can judge from the resulting reflected intensities of the fundamental laser beam and SH.

3.4 Channel HISoPE waveguide fabrication

Once the HISoPE technique was validated for planar waveguides, channel waveguides became the next target.

The fabrication of channel waveguides demands a photolithography technique described in section 1.7. The optical mask was designed and fabricated on purpose for HISoPE waveguides. The design of the mask is given on the figure 3.12.

The pattern includes twelve small samples, which have 2.8 cm length suitable for the sample holder. Small crosses on the mask are useful for cutting the wafer before or after the proton exchange. Every sample consists of 9 groups of waveguides. Each group consist of 6 waveguides of three different widths: 1 μm, 1.5 μm and 2 μm (see figure 3.12). Further we will use roman numerals to indicate a group and small latin letters to indicate waveguides within the group.

The widths of the mask openings are almost the limit of standard UV photolithography, which is around 0.5 μm. The photolithography procedure was totally carried out by Sarah Benchabane from FEMTO-ST in Besançon, using MIMENTO platform. The layer of SiO_2 was deposited either at FEMTO-ST or at CILAS in Marseille.

The lift-off procedure is made after the deposition of SiO_2 layer upon the pattern of the photoresist. For this purpose, the wafer is immersed in acetone bath and placed in ultrasonic cleaner. A duration of 15 minutes is usually sufficient to remove the photoresist with SiO_2 above. Unfortunately, acetone himself leaves its own residues. For this reason in a second step the wafer is dipped in ethanol bath for one minute. Finally the wafer is rinsed in distilled water and blown with dry air. There are no pauses between cleaning steps: the wafer is removed and placed into the following bath rapidly because the residues that are left on the dry surface are very difficult to remove.

Once the lift-off is done, the wafer is ready for the proton exchange. At this stage, the wafer can be cut if only small samples are needed for the study. The thickness of SiO_2 layer is about 250 nm thus any scratch can damage the mask. Consequently, the treatment of the sample demands a great care.

The proton exchange procedure is always the same as the one described earlier in section 3.2.1. The SiO_2 mask allows proton exchange only through the openings of 1, 1.5 and 2 μm width. However, the opposite side of the sample is not protected by any layer and a planar waveveguide is fabricated at the same time.

It is very useful, as the depth of the channel waveguides can be evaluated indirectly by measuring the N_{eff} of the planar waveguide using a simple prism coupling technique.

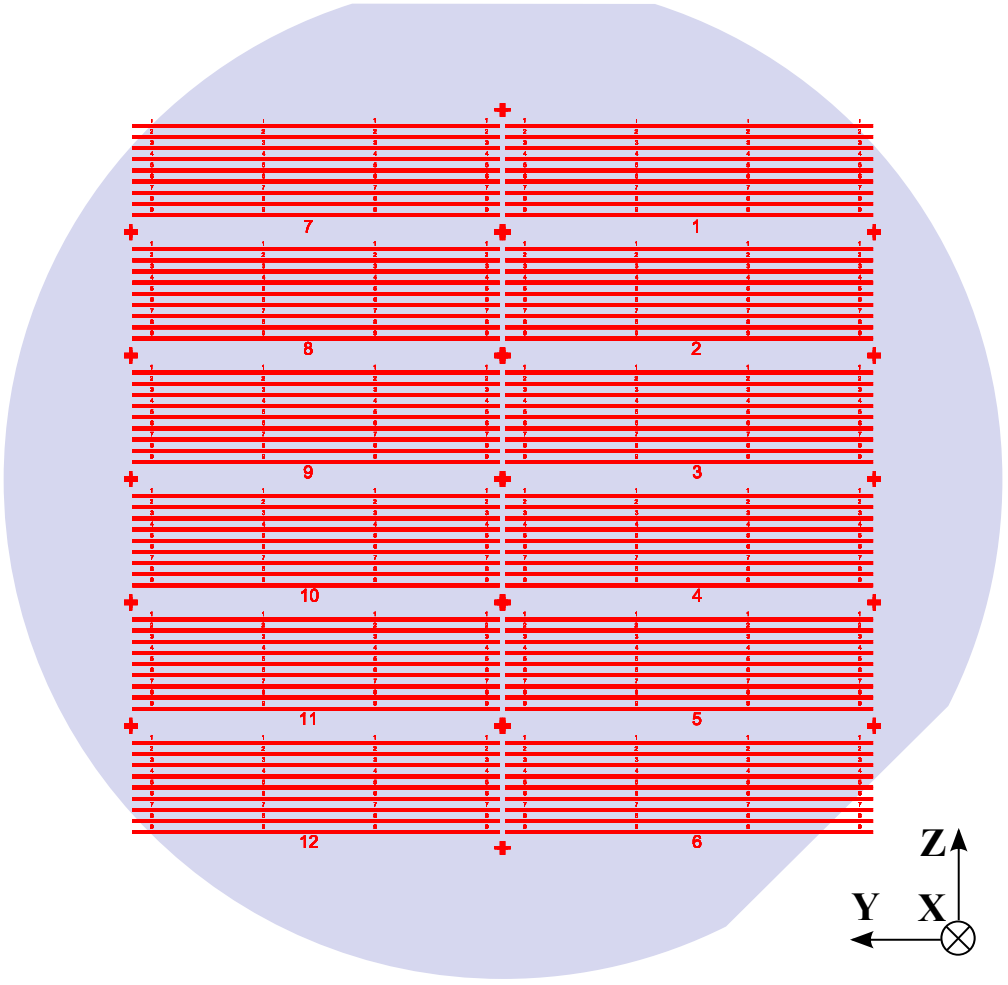

(a)

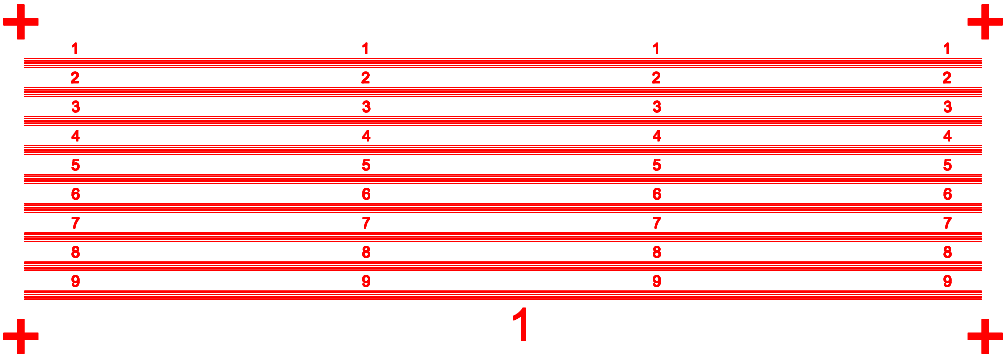

(b)

FIGURE 3.12: Design of the mask that was used for HISoPE channel waveguide fabrication: (a) - organization of the samples on the X-xut $LiNbO_3$ crystal surface; (b) - design of a separate sample with waveguides organized in 9 groups with 6 waveguides in each.

The variation of the refractive index, $\delta n_e \approx 0.9$, in HISoPE waveguides allows to observe the channel waveguides with an optical microscope (see figure 3.13). Therefore all the possible defects of the fabrication procedure related to the mask imperfections can be verified. The sample can also be placed vertically and illuminated from below. Some light is coupled into the waveguides which can be observed with the microscope on the other end facet of the sample (figure 3.13(b)). This test do not require a lot of efforts, however one can rapidly identify damaged waveguides in which light does not propagateat all.

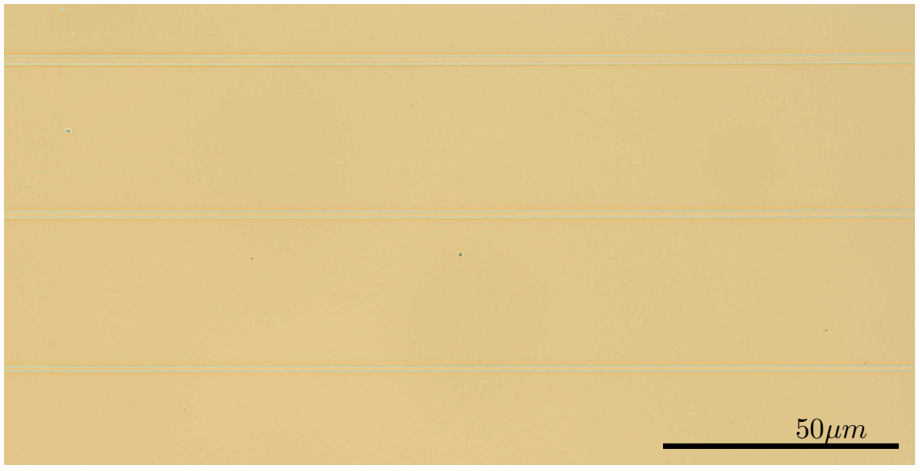

(a) view from above. The sample is observed in bright field and no polarizing filter is used. The three HISoPE waveguides correspond to the waveguides fabricated by the proton exchange through 1, 1.5 and 1.5 μm mask openings. The mask of SiO_2 had been removed before the photo was taken.

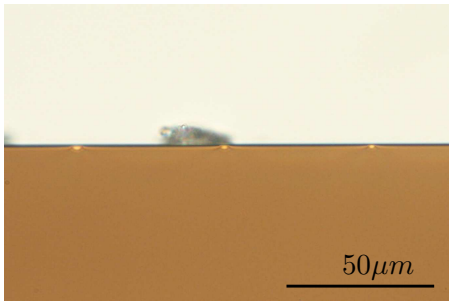

(b) View from end facet. TE polarized light is used for illumination. The waveguides can be recognized by the emerging guided light. Dust particles are visible on the surface, but this does not correspond to any defects of the surface.

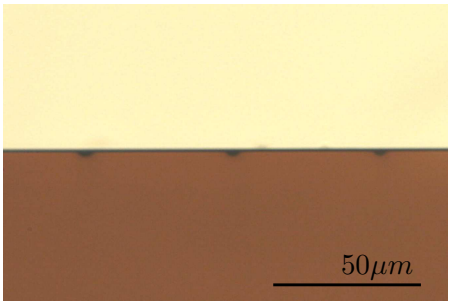

(c) View from end facet. TM polarized light is used for illumination. As the proton exchanged waveguides on X-cut surface do not support TM polarization, the exchanged channels are darker than the substrate.

FIGURE 3.13: Channel HISoPE waveguides observed using an optical microscope. Observing the sample in the bright field configuration allows to find quickly the waveguides which are damaged. The channel waveguides in these figures were fabricated in 2.7% melt at 300°C during 48 hours.

3.5 Optical characterization of the channel HiSoPE waveguides

3.5.1 M-lines

Having the same fabrication parameters does not imply that the planar waveguide fabricated on the backside of the substrate and the channel waveguides have the same refractive index change and depth. The maximal index change δn_e in the channel waveguides is usually smaller than that of planar waveguides. Notably the channel waveguides index decreases with their diameter.[30]

In order to measure the index change of the channel waveguides, the prism coupling technique can be used to measure the effective indices (Appendix A). As the prisms touch directly the surface of the sample, this technique is potentially dangerous for characterizing the channel waveguides because any mechanical scratch can damage the waveguide. Thus the characterization demands a lot of care. However, knowing the effective indexes of the channel waveguides, one can calculate the index change δn_e and evaluate the width of the waveguides (see for details Appendix A.2).

As it was mentioned in the previous section 3.4, every sample with channel waveguides has a planar waveguide on the opposite side of it. Let us compare these waveguides with the channel ones. In table 3.2 we present the parameters calculated from effective indices measured by the prism coupling method. The sample was fabricated in a melt of BA and LB with the concentration $\rho_{LB} = 2.7\%$ at the temperature of 300°C during 36 hours. The depth of the planar waveguide is 1.3 μm and $\delta n_e = 0.094$. The reconstructed profile of this waveguide is given in figure 3.14.

TABLE 3.2: Calculated index change and the dimensions of the channel HISoPE waveguides. The sample was fabricated in BA+BL melt with $\rho_{LB} = 2.7\%$ at the temperature of 300°C during 36 hours.

opening (μm)	waveguide (μm)	enlargement (μm)	depth (μm)	δn_e
1	1.8	0.8	0.9	0.093
1.5	2.2	0.7	1.0	0.093
2	2.5	0.5	1.1	0.093
planar w-g			1.3	0.094

The channel waveguides are not as deep as the planar one. The depths vary from 0.9 μm for the most narrow waveguides to 1.1 μm for the widest ones. The mask openings reduce the proton exchange rate due to small area of $LiNbO_3$ exposed to the source of protons. Therefore the planar waveguides are deeper than the channel waveguides fabricated in the same conditions.

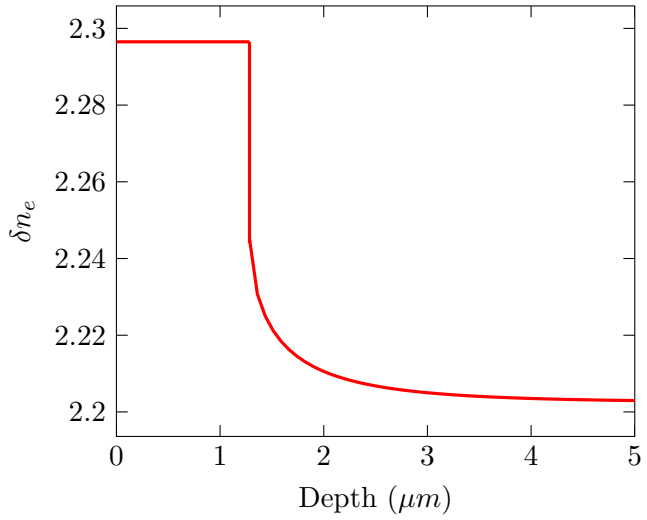

FIGURE 3.14: Index profile of planar HISoPE waveguide of the sample W29.

In addition the lateral diffusion slows down the formation of the waveguide in depth. Comparing the widths of the mask openings (first column of table 3.2) with the widths of the obtained channel waveguides (second column), one can conclude that the enlargement of the channel HISoPE waveguides is not negligible (third column). The enlargement due to the lateral diffusion of the protons is more significant for waveguides with smaller width.

Surprisingly, the value of δn_e in the obtained channel waveguides is practically unchanged compared to the planar waveguides. Consequently, the confinement ability is not reduced and this stands as a positive sign.

3.5.2 Propagation losses

Propagation losses in the channel waveguides were measured using the Fabry-Perot cavity method (see Appendix B for more details). All the samples for this characterization were fabricated with the melt concentration $\rho_{LB} = 2.7\%$ at 300°C during 48 hours.

A first set of the samples was fabricated with a SiO_2 mask deposited at FEMTO-ST using evaporation method of deposition. They showed average losses of $4 \pm 0.3\,\mathrm{dB/cm}$ at $\lambda = 1.55\,\mu\mathrm{m}$. Such a value is too high to be acceptable for device fabrication.

One of the possible mechanisms of the propagation losses could be the defects of the SiO_2 mask that leads to imperfections of the waveguides and therefore to scattering losses. As the samples were observed using an optical microscope before the proton exchange, we exclude this source of losses.

A next series of the samples was fabricated with a SiO_2 mask deposited by Cilas using ion beam assisted deposition method. We observed better value of propagation losses of 1.75 ± 0.2 dB/cm for HISoPE channel waveguides fabricated on X-cut $LiNbO_3$. As the fabrication conditions were the same for all the samples except the deposition procedure of the SiO_2 mask, this significant improving of the propagation losses is referred to the quality or different physical properties of the SiO_2 layer. But the mechanism of influence of SiO_2 mask on the final properties of the proton exchanged waveguides remains unclear.

However, there is another mechanism of losses in the HISoPE waveguides fabricated on $LiNbO_3$, which is not related to the fabrication defects. As discussed for planar waveguides the crystalline deformations induced by the proton exchange can favor TE-TM coupling. The hybrid modes can explain the high values of losses observed in the channel waveguides. This will be discussed in the next paragraph.

3.5.3 Hybrid modes in channel waveguides

In order to verify the hybrid nature of the modes, TE polarized light was injected into the channel HISoPE waveguide by microscope objective. The end faces of the sample were polished in advance. We used a visible 5 mW He-Ne laser radiating a wavelength of 633 nm. Though, the characterized waveguides were multimode at this wavelength, the advantage was that there was no need of a special IR camera to observe the light scattering from the waveguide. A paper screen with a polarizing card were placed behind the end face of the waveguide to observe the light that exits the sample (figure 3.15).

The ordinary part of the hybrid modes radiates into the substrate at certain angles corresponding to the effective indices of the propagating modes. On the paper screen the hybrid modes will be represented by a curved bright lines as in the figure 3.16. A part of the radiating light is reflected from the bottom of the sample, that is why there is a mirror reflection of the lines in the upper part of the image.

The intensity of these lines depends on the TE-TM coupling in the waveguide. As the waveguide is multimode at 633 nm, one can observe the concentric lines corresponding to the different propagating modes when the polarizer is oriented to select the TM polarization. The shape of the lines is explained by the radial shape of the channel waveguide.

One can easily calculate the effective indices of the propagating modes by measuring the corresponding angles between the waveguide direction and the TM polarized rays.

Even with usual photo camera one can see that the intensity of TM polarized light is relatively weak compared to the intensity of propagating TE polarized light. Therefore, it is interesting to see the propagation of IR light in the waveguide as the final device (EO modulator) should work at the wavelength of 1.55 μm.

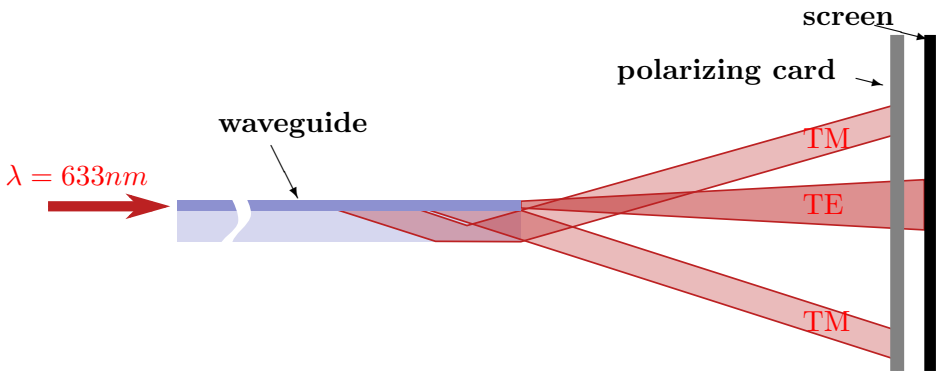

FIGURE 3.15: Schematics of the experimental set-up for observing hybrid modes.

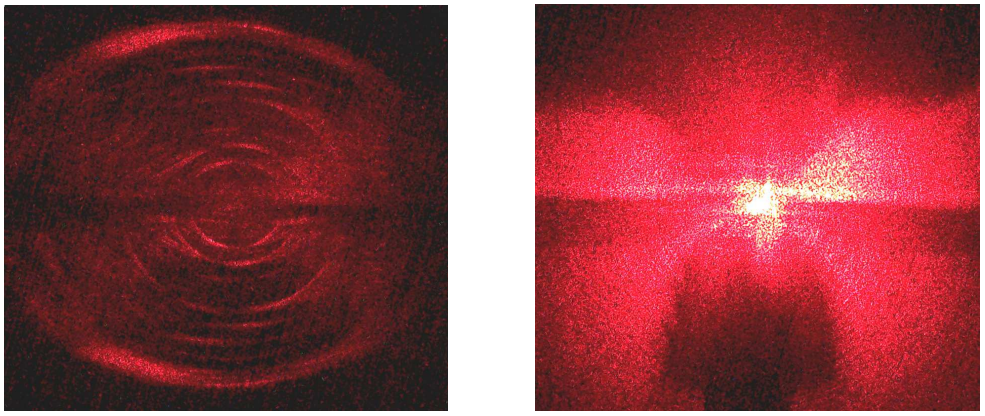

(a) TM polarization (b) TE polarization

FIGURE 3.16: The photos of the screen placed behind the X-cut HISoPE waveguide sample. The sample was placed horizontally.

The characterizations at IR wavelengths around 1.55 μm were carried out at Thales Research and Technology by Jérôme Bourderionnet.

A laser at $\lambda = 1.55\,\mu$m was coupled into the waveguide by a lensed optical fiber. On the other side of the sample, a microscope with an IR camera allowed a direct imaging of the optical mode that exits from the end of the waveguide. An example of the waveguide end-facet image is presented in figure 3.17.

As one can see from the image 3.17(b), the TM component is not observed with this set-up. However they were noticed using an IR sensing card. The experimental set-up was modified because the numerical aperture and working distances of microscope objectives did not allow to visualize the TM component of light. The schematics of the new experimental set-up is presented in figure 3.18. A screen (paper sheet) with a

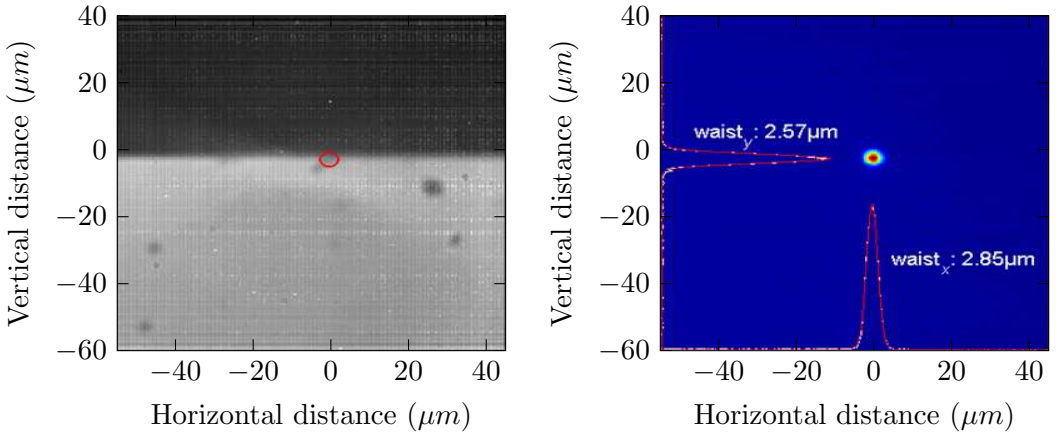

(a) End-face of the sample

(b) Light exits the waveguide

FIGURE 3.17: Near field imaging of the propagating mode at $\lambda = 1.55\,\mu$m in HISoPE channel waveguide. The light injected into the waveguide fabricated through $2\,\mu$m mask opening. The width and the depth are $2.5\,\mu$m and $1.1\,\mu$m respectively. The proton exchange was carried out in the BA melt with 2.7% of LB at a temperature of 300°C during 36 hours.

polarizer is placed between the sample and the IR camera. By changing the angle of the polarizer, it is possible to observe TE and TM polarizations separately.

A spot corresponding to the fundamental mode is observed (figure 3.19(a)) when the polarizer is set to transmit TE polarization. TM component radiates into the substrate. A part of the TM polarized light is reflected from the bottom side of the sample and thus two beams are observed on the screen at the same time (figure 3.19(a)). The asymmetry of the TM arcs is not clearly understood and was not observed at 633 nm as can be seen in figure 3.16.

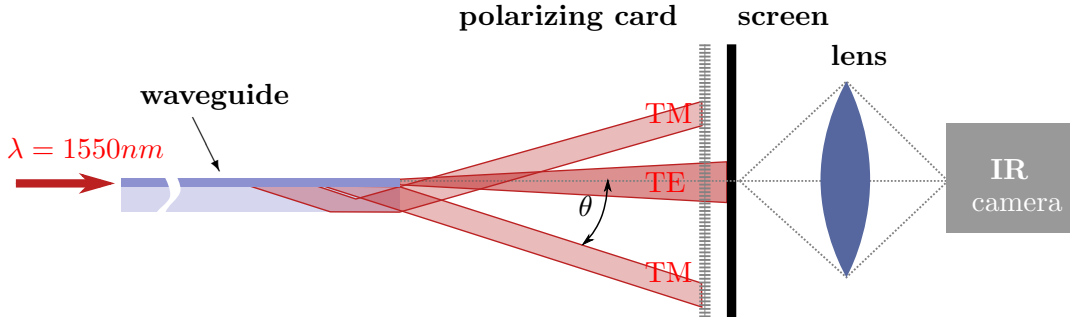

FIGURE 3.18: Schematic representation of the experimental set-up used to observe both the propagating and the hybrid modes.

The angle between TM polarized beam and the direction of propagation is related to N_{eff} of the propagating hybrid mode by the equation:

$$N_{eff} = \sqrt{n_o^2 - \sin^2\theta}, \tag{3.1}$$

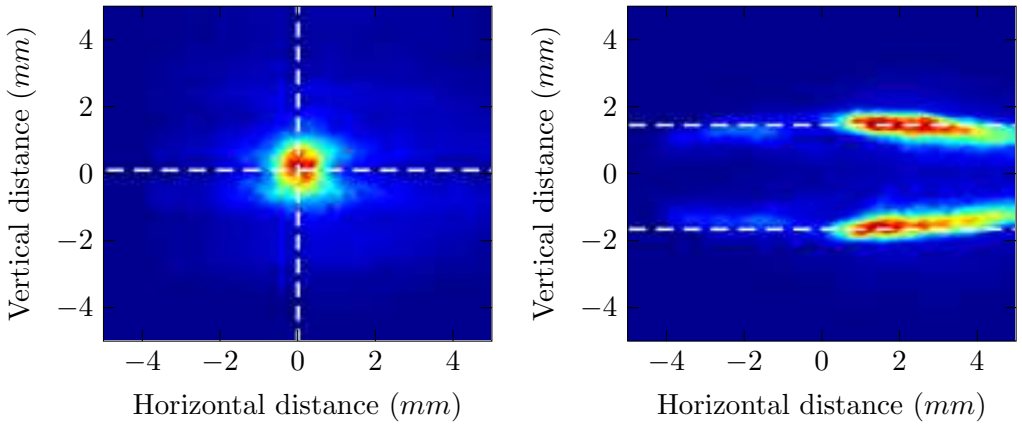

(a) TE polarization.

(b) TM polarization.

FIGURE 3.19: TE and TM components emitting from HISoPE channel waveguide. A distance between the end face of the waveguide and the screen is 3.5 mm.

where n_o is the ordinary refractive index of the substrate. The angle θ is equal to 19.5°. It can be easily calculated assuming the distance between the waveguide and the screen (3.5 mm) and the distance between the TM polarized arc and the center of the TE polarized spot (3.1 mm).

The ordinary index in $LiNbO_3$ substrate is 2.2112 for a wavelength $\lambda = 1.55\,\mu$m. Therefore one can easily calculate $N_{eff} = 2.186$. This value of N_{eff} is smaller than n_o in the substrate, which explain the coupling with radiating mode. This experiment confirmed that a part of the propagation losses is due to the hybrid nature of the propagating modes. Despite this intrinsic problem we were able to realize waveguides with losses ≤ 2 dB/cm and decided to use them to verify the possibility of combining the HISoPE waveguides with photonic crystals.

3.5.4 Transmission spectra of nanostructured micro waveguides

The photonic structures on the HISoPE waveguides were etched by FIB milling, and the transmission spectra of these nanostructured waveguides were studied. This part of the work was totally carried out by FEMTO-ST in Besançon. In this paragraph a few transmission spectra will be presented just to illustrate the problematic and the current state of the art of the project.

The transmission curves for the wavelengths ranging between 600 nm and 1800 nm were measured using a supercontinium white light source. The light was coupled in and out from the waveguides using optical fibers.

Let us compare the transmission of the structured waveguides. Three configurations were studied and those are illustrated in figures 3.20, 3.21 and 3.22, respectively. The first and the second are photonic crystals with a triangular and a square lattice, respectively. The last sample presents a triangular photonic crystal with an introduced defect: one row of air holes along the direction of propagation was removed. In the figures, the green curves correspond to the transmission of the waveguide without any photonic structures. The red curves were obtained for the structured waveguides.

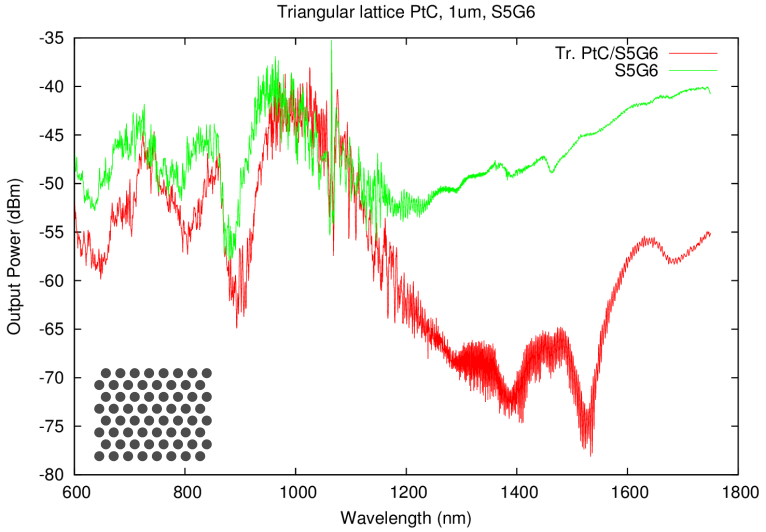

FIGURE 3.20: Transmission curve of the HISoPE waveguide with triangular lattice photonic crystal. The waveguide width is 1 μm (width of the mask opening). The characterization was made by FEMTO-ST.

The waveguides are multimode in the visible range. For this reason the transmission spectra of the waveguide is very fluctuating in this region. Starting from 1200 nm the rapid fluctuations disappear (the waveguides become monomode) and a gradual augmentation of the signal with the wavelength can be observed.

The parameters of the photonic crystals, the period and the radius of the hole, were chosen in order to create an optical transmission gap around 1500 nm. Experimentally, we observed that the photonic crystals on the HISoPE waveguides modify the initial spectra by decreasing the level of the signal between 1200 and 1800 nm with the appearance of gaps around 1400 and 1520 nm. In addition, the transmission curves are very noisy in this range.

The overall attenuation of the signal after the nano-structuration of the waveguide can be explained by the imperfection of the air holes. The conical shape of the holes remains the main and unsolved problem for $LiNbO_3$. Certainly this adds important extra propagation losses.

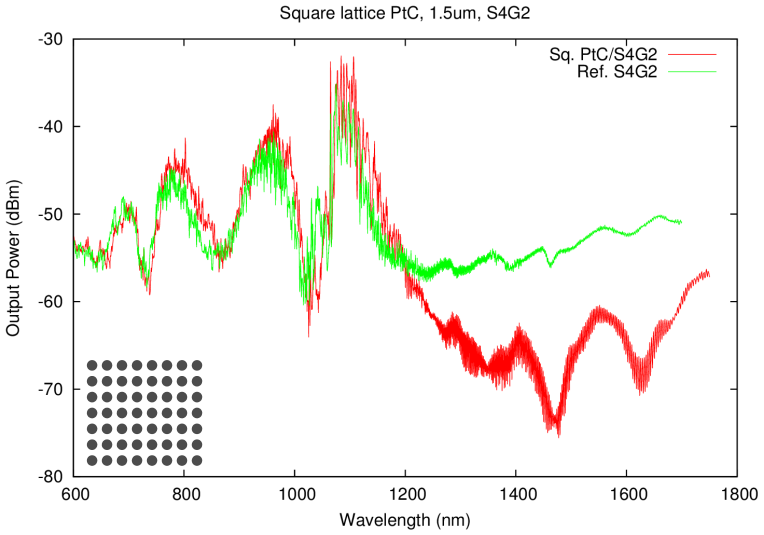

FIGURE 3.21: Transmission curve of the HISoPE waveguide with square lattice photonic crystal. The waveguide width is 1 μm (width of the mask opening). The characterization was made by FEMTO-ST.

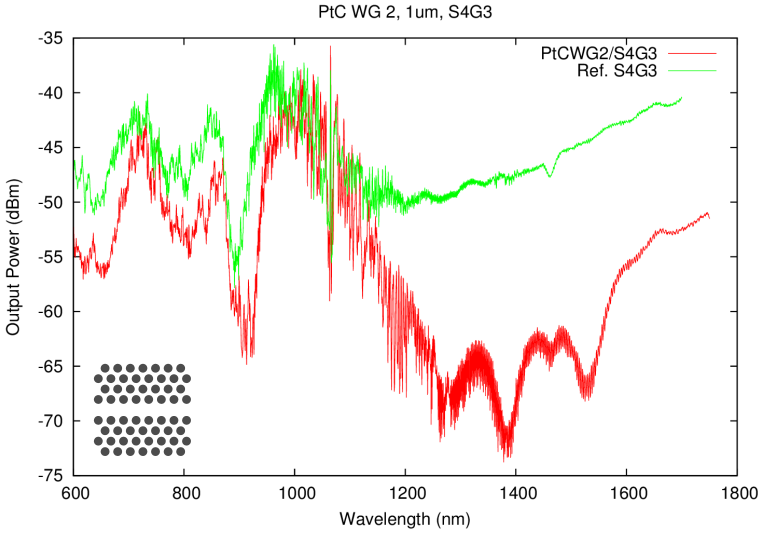

FIGURE 3.22: Transmission curve of the HISoPE waveguide with triangular lattice photonic crystal where one row of the hole was removed. The waveguide width is 1.5 μm (width of the mask opening). The characterization was made by FEMTO-ST.

However, the most important characteristic is that the spectra are very similar for all the photonic crystal regardless of the hole organization or the presence of the defect (one row missing). Therefore, the observed signal gaps between 1200 and 1800 nm do not correspond to a signature of the photonic crystal.

Taking into account the difficulty of hole etching in $LiNbO_3$, it is possible that the overall losses on the photonic structure hide the shape of the transmission curve that should correspond to the photonic crystal.

3.6 Discussion and Perspectives

The first characterization of planar HISoPE waveguides on X-cut $LiNbO_3$ showed that the fabrication technique is reliable and well reproducible. The light scattering is weak for planar HISoPE waveguides, which indicates low losses. On the other hand, the propagating modes are hybrid modes, which can have very undesired consequences. Concerning the nonlinearities, the surface SHG probing did not reveal any reducing of $\chi^{(2)}$. Thus HISoPE waveguides are very different from PE and SPE ones as they propose tight confinement with preserved nonlinearities.

The channel HISoPE waveguides showed no reduction in the index change, and consequently the optical confinement is high for these waveguides. Unfortunately the propagation losses are rather high. The best measured values were around 1.75 dB/cm which can be explained by the hybrid nature of the propagating modes.

This first attempt to combine HISoPE waveguides with photonic crystals (PCs) can be considered as unsuccessful. The HISoPE waveguides were supposed to confine the optical mode to a depth smaller than the depth of the hole of the PC. But the spectral gap corresponding to the photonic structure were not observed even for PCs on HISoPE waveguides with $\delta n_e = 0.09$. Therefore the tight optical confinement of the HISoPE waveguide does not solve the problem.

The losses around 1.75 dB/cm due to the hybrid nature of the propagating modes are the main weak side of these waveguides. Just for comparison, the PE waveguides with similar optical confinement realized on X-cut crystal had the losses in the order of 30 dB/cm.[108] So here we have much better values. However they are not acceptable for device fabrication neither.

One of the proposed idea, aimed at solving the problem of light radiating into the substrate, was to realize a double exchange in the following way. Firstly, a deep waveguide should be fabricated with a not very high value of δn_e. Then a HISoPE waveguide can be fabricated on the same surface, but its depth should be smaller than the depth of the first waveguide. In this case the deep waveguide serves as a new modified substrate. It can be, for example, a deep SPE waveguide. As the proton exchange increases the extraordinary index and reduces slightly the ordinary one, this could be enough to get an effective index of the propagating mode in the HISoPE waveguide higher than the ordinary index of the modified substrate. In this case, the hybrid nature of the mode, no longer introduces extra propagation losses.

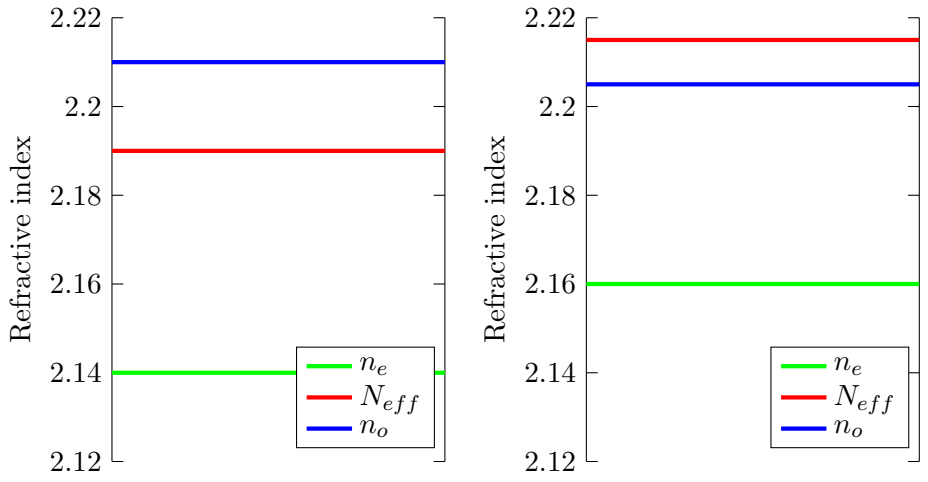

(a) HISoPE waveguide (b) SPE + HISoPE waveguide

FIGURE 3.23: The position of the effective index of the fundamental mode relative to ordinary and extraordinary indices of the substrate at $\lambda = 1.5\,\mu$m. The values were calculated for 1μm planar waveguide.

We fabricated a series of double exchanged samples using SPE as deep waveguide. Unfortunately the index change drops down very quickly with the depth. Therefore HISoPE waveguides of $1\,\mu$m depth do not 'see' the difference.

It is difficult to fabricate a much deeper SPE waveguide. The experiment should be repeated, but using an APE process, in order to modify a deep enough layer which can act as a quasi substrate. This will require a new study which I could not lead in the remaining time of my PhD work.

Chapter 4

Highly confining waveguides on Z-cut $LiNbO_3$

4.1 HISoPE technique applied to Z-cut $LiNbO_3$ wafers

Due to the anisotropy of $LiNbO_3$, the proton exchange process along the Z-axis is different from that along the X-axis. Waveguides on X-cut surface are usually deeper than waveguides on Z-cut surface fabricated in the same conditions.[30,108] The threshold concentration ρ_t shifts from 2.8% for X-cut to 2.7% for Z-cut $LiNbO_3$ at an exchange temperature of 300°C. As for X-cut waveguides, we chose for realizing highly confining waveguides on Z-cut $LiNbO_3$ to work with a concentration of LB high enough to preserve the nonlinear and electro-optical coefficients but lower than ρ_t to create also a high index change for the waveguides. Except the concentration, we used the same fabrication parameters and steps that were used for fabricating X-cut waveguides (see section 3.2.1).

4.1.1 High loss optical modes in HISoPE waveguides

Unexpectedly, working with LB concentrations close to ρ_t, even planar Z-cut optical waveguides suffer from high propagation losses. For a demonstration of the problem we will take three planar waveguide samples fabricated with different LB concentrations, in our case 2%, 2.3% and 2.4%, at the same temperature of 300°C during 17 hours. A more acidic proton source accelerates the proton exchange and, consequently, the waveguide formation. While the duration of the proton exchange is the same for the three samples, the one fabricated at $\rho_{LB} = 2\%$ is deeper and has eight propagating modes compared to five and six modes in the waveguides fabricated with 2.4% and 2.3% respectively. The measured N_{eff} for these samples are given in table 4.1.

TABLE 4.1: Measured effective indices (at $\lambda = 0.633\,\mu$m) measured for planar waveguides fabricated using different concentrations of LB: 2%, 2.3% and 2.4%.

Sample	ρ_{LB}	Temperature	Exchange duration	Modes	N_{eff}
Z1	2.0%	300°C	17 hours	TM_{00}	2.3051
				TM_{01}	2.2986
				TM_{02}	2.2892
				TM_{03}	2.2762
				TM_{04}	2.2600
				TM_{05}	2.2403
				TM_{06}	2.2185
				TM_{07}	2.2040
Z9	2.3%	300°C	17 hours	TM_{00}	2.2991
				TM_{01}	2.2867
				TM_{02}	2.2665
				TM_{03}	2.2402
				TM_{04}	2.2129
				TM_{05}	2.2039
Z7	2.4%	300°C	17 hours	TM_{00}	2.2951
				TM_{01}	2.2739
				TM_{02}	2.2417
				TM_{03}	2.2108
				TM_{04}	2.2033

Let us now examine the optical TM_{05} mode of the first sample, the TM_{03} mode of the second sample and the TM_{02} mode of the third sample which are given in the table. The values of N_{eff} of these modes are very similar, around 2.24 at $\lambda = 633\,$nm. Looking at the m-lines image of the sample fabricated at $\rho_{LB} = 2.4\%$ (figure 4.1(a)) we see that TM_{02} mode is very attenuated so that only a light spot is visible. Generally, a weak intensity of the m-lines can be caused either by the propagation losses or by an inefficient coupling between waveguide and the prism used in the m-lines experiment. Inefficient coupling between the waveguide and the prism results in attenuation of all the m-lines. But as one can see on figure 4.1(a), the TM_{02} mode is the only one to be weak while the neighbor m-lines of TM_{01} and TM_{03} are much brighter, though the coupling is not optimized for these particular modes. This indicates that the different optical modes in the waveguide of the sample have different propagation losses. Moreover, all the optical modes with N_{eff} between 2.23 and 2.27 for all the waveguides fabricated with $\rho_{LB} = 2.4\%$ suffer from high propagation losses while the other modes propagate well in the same waveguides. Thus, it is not an accidental effect and this concerns only the modes with effective indices confined in a range $2.27 > N_{eff} > 2.23$.

The m-line of the TM_{03} mode of the sample fabricated with $\rho_{LB} = 2.3\%$ (see figure

4.1(b)) is much brighter compared to the first sample. But still, the excited m-line of the mode is slightly attenuated compared to the neighboring m-lines while the coupling is optimized only for the TM_{03} mode.

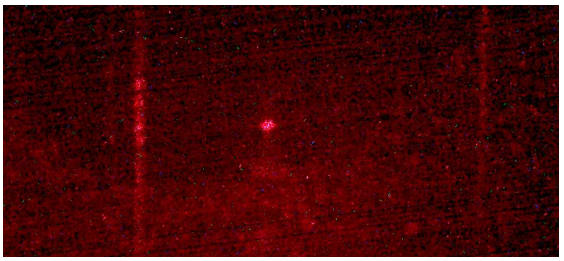

(a) $\rho_{LB} = 2.4\%$

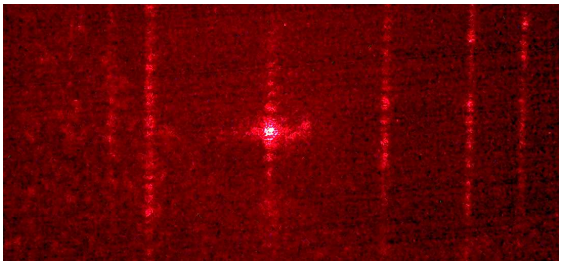

(b) $\rho_{LB} = 2.3\%$

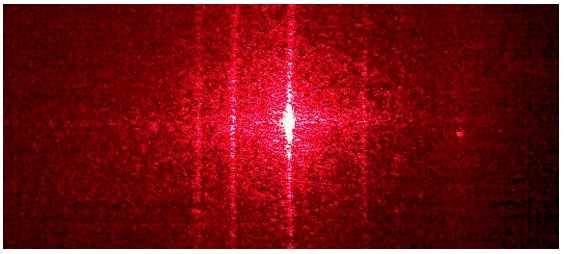

(c) $\rho_{LB} = 2\%$

FIGURE 4.1: High loss modes in Z-cut planar HISoPE waveguides.

Therefore, taking into account the comparison of these two samples, the concentration of lithium atoms in the source melt has to be reduced if we want to improve the propagation quality of our proton exchanged waveguides. It was verified that HISoPE waveguides fabricated at $\rho_{LB} = 2\%$ are totally free from such diffusing modes (see figure 4.1(c)). On the other hand, one should remember that increasing the acidity of the source melt can lead to a degradation of the nonlinear coefficients. Later in the section dedicated to the nonlinear optical characterizations we will verify if the nonlinearities are preserved for HISoPE waveguides realized with 2% of LB and at 300°C.

Such behavior of the optical mode propagation was observed only for Z-cut proton exchanged waveguides but not for X-cut. This indicates that the formation of the waveguiding layers highly depends on crystalline orientation. And, unfortunately, this results not only in different kinetics of the proton exchange, but may also induce propagation losses. Therefore there is a strong need to explain the nature of this propagation losses.

4.2 Crystalline structure of Z-cut $LiNbO_3$ waveguides

The optical characterizations alone cannot explain the presence of these high loss modes in Z-cut HISoPE waveguides. In order to try to understand this phenomenon we will use an X-ray diffractometer to define the crystallographic phases present in the different kinds of planar proton exchanged waveguides. We used the diffraction from the 00.12 planes parallel to the surface of Z-cut $LiNbO_3$ substrate. A study of this family of atomic planes is sufficient to determine all the possible crystalline phases in the proton exchanged waveguides.[98–100,124]

Let us recall that the deformation for the atomic planes parallel to the surface can be described by the next equation (see section 2.3 for details):

$$\varepsilon_{00.12} = -\Delta\theta_{00.12} \cdot \cot\theta_{00.12}, \tag{4.1}$$

where $\theta_{00.12}$ is a Bragg angle of X-ray beam scattered from (00.12) planes. From this relation it is clear that an increase of the inter-plane distance will lead to a reduction of the Bragg angle. The value of $\varepsilon_{00.12}$ for all possible crystalline phases in proton exchanged waveguides is quite well studied and reported in literature.[98–100] As we have already noticed in the paragraph 1.6, the crystalline phases can be represented by a phase diagram (see figure 4.2), where the maximal index change is plotted as a function of the deformation $\varepsilon_{00.12}$ of the waveguiding layer.

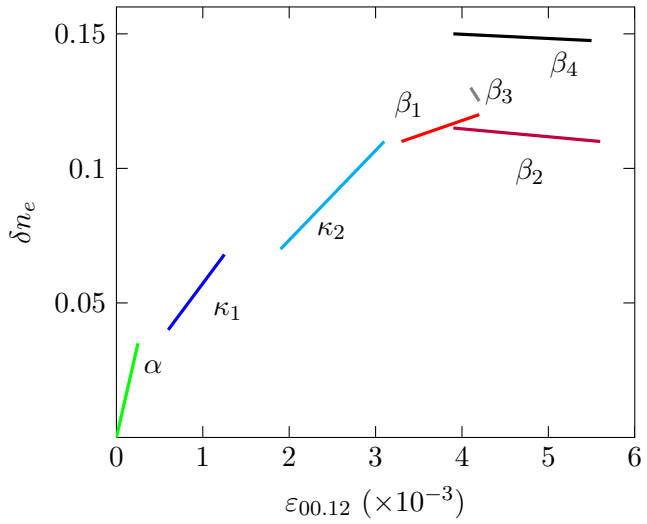

FIGURE 4.2: Phase diagram of proton exchanged waveguides realized on Z-cut $LiNbO_3$ surface.[99]

Also, the crystalline phases of proton exchange waveguides have different nonlinear optical properties as it has been described before in section 1.6. So the structural comparison

of the waveguides fabricated by different techniques should demonstrate the principal characteristic of the HISoPE waveguides and give some preliminary idea about its non-linear properties.

A typical XRD spectrum of bulk $LiNbO_3$ is shown in figure 4.3. A narrow peak corresponds to the Bragg angle of the X-rays scattered from the parallel to the surface (00.12) atomic planes. And it doesn't have any contamination aside. This peak is observed at an angle of 81.7°. However for convenience, in all the following XRD spectra, this value will be used as the origin and the angle will be expressed in seconds of arc.

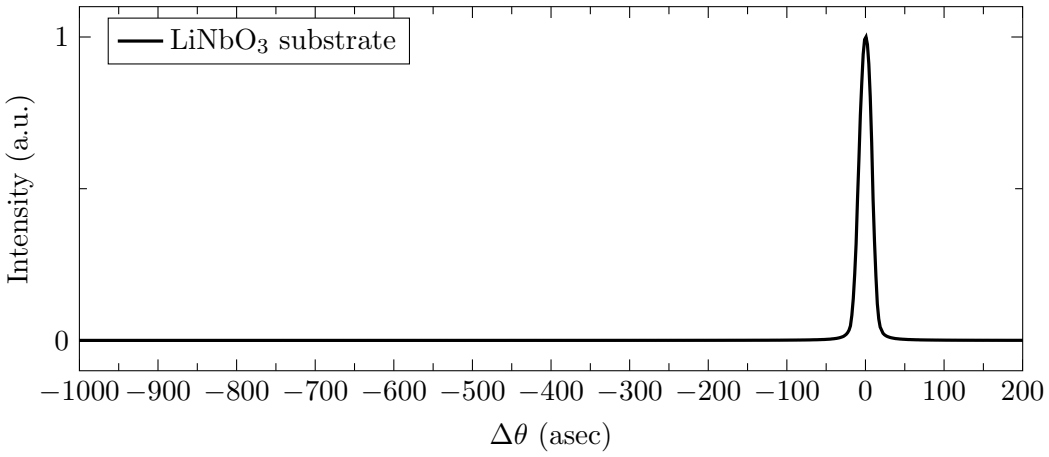

FIGURE 4.3: XRD spectrum from the (00.12) planes of pure $LiNbO_3$ substrate used for waveguide fabrication.

4.2.1 SPE waveguides

SPE waveguides are fabricated using a lithium benzoate concentration $\rho_{LB} > \rho_t$. An example of XRD spectrum of an SPE waveguide fabricated with $\rho_{LB} = 2.9\%$ at 300°C is shown in figure 4.4. A unique peak appears near the main substrate peak meaning that the waveguiding layer consists of one phase only. The angle of $-150''$ corresponds to the α phase. This crystalline phase is characterized by practically unmodified nonlinear coefficients and a weak index change $\delta n_e \leq 0.03$. The shape of the diffraction peak can give a lot of information. If the crystalline lattice of the waveguide is well organized, i.e. there is no homogeneity in the exchanged layer, the peak will be as sharp as the substrate one.

However the peak of the α phase is rather broad and is not separated from the substrate peak. It means that in fact the interface between the substrate and the exchanged layer is not well defined. The concentration of the diffused protons reduces gradually with the depth in SPE waveguides. Thus the interface waveguide-substrate is blured and the deformation $\varepsilon_{00.12}$ is changing gradually too. Consequently, the atomic planes of

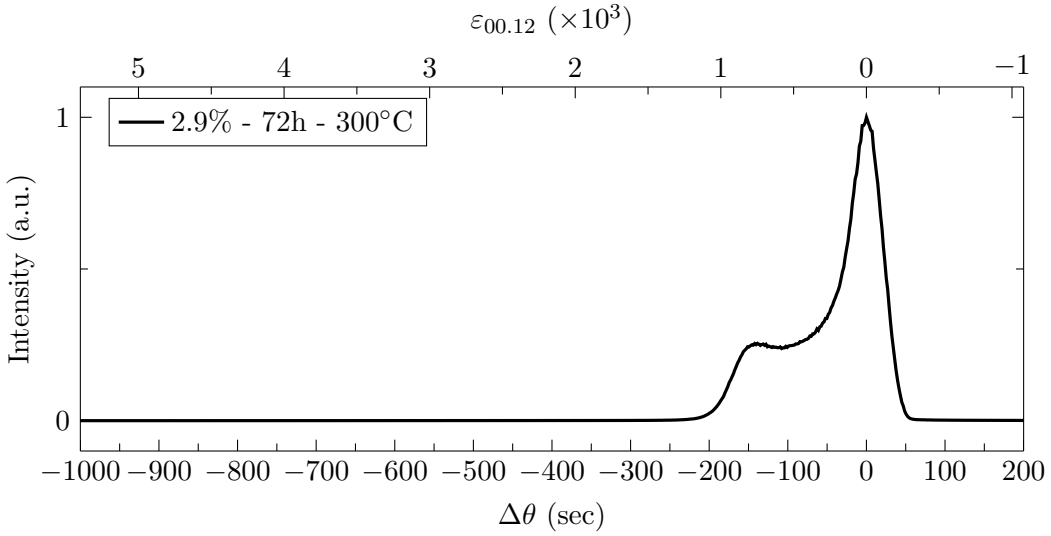

FIGURE 4.4: XRD spectrum from the (00.12) planes of the waveguide fabricated with $\rho_{LB} = 2.9\%$ at 300°C during 3 days. These are the usual fabrication parameters used for SPE technique in our laboratory.

the exchanged layer are characterized by intermediate deformations and diffract X-ray beam between the angles $-150''$ and $0''$.

4.2.2 PE waveguides

The β family crystalline phases are common for what we call PE waveguides. If pure BA is used as the source of the protons, the exchanged layer presents only β_1 and β_2 phases.

An example of XRD spectrum of PE waveguide is given in figure 4.5. The sample was fabricated in pure BA at 360°C during 30 minutes. On the contrary to SPE waveguide, there is no peak corresponding to the phase α. But there are two peaks at angles of $-840''$ and $-580''$. Therefore two crystalline phases are present in the waveguide. Note that the phases are not mixed with each other in this proton exchanged waveguide. Instead, the waveguiding layer is stratified into two sublayers having each a single crystalline phase.

The first peak at $-840''$ corresponds to β_2 phase. The narrow shape of the peak with practically the same width as the substrate peak points on a high crystalline quality of this well-isolated sublayer. The second broad peak around $-580''$ belongs to β_1 phase. According to the shape of the peak, this sublayer is not of the same crystalline quality as the β_2 sublayer. This may due to the fact that this β_1 phase is located between the substrate and the β_2 phase, thus acting as a transition layer. Therefore the higher

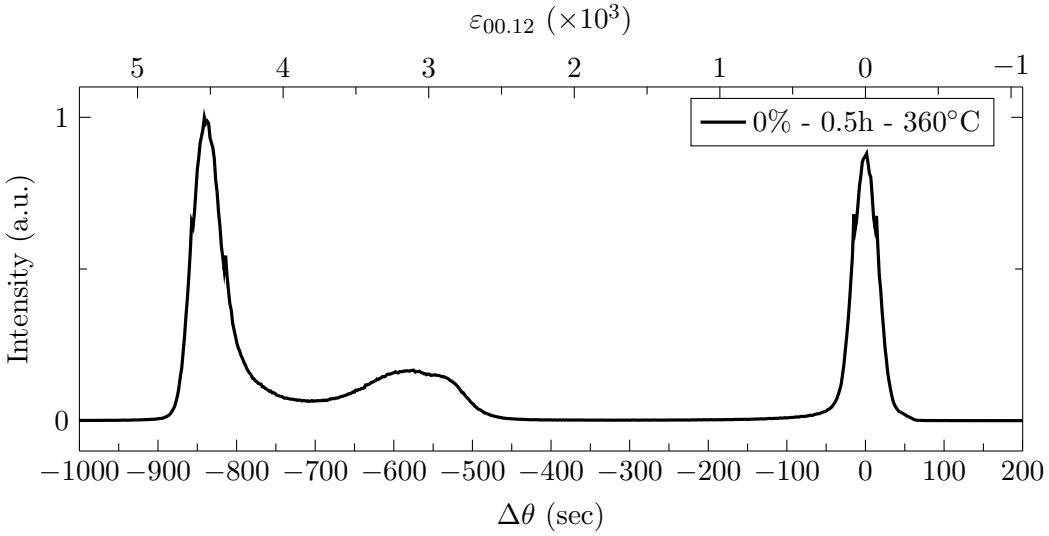

FIGURE 4.5: XRD spectrum from the (00.12) planes of the waveguide fabricated in pure benzoic acid at 300°C during 30 minutes.

amount of the defects in this sublayer could be explained by a double lattice parameters mismatch.

4.2.3 HISoPE waveguides

HISoPE waveguides are very different from SPE and PE waveguides. An example of XRD spectra of an HISoPE sample is given in figure 4.6. The waveguide sample was fabricated using a BA+LB melt with $\rho_{LB} = 2.4\%$ at 300°C during 17 hours. The sharp intense peak at $-490''$ with the same bandwidth as the substrate corresponds to the phase κ_2. Also a slight augmentation of the intensity curve around $-150''$ indicates a small amount of α phase, which is present in the waveguide.

It is interesting to note that this spectrum is very similar to XRD curves of VPE waveguides characterized before in the laboratory or reported in the literature.[25,29,30] Consequently, VPE and HISoPE waveguides have a similar crystalline organization, although the fabrication methods are different.

It is worth mentioning that if the proton exchanged waveguide consists of two or three crystalline phases, they are arranged in a specific way. Concerning HISoPE waveguides, an example is given in figure 4.7. The surface of the planar waveguide was polished at a shallow angle. Therefore centering the X-ray beam on the different zones of the polished surface, we were able to measure spectra corresponding to different depths of the waveguide. With this technique, it is possible to observe the evolution of the XRD spectra, though it is difficult to determine the exact depth of each characterized point of the waveguide. Thus, in figure 4.7, the red curve belongs to the unpolished area of the

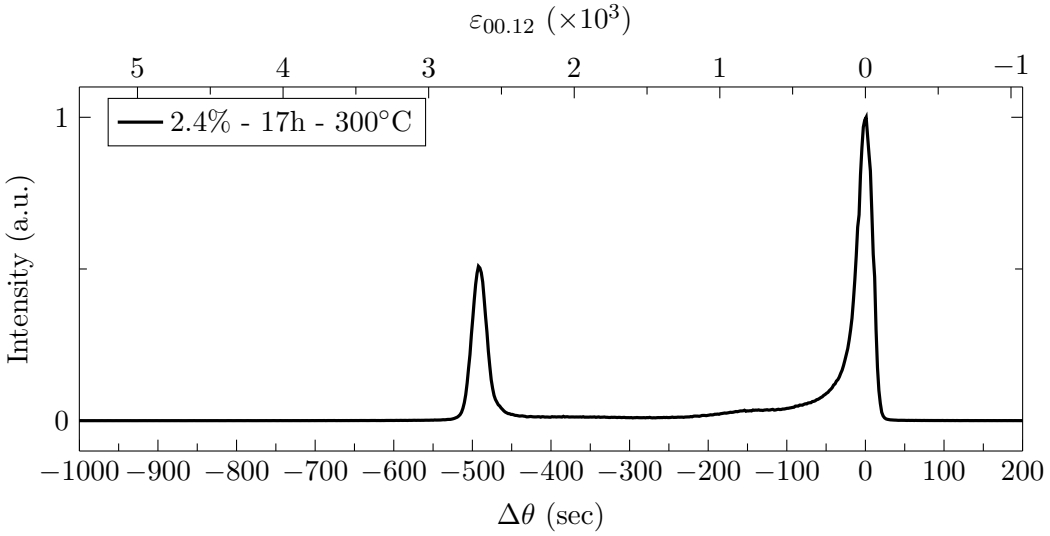

FIGURE 4.6: XRD spectrum of an HISoPE sample fabricated with $\rho_{LB} = 2.4\%$ at 300°C during 17 hours.

HISoPE waveguide. A semilogarithmic scale is used to be able to observe low intensity peaks, which are practically invisible in linear scale. This curve has a sharp peak around $-500''$ corresponding to the phase κ_2. The broad and not so intense peak near $-150''$ indicates the presence of α phase. There is also a transition area between $-400''$ and $-300''$ where there are no peak but the intensity is not zero.

The peak corresponding to κ_2 around $-500''$ reduces and then disappears when the sufficient layer depth from the surface is removed. That is not a surprise if this crystalline phase is formed at the surface of the crystal. Further polishing removes, one by one, the transition layer and α phase, and finally it remains only the narrow substrate peak (blue curve, figure 4.7). The crystalline phase α is placed between κ_2 and the substrate, and contributes apparently to relax the lattice parameters mismatch.

Therefore crystalline phases with higher deformations, i.e. showing the highest absolute value of $\Delta\theta$, are placed near the surface while the phases with lower deformations are formed deeper.

Moreover, the transition layer between κ_2 and α phases between $-400''$ and $-300''$ cannot be considered to be a good sign as the flat shape of the curve indicates an inhomogeneity of this layer. Returning to the high propagation loss intermediate modes, let us study XRD spectra for the samples fabricated with different concentrations of LB. Three XRD spectra of HISoPE waveguides are plotted in figure 4.8. As one can see from the figure that the position of the peak corresponding to κ_2 phase shifts to the left when the concentration of LB is decreased. Naturally, the deformations are induced by a higher concentration of protons in the waveguide fabricated in more acidic sources.

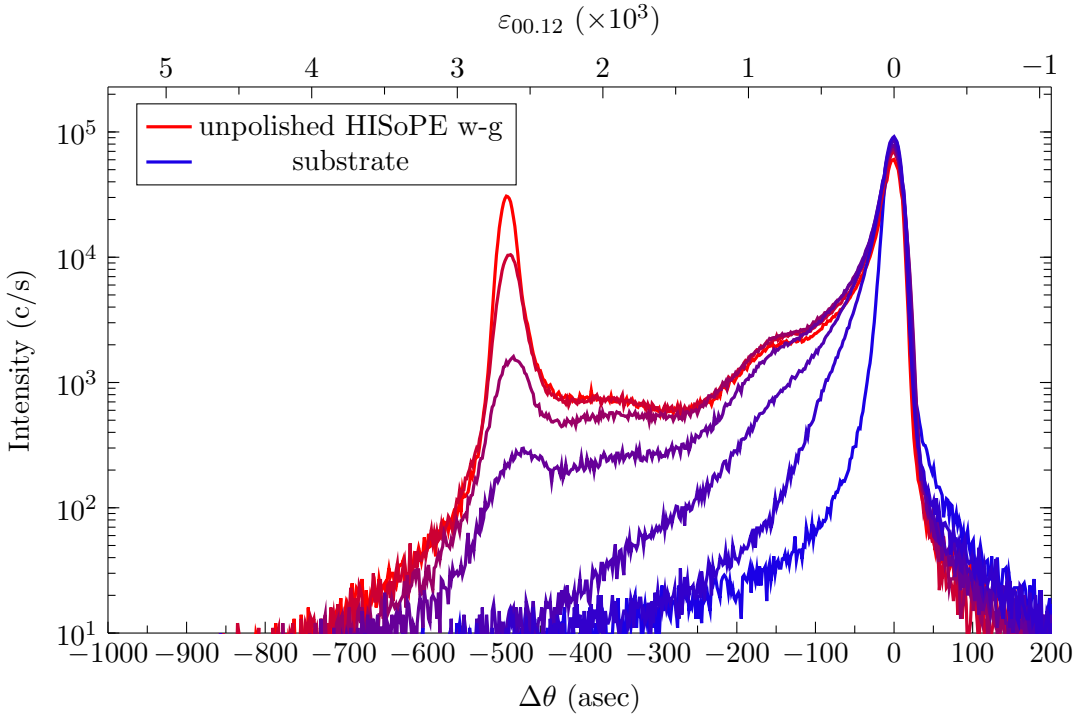

FIGURE 4.7: Spectra of XRD on 00.12 planes of *Z*-cut HISoPE planar waveguide gradually polished to the substrate. The initial waveguide was fabricated with $\rho_{LB} = 2.4\%$ at 300°C during 17 hours in a zirconium container.

The peak around $\Delta\theta = -150''$ corresponding to the phase α is clearly observed. And there is also a transition layer between α and κ_2 phases that is represented by a plateau between $-300''$ and $-400''$. Note that the phase κ_1 may have a peak in this range of angles. But it is hard to say if this transition layer corresponds to another crystalline phase or if it is just a mixture of α and κ_2 phases.

As we have mentioned before in section 4.1.1, the problem referred to high losses propagation modes disappears in HISoPE waveguides by reducing the concentration of LB. The intensity of the transition layer also drops when ρ_{LB} is decreased. Looking on the XRD curves, the difference seems to be not very essential from the crystalline organization point of view. However, we believe that the inhomogeneity of this transition layer is critical for the propagation quality of the waveguide and seems to be responsible for high scattering losses. As one can see in figure 4.8, the difference between the m-lines of the propagating modes is huge. The sample fabricated with $\rho_{LB} = 2.4\%$ is associated with the high loss propagating mode which can be identified by the light spot. The sample fabricated with $\rho_{LB} = 2.3\%$ is much better, and one can observe all the m-lines of the propagating modes. Finally, the waveguide fabricated using the 2% melt has no loss problems of the intermediate mode. The m-line of the excited mode is brighter than the neighbor m-lines and has a very intense spot in its center. This indicates a little coupling between the modes and low losses.

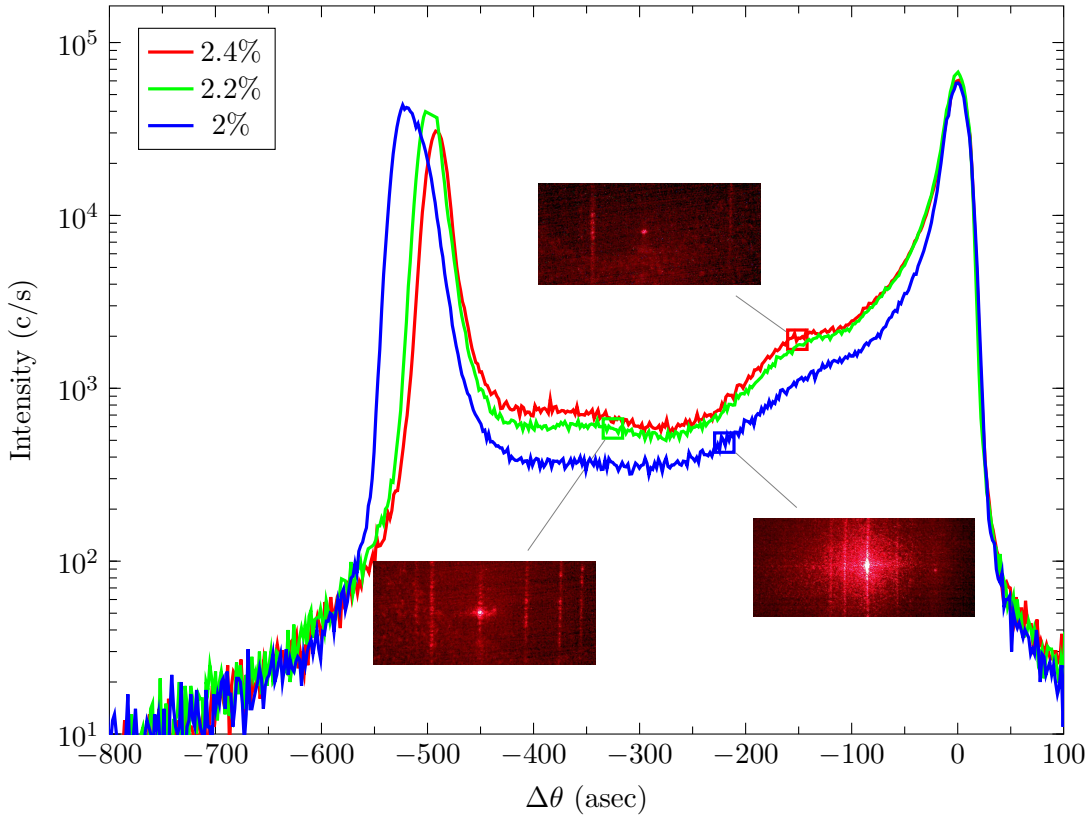

FIGURE 4.8: Spectra of XRD from (00.12) planes of HISoPE planar waveguides. The characterized Z-cut HISoPE waveguides were fabricated during 17 hour at 300°C and with different ρ_{LB}: 2%, 2.3% and 2.4%.

The presence of the inhomogeneous transition layer can explain why only the intermediate propagating modes are suffering from high losses. The reason is demonstrated in figure 4.9. In this figure the index profile of the HISoPE waveguide is plotted with the mode profiles. The step part of the waveguide is composed of the phase κ_2 and the gradient part consists of the phase α. The transitional layer is placed in the middle between κ_2 and α as it was confirmed by the XRD spectra of the polished waveguide (figure 4.7). The fundamental mode TM_{00} has no big problems with losses as most of its energy is confined in the step part of the waveguide (see figure 4.9(a)). However, the modes TM_{01} and TM_{02} have a lot of energy in the high loss transition layer of the waveguide. Finally, the mode TM_{03} has its maximum in the gradient part of the waveguide where there are no problems with the crystalline quality.

Going back to the crystalline phase composition of the HISoPE waveguides, it is worth mentioning that before this work, the phase κ_2 was observed in the waveguides realized either directly by VPE or by annealing of PE waveguides. In the first case, κ_2 is obtained directly, and XRD spectra of VPE waveguides are very similar to HISoPE ones. In the latter case, κ_2 and κ_1 are found for annealing duration too short to fabricate APE waveguides. The post exchange annealing allows the protons to diffuse further from

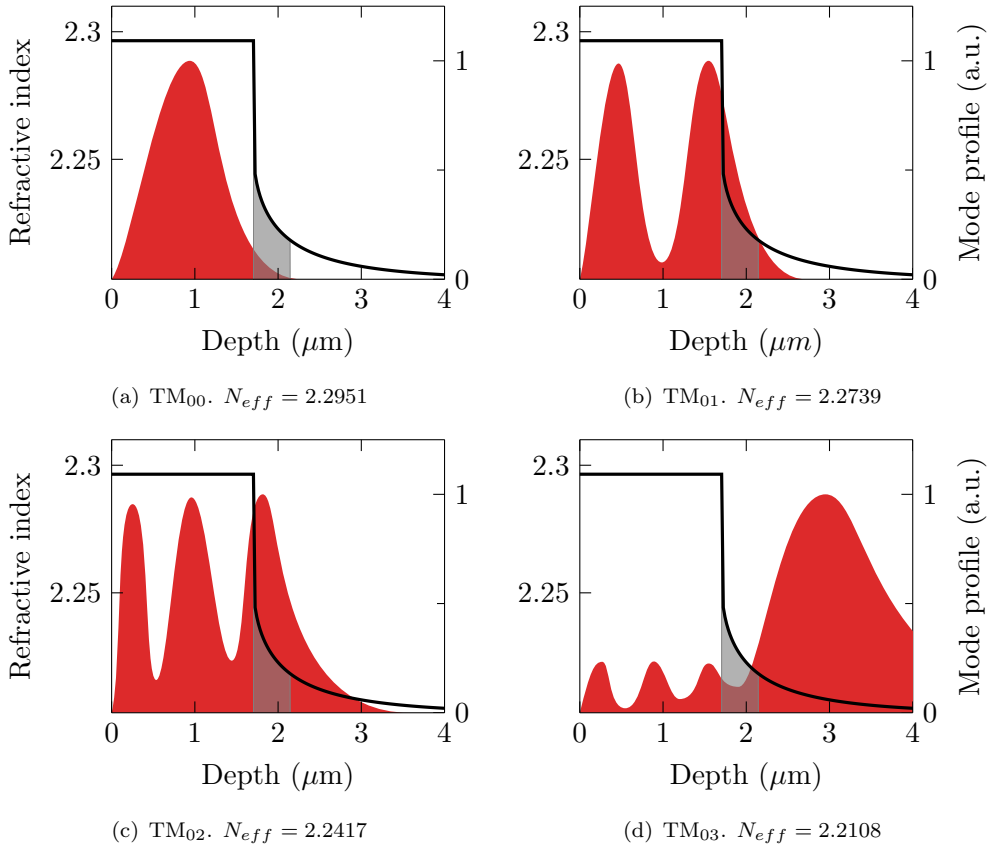

(a) TM_{00}. $N_{eff} = 2.2951$

(b) TM_{01}. $N_{eff} = 2.2739$

(c) TM_{02}. $N_{eff} = 2.2417$

(d) TM_{03}. $N_{eff} = 2.2108$

FIGURE 4.9: Index profile and the propagating modes profiles of the planar HISoPE waveguide on Z-cut $LiNbO_3$ fabricated with $\rho_{LB} = 2.4\%$ at 300°C during 17 hours.

the exchanged layer to the substrate and, therefore, the waveguiding layer consisting of β_i phases transforms to layers containing less protons such as κ_2 and κ_1 phase layers. And finally, the α phase is obtained if the annealing is long enough. But the associated transformation is gradual and occurs via κ_i phases. The layers in κ_i phases obtained by annealing are very inhomogeneous and suffer from high light scattering.[99]

Considering the results of our XRD characterizations, we confirm that the κ_2 phase can be obtained by a direct proton exchange in HISoPE waveguides. A very important thing is that, in this case, the crystalline organization of this phase is very good and is correlated with the good optical quality. However one should eliminate, or at least reduce, the influence of the inhomogeneous transition layer. Reducing the LB concentration in the proton source can solve this problem. But now, one should verify carefully if these waveguides fabricated in more acidic proton sources still present preserved nonlinear properties.

4.3 Nonlinear optical characterizations of planar waveguides

4.3.1 Surface SHG profiling

The observation of similar crystalline organization in VPE and HISoPE waveguides allows to hope that they also present similar optical properties. Planar HISoPE waveguides were found to have low propagating losses. However, the nonlinearities should be verified. The same experimental set-up is identical to the one used for X-cut waveguides and is described in details in the Appendix C.

At first, let us consider a waveguide without non-degraded nonlinear properties. An example of SHG profile of SPE waveguide is shown in figure 4.10. SPE waveguides are known for their non-degraded nonlinearities. The intensity curves in the figure were normalized by corresponding intensities of SHG and fundamental beam reflected from the bulk crystal. The reflected fundamental beam is used to localize the surface of the sample. The index profile of the waveguide superimposed with the SHG signal aims to identify the SHG response of the different parts of the waveguide.

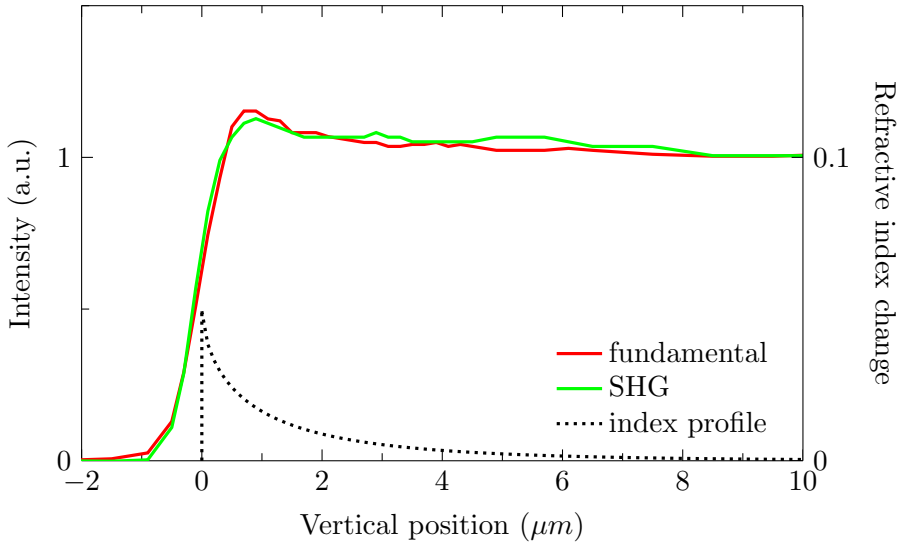

FIGURE 4.10: Surface SHG profiling of SPE waveguide and the corresponding index profile for a wavelength λ=0.633 μm. The sample was fabricated in 2.9% melt of BA and LB at 300°C during 3 days.

The surface of the crystal and, consequently, the waveguide begin when the reflected fundamental intensity rises. The surface can be located where it reaches half the substrate value. The normalized SHG intensity curve (green line) coincides perfectly with the reflected fundamental beam (red line). The SHG intensity is not reduced in the waveguide region compared to the substrate. This indicates an unmodified $\chi_{33}^{(2)}$ in the waveguiding layer.

Now let us have a look at a PE waveguide, which is known to present highly reduced nonlinearities. An example is given in figure 4.11. The waveguide has a step-like index profile with a gradient part. The depth of the waveguide is around 3.5 μm.

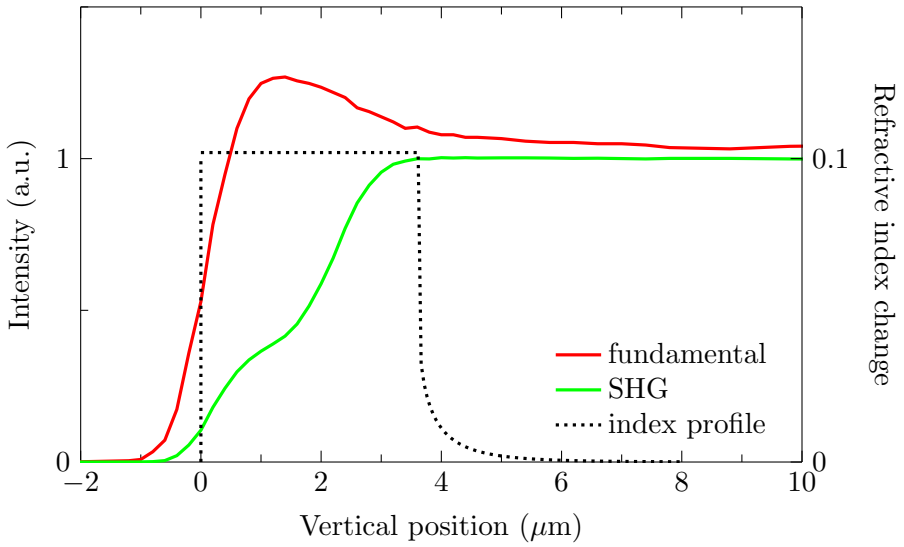

FIGURE 4.11: Surface SHG profiling of PE waveguide and the corresponding index profile for a wavelength λ=0.633 μm. The sample was fabricated in pure BA at 360°C during 30 minutes.

The intensity of the reflected fundamental quickly rises when pointing the surface position. However the SHG intensity curve raises slowly to a plateau value observed in the 3.5 μm layer corresponding to the waveguide. This plateau value is smaller than the response of the substrate. The reduced SHG intensity in the proton exchanged waveguide means that the nonlinear coefficient is degraded in this layer.

The two extreme cases seen above are easy to summarize: the weaker the SHG signal, the worse the nonlinear coefficient in the waveguide. But for HISoPE waveguides we obtained quite interesting results, which are difficult to explain in such a simple way.

An example of surface SHG profiles obtained with HISoPE waveguides are given in the following figures 4.12-4.14. The samples fabricated with different concentrations of LB have step-like index profiles with a gradient part. The maximal refractive index change is around 0.1. Thus the waveguides have good confinement capabilities.

The reflected SHG signal has a strange shape. All the three figures show a peak that is much more intense than the signal reflected from the substrate. Similar peaks have been observed for PE or APE waveguides on $LiNbO_3$.[30,125] They were located at the interface between the waveguide and the substrate, and were associated to the higher diffusion present in this area of the waveguide. For HISoPE waveguides, the peak occurs near the surface of the crystal and not at the interface between the waveguide and the substrate. The width of this peak is correlated with the depth of the waveguide. On the

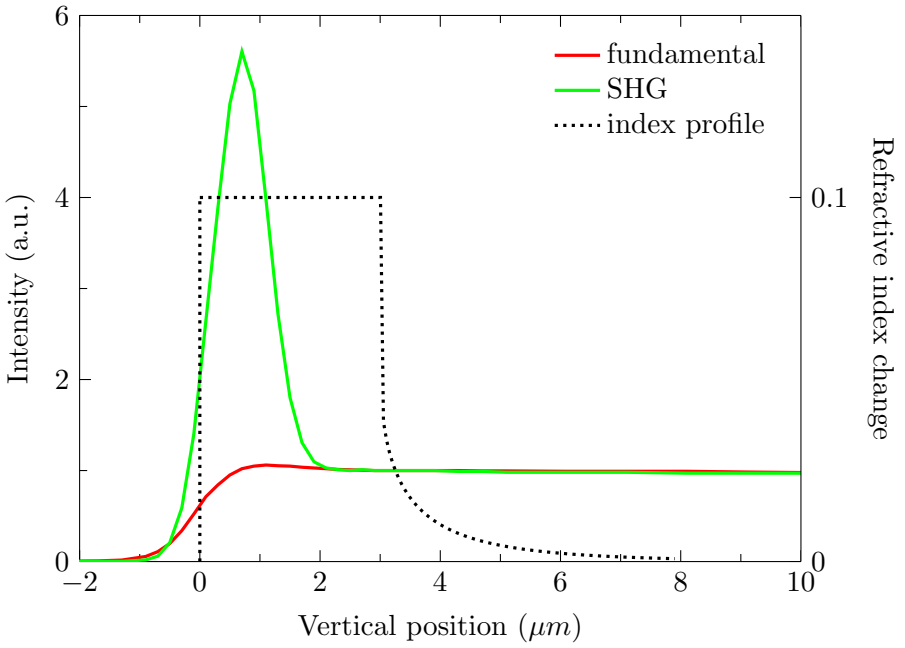

FIGURE 4.12: Surface SHG profiling of HISoPE waveguide and the corresponding index profile for a wavelength $\lambda = 0.633\,\mu$m. The sample was fabricated in BA+LB melt with $\rho_{LB} = 2.3\%$ and at 300°C during 35 hours.

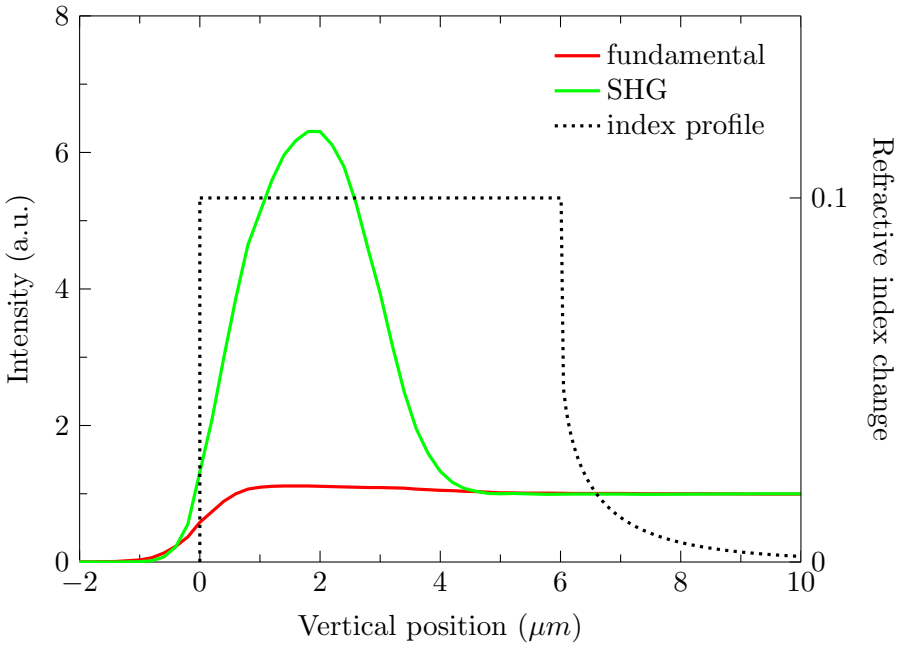

FIGURE 4.13: Surface SHG profiling of HISoPE waveguide and the corresponding index profile for a wavelength $\lambda = 0.633\,\mu$m. The sample was fabricated in BA+LB melt with $\rho_{LB} = 2.2\%$ and at 300°C during 3 days.

observed samples, the full width at half maximum of the peak is always around the $^1/_2$ of the waveguide depth.

Finally the maximum of the peak increases when the concentration of LB used for

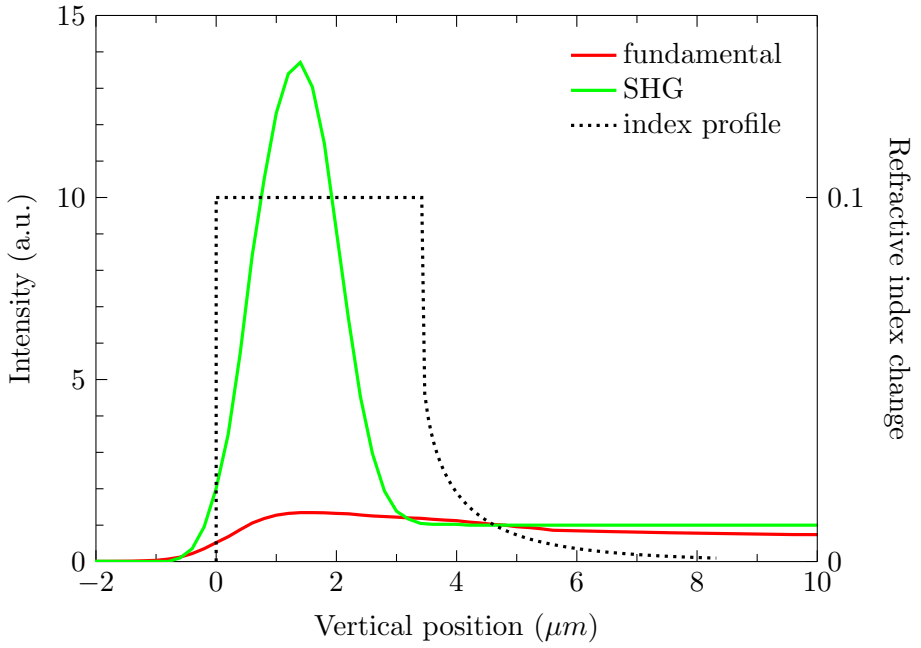

FIGURE 4.14: Surface SHG profiling of HISoPE waveguide and the corresponding index profile for a wavelength λ=0.633μm. The sample was fabricated in BA+LB melt with $\rho_{LB} = 2\%$ and at 300°C during 40 hours.

waveguide fabrication is reduced. Therefore it seems that these peaks cannot be fully explained by the discontinuity[125] of the value of the nonlinear coefficient between the air and the crystal.

It is not very likely that the increase of the SHG signal can be explained by the increase of the nonlinear coefficient in the waveguide. Therefore the reason for this SHG peak is not clear. However, these measurements seam to indicate that the nonlinearities in the HISoPE waveguide are not degraded.

4.3.2 SHG imaging by confocal microscopy

In collaboration with Hervé Rigneault from the Fresnel Institute in Marseille, we studied our HISoPE waveguides using SHG imaging by confocal microscopy in order to confirm and validate the results obtained by reflected SHG profiling. The image of the end facet of the planar HISoPE waveguide is shown in figure 4.15.

The intense horizontal line corresponds to an enhanced SHG intensity in the planar waveguide. The substrate is below and the air is above the waveguide. Therefore this experiment confirm the curves of reflected SHG described in section 4.3.1. We don't think that the intensity increase in the waveguide can be interpreted as an increase of the nonlinear coefficient $\chi^{(2)}$, but the presence of the index profile can modify the radiation diagram of the SHG and explain the observed phenomenon.

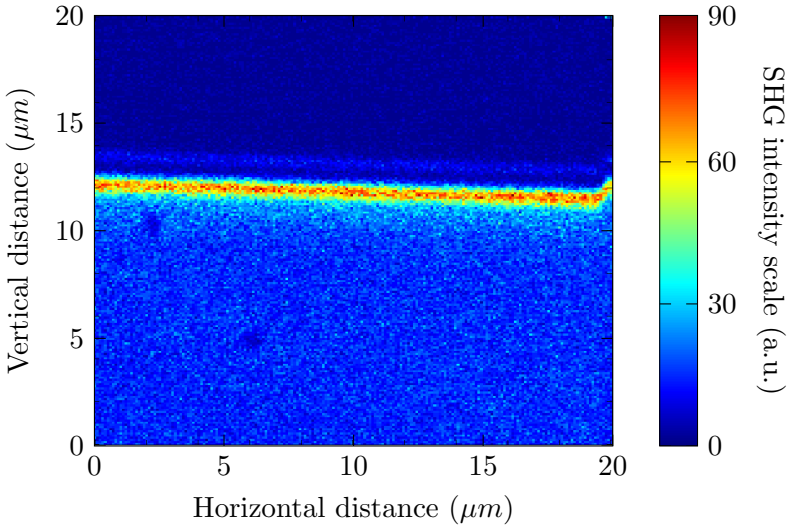

FIGURE 4.15: SHG image of side view of the planar waveguide polished end face. The $\chi^{(2)}_{33}$ coefficient is probed. The waveguide was fabricated in the 2% melt at 300°C during 9 hours. The depth of the waveguide is around 1.6 μm.

4.3.3 Measurement of the electro-optical coefficient by absorption

Another characterization of a set of proton exchanged waveguides fabricated in our laboratory with different recipes, was carried out by Sergey Kostritskii and collaborators in Russia. It consists in monitoring the absorption edge of the waveguides in the UV region, which allows calculating the reduction of the electro-optical coefficient[126]. The results are summarized in table 4.2.

TABLE 4.2: Electro-optical coefficients evaluated by absorption method[126]. The given values of r_{33} are the relation of the modified coefficient and the coefficient of the substrate.

Waveguide	Profile	Fabrication parameters	Evaluated r_{33}
substrate	-	-	1
#1	APE	fabricated in Russia	0.9
#2	SPE	2.9%, 300°C, 3 days	0.85
#3	HISoPE	2.3%, 300°C, 35 hours	0.25

At this stage, we have to admit that these results tend to be in contradiction with the surface SHG we performed, at least if we consider that the nonlinear and electro-optical coefficients are proportional. Indeed, on one hand, the UV absorption study shows that the value of the r_{33} in HISoPE waveguides is similar to that of PE waveguides[127], but on the other hand, surface SHG profiling distinguish well these two types of proton exchanged waveguides.

For this reason we fabricated HISoPE channel waveguides to characterize directly the nonlinear properties of these waveguides.

4.4 Channel HISoPE waveguides

Knowing the problem of high loss modes in HISoPE waveguides fabricated with LB concentrations close to ρ_t, we made a set of samples using $\rho_{LB} = 2\%$. We found no high loss modes in the corresponding planar waveguides realized with this concentration. Thus, we chose this fabrication parameter to further realize channel HISoPE waveguide.

The mask pattern was the same than the one used for X-cut $LiNbO_3$ waveguides. Therefore three widths are available: 1, 1.5 and 2 μm. The fabrication procedure was identical to the one described in section 3.2.1. Each sample has 9 groups of six waveguides each. The length of the samples is around 2.5 cm after fabrication and end facets polishing. As the opposite side of the sample is not protected by any layer deposition, it is exposed to the acid melt during the proton exchange. Therefore, on this side a planar waveguide is present for characterization, which is very useful to measure the index profile of the waveguide using the m-lines technique.

4.4.1 Propagation losses

A Fabry-Perot cavity technique was used to measure the propagation losses. It is described in Appendix B. Despite the fact that the planar waveguides on the opposite side of the sample were of good optical quality and did not suffer from light scattering, the channel HISoPE waveguides showed very high propagation losses ≥ 5 dB/cm.

The main mechanism of the losses in channel HISoPE waveguides on Z-cut $LiNbO_3$ was identified by observing the far field at the output of the samples. A strong TM-TE polarization coupling was revealed. Let us concentrate on this phenomenon in the next paragraph.

4.4.2 Hybrid modes

Due to their crystalline orientation, the planar Z-cut proton exchanged waveguides are not expected to show so-called hybrid modes (look for details in section 2.4). Thus, the channel waveguides were expected to have even less problems with this phenomenon than the X-cut. However, the observation of a strong TM-TE polarization coupling implies that the strains and stresses inducing this phenomenon are not negligible in the channel waveguides. This may be explained by the fact the on Z-cut substrates we reduced ρ_{LB} to avoid the problem of lossy modes, but as observed with the X-rays, this induces higher strains in the waveguides and stresses at their interfaces with the substrate.

In figure 4.17, an image of the hybrid modes is presented. A laser beam at the wavelength 633 nm is coupled into the channel waveguide (figure 4.16). The hybrid modes that radiate into the substrate are observed on a paper screen. The polarizer is used to separate TE and TM polarizations. By measuring the angles θ between the waveguide direction and the light rays of the hybrid modes, one can calculate the associated effective indices of the modes. The measurement confirmed that N_{eff} of the hybrid modes correspond well to the N_{eff} of the propagating modes in the channel waveguides. The effective indices of the radiating hybrid modes are smaller than the ordinary index of the substrate n_o. If $N_{eff} > n_o$, the mode propagates in the waveguide without losses even if there is a TM-TE coupling.

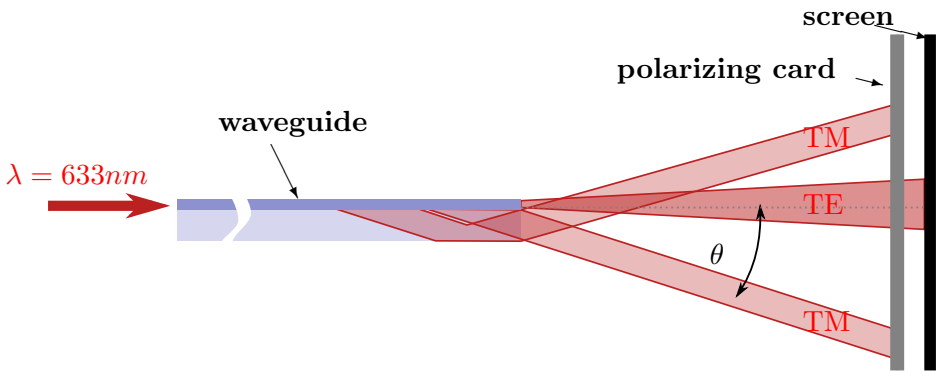

FIGURE 4.16: Schematics of the experimental set-up for observing hybrid modes is the same as was used for characterization of the X-cut waveguides in paragraph 3.5.3.

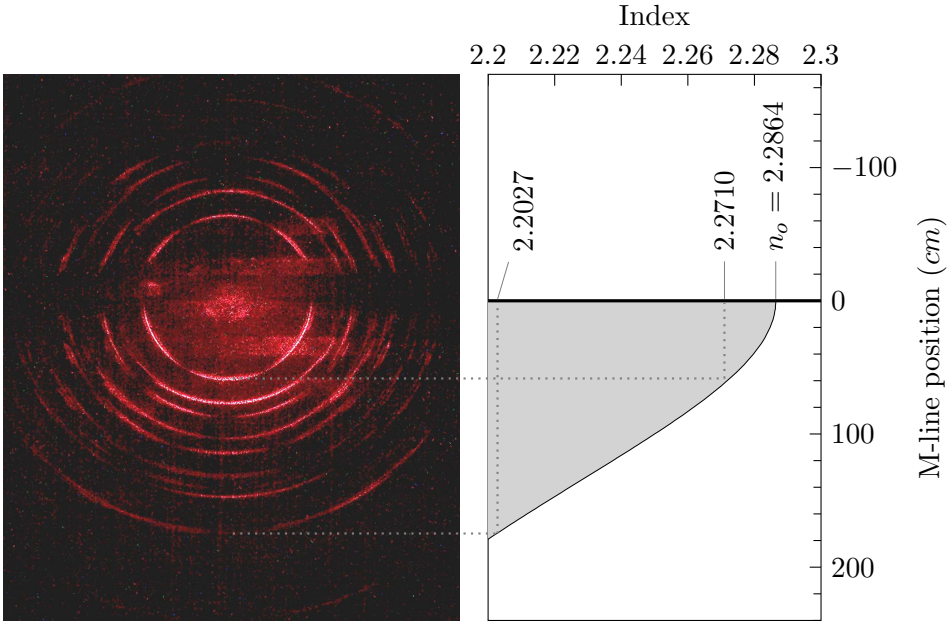

FIGURE 4.17: Observation of the TE polarized hybrid modes in HISoPE channel waveguides: on the left, the picture of the screen is placed, and on the right, the curve describes the effective index of the hybryd modes as a function of the distance between the center and the m-line.

Unfortunately using a more acidic proton source with $\rho_{LB} = 2$ to eliminate the problem of high diffusing modes, brought another problem as the strains and stresses are then higher. This induces another loss mechanism in channel waveguides. Indeed, in a planar waveguide, the crystal is free to expand in the direction perpendicular to the surface. But in a channel waveguide, the substrate is also present on the side of the waveguides preventing the crystal to expand freely in any direction (see figure 4.18).

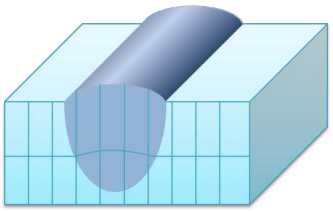

FIGURE 4.18: Schematic representation of the cristalline deformation in channel HISoPE waveguides.

Strain and stresses in X and Y directions are no longer the same and in the waveguide the crystal becomes biaxial with principal axes different from the principal axes of the substrate. That is why hybrid modes are present in channel waveguides, though they are not observed in planar Z-cut waveguides.

4.4.3 SHG imaging of HISoPE channel waveguides

As up to now, all the HISoPE waveguiges fabricated on Z-cut $LiNbO_3$ suffer from high losses, we did not succeed to fabricate any working PPLN waveguide with this technique. However, we used SHG confocal microscopy to monitor the reflected SHG signal and observe the modifications of the nonlinear coefficients. The propagation losses are not expected to influence the results very much.

In figure 4.19, SHG 2D intensity profiles are shown, which were obtained in two different configurations. The observation plane is either an XY plane (observation of the surface) or an XZ plane (observation of the end facet).

SHG imaging of the end facet of the channel waveguide (figure 4.19(a)) shows a result similar to those observed with planar waveguides (section 4.3.2). In this configuration the nonlinear coefficient $\chi^{(2)}_{33}$ is probed. The intensity in the waveguide is brighter than in the substrate. But it seems that it is brighter only at the interfaces of the waveguide while the center of the waveguide has the same intensity as the bulk crystal. Anyway, there is no reduction of the second harmonic signal compared to that of the substrate if we trust this image.

In figure 4.19(b), a view of the surface is presented. In this position of the sample, the coefficient $\chi_{22}^{(2)}$ is probed. One can see that in this case the SHG signals in the channel waveguides are smaller than that of the substrate.

Therefore, both images are difficult to interpret. Before concluding that $\chi_{22}^{(2)}$ is reduced while $\chi_{33}^{(2)}$ is increased one has to keep in mind that, as the refractive index change in HISoPE waveguides is rather high, one cannot neglect the lens effect due to the waveguides which can affect both the focusing and the collecting processes. More investigations and modeling are necessary before extracting precise information on the values of the nonlinear coefficients from these local SHG measurements.

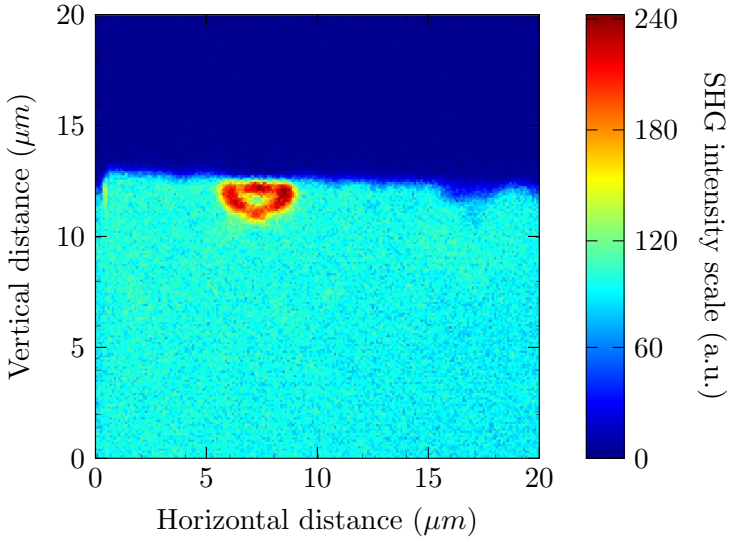

(a) SHG intensity image of the end face of the sample

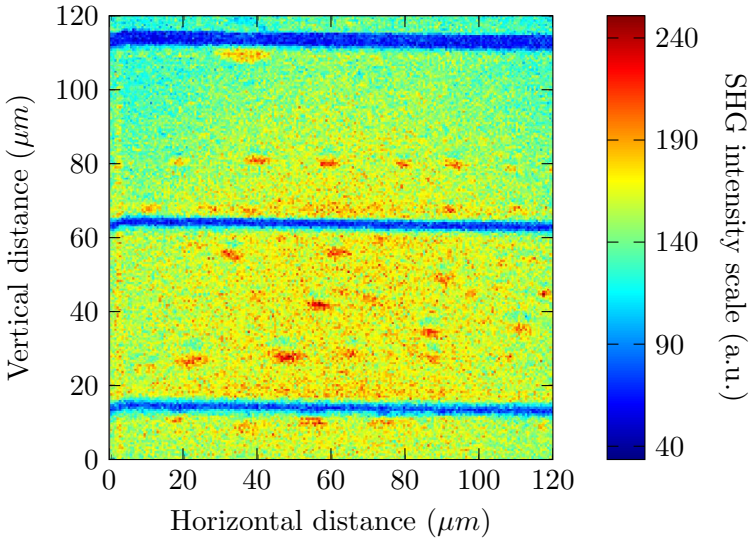

(b) SHG intensity image of the surface

FIGURE 4.19: SHG image of: (a) - side view of the planar waveguide polished end face, and (b) - view from the top. The waveguide was fabricated in the 2% melt at 300°C during 9 hours. The depth of the waveguide is around 1.6 μm.

4.5 Buried proton exchanged waveguides

As we have mentioned in the introductory chapter of this manuscript, HISoPE waveguides with their complex shape of index profile (step+gradient) were initially considered as a nice means to fabricate buried waveguides with a better optical confinement. Buried waveguides are interesting as they present a rather symmetric index profile and, therefore, the fundamental modes at different wavelengths have their maxima at the same depth. This guaranties a good overlap between these modes and, therefore, a good conversion efficiency in nonlinear interactions. The symmetric profile also optimizes the coupling between the waveguide and standard optical fibers. In addition, the fact that the waveguide is buried means that the layer which covers the waveguide, serves as a protection layer reducing the losses due to the surface defects.

Therefore, taking into account the propagation loss problems in surface channel HISoPE waveguides, we explored in parallel the buried waveguides potential, using the HISoPE method in combination with the RPE technique.

The first buried waveguides were fabricated on a PPLN substrate with periods ranging from 15.6 μm to 16.6 μm. The mask openings for the channel waveguides were 4, 5, 6, 7 and 8 μm.

Though the value of the period for quasi phase matching (QPM) can be calculated in advance for a concrete waveguide, it is useful to have a wide range of periods as the phase matching conditions are very sensible to the actual index profile of the channel waveguide under test. This increases the chance to observe the desired phase matching within the tuning range of our laser, even if the fabrication results in waveguides with somehow different dimensions or maximum index change than expected.

The depth was controlled by measuring the effective indices of the planar waveguide on the opposite side of the sample. The reconstructed index profile in figure 4.20 shows the initial HISoPE waveguide. The depth of the step part of the waveguide is around 1.5 μm. Then the sample was immersed in an *Li*-rich melt of salts KNO_3:$NaNO_3$:$LiNO_3$ with a proportion ratio 1:1:0.1 for 16 hours and at a temperature of 300°C. This melt is traditionally used for RPE.[22,77,128] The melting points for the salts KNO_3, $NaNO_3$ and $LiNO_3$ are 334°C, 308°C and 264°C, respectively. But in this particular ratio 1:1:0.1 they form so-called eutectic system, i.e. the melting temperature of the mixture decreases down to 120°C.[129] The low melting point of KNO_3:$NaNO_3$:$LiNO_3$ melt gives a very comfortable range of working temperatures.

The choice of the temperature of the RPE is essential as we want to avoid any annealing effect on the waveguide, i.e. the gradient part of the profile should not be modified. Note

that it has already been verified in the laboratory, that the annealing at a temperature lower or equal to the exchange temperature has a small, or even no, effect on the index profile. We therefore chose to work at the temperature of 300°C to have a fast reverse exchange process without annealing effects.[30]

As one can see in figure 4.20, the extraordinary refractive index has been reduced near the surface after 16 hours of RPE and now the waveguide is buried. However m-lines characterization showed that it was multimode at 1.5 μm with such a refractive index profile.

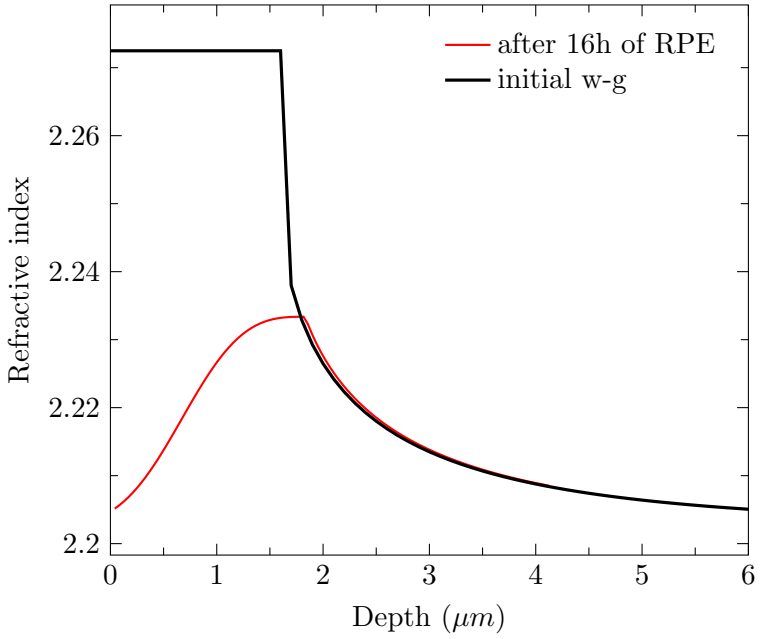

FIGURE 4.20: Index profile of the initial HISoPE waveguide and the waveguide obtained after 16 hours of RPE in a melt of KNO_3:$NaNO_3$:$LiNO_3$ with a proportion ratio 1:1:0.1 respectively and at the temperature of 300°C.

Therefore, a 24 hour RPE procedure was added. At this point it was no longer possible to measure the effective indices of the waveguide by the prism coupling technique. The waveguide is deeply buried into the substrate, and due to the increased distance between the waveguide and the prisms, the tunnel effect is no longer effective. We therefore polished the end faces for further optical characterizations without knowing precisely its index profile.

4.5.1 Propagation losses of the buried waveguides

Propagation losses were measured using the Fabry-Perot method, i.e. by measuring the resonances of the cavity formed between the polished end facets of the waveguide. This method is described in Appendix B in more details. Here we will discuss the results only.

At first, it was verified that the waveguides formed through the mask openings $\geq 5\,\mu$m were multimode at the wavelength $\lambda = 1.55\,\mu$m. And only $4\,\mu$m waveguides were singlemode such that we continued to work with these waveguides only.

The measured propagation losses were between 2 and 4 dB/cm. These rather high values of losses indicate that these waveguides are far from being optimized.

4.5.2 Near field mode observation

In order to find the reason for the high propagation losses the near field was observed at the output of the waveguides. A tunable laser in the telecom range (Tunics, Yenista Optics) was used as light source at a wavelength around $1.5\,\mu$m and was injected into the waveguide using optical fiber. The output of the waveguide was collimated by an aspheric lens and sent to an IR camera to image the mode.

The waveguides fabricated through $4\,\mu$m mask openings were singlemode. But a strange behavior was noticed while tuning the wavelength of the injected light. The spot corresponding to the propagating modes oscillated in a direction parallel to the surface of the sample. In figure 4.21 we present the two extreme positions.

(a) (b)

FIGURE 4.21: Variation of the position of the spot at the output of the waveguide as a function of the coupled wavelength. The amplitude of variation is on the order of the waveguide width of $4\,\mu$m.

This observation indicates that the fabricated structure behaves like a directional coupler. This can be explained considering that the reverse exchange, performed through an SiO_2 mask, does not extend laterally as much as the direct exchange and tends to 'cut' the initial waveguide into two strongly coupled parallel waveguides behaving as directional coupler (see figure 4.22(a)).

Nevertheless, considering the problem with the profile, these realizations were the very first attempt to fabricate buried waveguides from the HISoPE ones. So we continued to examine their nonlinear properties.

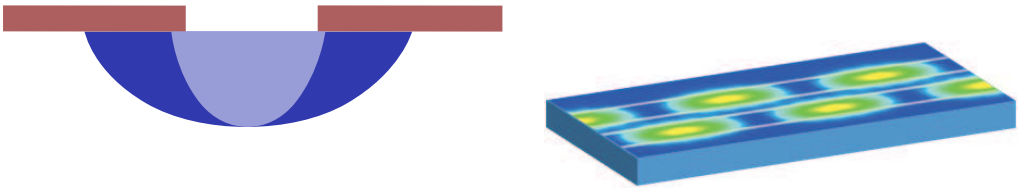

(a) (b)

FIGURE 4.22: Schematics of the channel waveguide profile after RPE (a), which can behave as a directional coupler (b).

4.5.3 SHG in buried waveguides

The measurement of the second harmonic generation in buried waveguides confirmed the great problems with the corresponding index profile of the buried waveguides.

For characterization, we used only the waveguides with 4 μm in width as the others were multimode at $\lambda = 1.5\,\mu$m. Thanks to the different quasi phase matching periods on the sample, we were able to find several waveguides presenting an SHG response in the tuning range of the Tunics laser (1540-1610 nm). A standard optical fiber was used to inject the light. An aspheric lens collected the light at the output of the waveguide and directed it into a Si detector. The pump power emerging from the fundamental mode was measured using a detector sensible in the IR range and a dichroic mirror to separate it from the second harmonic (figure 4.23).

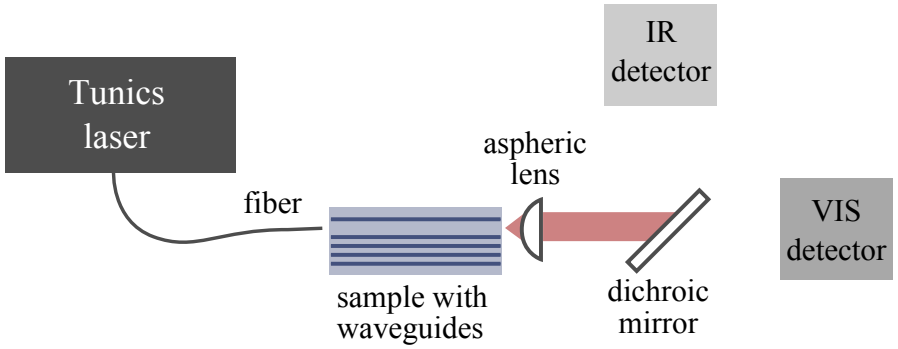

FIGURE 4.23: Schematic of the employed SHG measurement set-up.

Three SHG intensity curves are plotted in figure 4.24. They represent the intensity of the second harmonic as a function of the injected wavelength. We used waveguides with three different poling periods: 16.6 μm, 16.5 μm and 16.3 μm. The waveguides associated with the poling period $\Lambda = 16.4\,\mu$m were found to be damaged, and so they are not represented.

The obtained spectra are far from the theoretical sinc function shape. At least two main peaks are present on each SHG curve instead. The propagation losses measured for these waveguides are 2.2 dB/cm for $\Lambda = 16.6\,\mu$m, 2.7 dB/cm for $\Lambda = 16.5\,\mu$m and 3.7 dB/cm

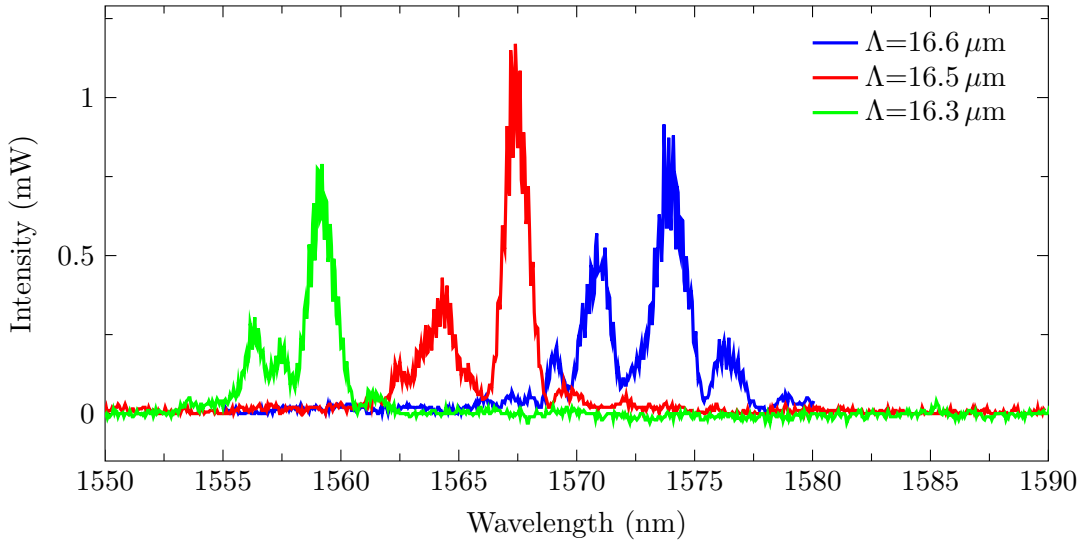

FIGURE 4.24: SHG curves of the buried proton exchanged PPLN waveguide with periods 16.6 μm, 16.5 μm and 16.3 μm. Injected power is 5 mW.

for $\Lambda = 16.3\,\mu$m. Taking into account these propagation losses the conversion efficiency was calculated for the best peaks of each curve.

The best value is around 40% $W^{-1}cm^{-2}$. This is quite surprising as this conversion is rather good. The different positions of the two main peaks in the SHG spectra cannot be explained by the multimode nature of the waveguides at the shortest pump wavelength. The distance between the peaks is too small and corresponds to an effective index difference on the order of 10^{-4} only. But this situation is quite compatible with the directional coupler configuration. The RPE process cuts the waveguide into two which are practically identical and strongly coupled. A difference of 10^{-4} between the effective indices of the propagating mode can be due to a small dimensional difference, and explains the observed SHG spectra. As the twin waveguides are very close, the fundamental power rapidly moves from one waveguide to the other (figure 4.22(b)), generating slightly different SHG waves which also travel in both waveguides. At the output, we detected both SHG intensities at the same time, which explains the two intense peaks, which are observed for each period.

Another consequence of the optical coupler configuration is that the effective length producing each of the two peaks is actually half of the sample length. The effective conversion efficiency, re-calculated taking into account this effective interacting length, is then as high as 160% $W^{-1}cm^{-2}$, which is a very good result compared to the published values.[36,37]

4.5.4 Spontaneous parametric down conversion

Spontaneous parametric down conversion (SPDC) experiments also confirmed that the phase matching condition is satisfied for several pump wavelengths. The measured SPDC intensity curves of the buried waveguide are in figure 4.25.

At the pump wavelength of 780.2 nm two families of signal and idler modes are present on the curve. The idler of the first family is not observable as, unfortunately, its wavelength is out of the detector sensibility range. At the pump wavelength of 781.5 nm, the second family is already at the degenerate wavelength of 1555 nm. But now one can observe both the idler and the signal of the first family on the SPDC spectrum. And finally, the first family reaches degeneracy when the pump wavelength is 781.7 nm.

Therefore this experiment confirmed the directional coupler nature of this buried waveguide. Considering the rather high propagating losses and the index profile of the waveguide, the conversion intensity around 160% $W^{-1}cm^{-2}$ is a very promising result. Note that theoretically the value of the conversion efficiency in an ideal buried waveguides with $\delta n_e = 0.03$, is 300% $W^{-1}cm^{-2}$.[36,37] It is a reasonable goal for a second generation of buried waveguides realized by a combination of the HISoPE and RPE processes.

However, to reach such a conversion efficiency it will be necessary to control the size of the waveguide and to avoid to cut it into two parallel waveguides during the RPE process. In order to reach this result, an important parameter to monitor is the kinetics of the RPE process.

4.6 Kinetics of RPE

To understand the fabrication of a directional coupler during the RPE process one has to keep in mind several parameters:

- The proton exchange is slightly faster along X-axis than along Z-axis.[108] Thus it tends to widen the waveguide realized in Z-cut $LiNbO_3$ as the X-axis is perpendicular to the waveguides.
- The RPE kinetics dramatically depends on the nature of the exchanged layer and is much faster in the step region than in the graded one.

This last point was established by the following preliminary study.

A $3''$ wafer of $LiNbO_3$ was exchanged in a melt of benzoic acid and lithium benzoate with concentration $\rho_{LB} = 2\%$ for 3 days at a temperature of 300°C. Then the wafer was

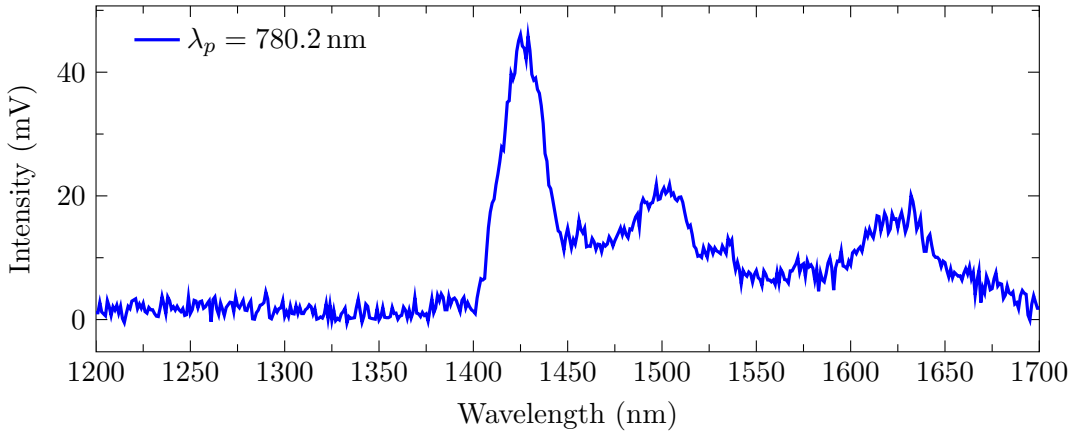

(a) Two families of signal and idler modes can be identified. The second family is totally observed: $\lambda_{s_2} = 1500\,\text{nm}$ and $\lambda_{i_2} = 1625\,\text{nm}$. The first family is represented by the peak of the signal at $\lambda_{s_1} = 1425\,\text{nm}$ while the idler is out of the detecting range.

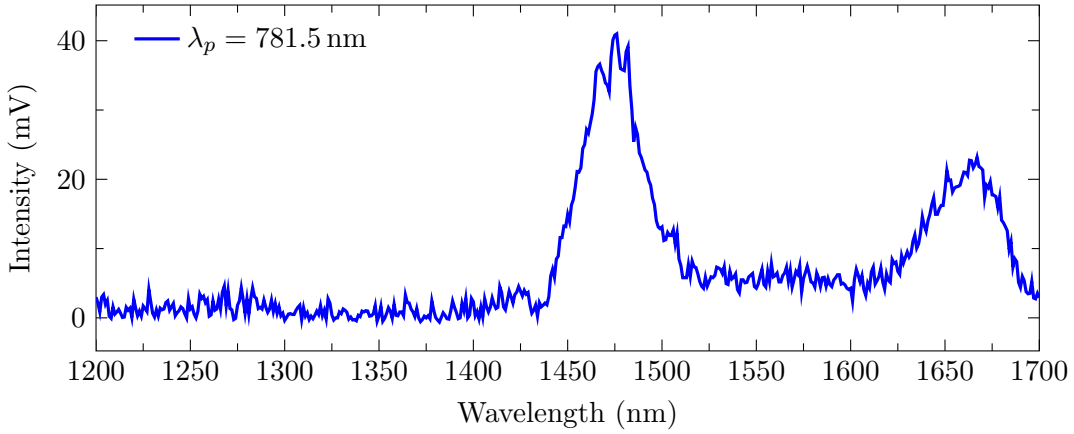

(b) The second family of signal and idler modes is observed at a degenerate wavelength. Moreover, the first family is observed.

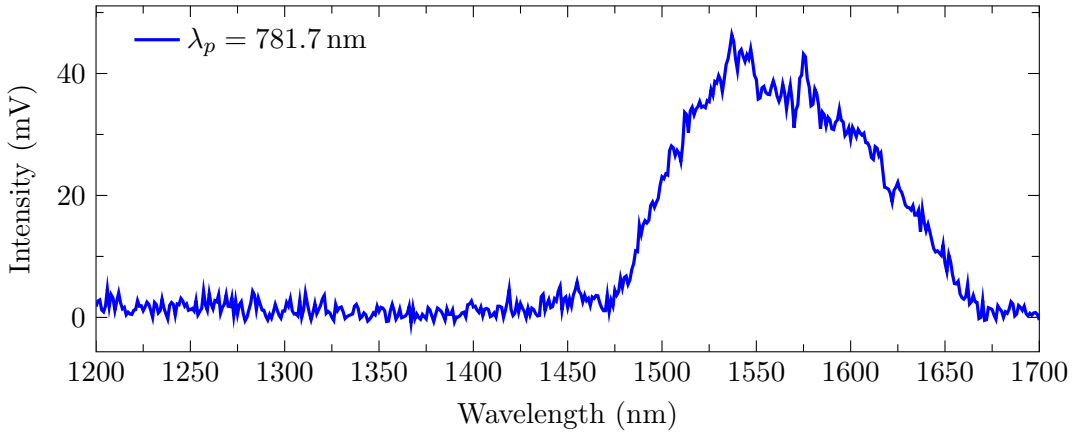

(c) The first family of signal and idler modes is close to degeneracy.

FIGURE 4.25: Observation of the different families of signal and idler frequencies in spontaneous parametric down conversion (SPDC) experiment. The idler of the first family is never observed as its wavelength is out of the detector sensibility range. The PPLN waveguide under test has a poling period $\Lambda = 16.3\,\mu\text{m}$.

cut into small samples. RPE was carried out in a melt of KNO_3:$NaNO_3$:$LiNO_3$ with a proportion ratio 1:1:0.1, respectively, and at a temperature of 300°C. All the samples were plunged in this melt simultaneously but pulled out at different times in order to study the influence of the RPE process on the waveguides.

In figure 4.26, the refractive index profiles of all the waveguides are given. The initial HISoPE waveguide presented a complex profile with a step section of 3.5 μm followed by a gradient section extending over 3 μm. As one can see, the shape of the gradient part of the profile is not modified, which indicates that in these conditions the annealing effect is negligible. One can also see that the RPE process is extremely fast in the step region. After five hours the 3.5 μm step is totally 'erased'. And then the RPE slows down. The profiles of the waveguides with 5 and 8 hours of RPE are almost identical, and after 16 hours of RPE, the erased section is only half of a micron deeper.

In figure 4.27, the depths of the erased part of the profile are plotted as a function of time. This figure shows that the RPE process dramatically changes when it reaches the interface between the step and the gradient section of the initial complex index profile.

The significant reduction of the RPE kinetics in the gradient part is a nice advantage to fabricate buried waveguides. The RPE erases the step part of the waveguide very quickly but then stops in the gradient part. This means that there is no need for a very precise time control of the RPE and that the thickness of the covering layer is more or less equal to the depth of the initial step section.

4.7 Discussion and perspectives

Out-diffusion problem

Studying the formation of periodically poled domains in $LiNbO_3$ (PPLN) in collaboration with Vladimir Shur from the Ural Federal University in Ekaterinburg, we defined another problem, which can occur in proton exchanged waveguides. It was found that out-diffusion of LiO_2 from the surface of $LiNbO_3$ can take place in our waveguides.

Therefore, I will now discuss the problem of out-diffusion of LiO_2. As it was mentioned in section 1.3, the out-diffusion can be used for waveguide fabrication as the modification of the stoichiometry of the $LiNbO_3$ leads to an index change. Initially, the conditions used for this process were high vacuum and a temperature up to 800°C. However the out-diffusion of LiO_2 and O_2 can be observed without vacuum such as during Ti-indiffusion, or at much lower temperatures such as during the annealing of APE waveguides which is carried out in the range between 300°C and 400°C. Here the out-diffusion is undesired

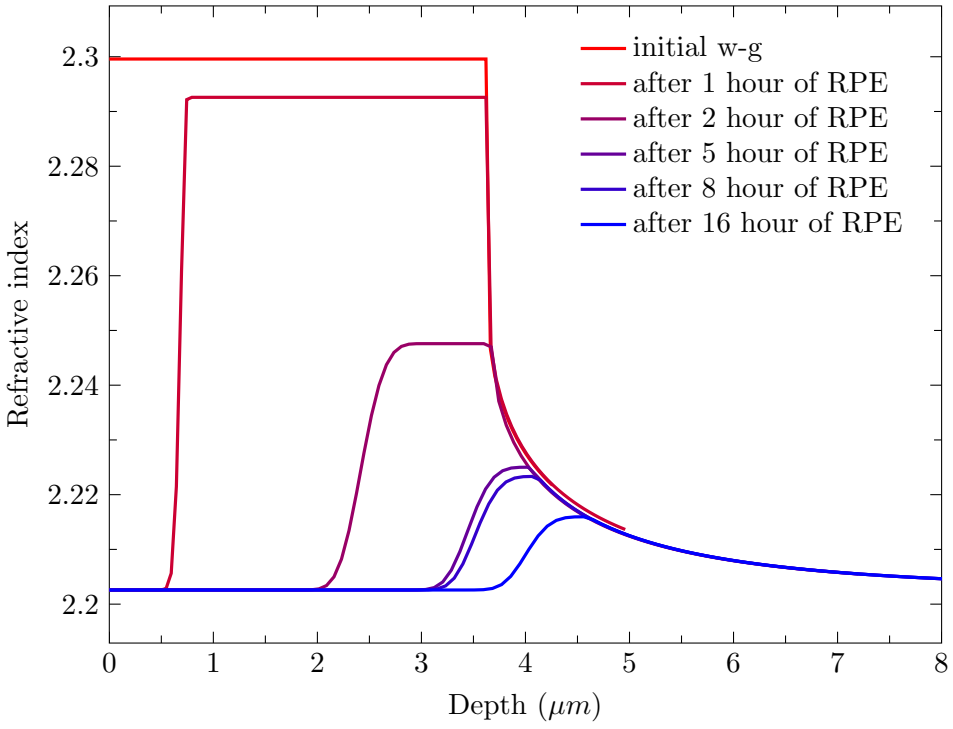

FIGURE 4.26: Index profiles of the buried waveguides obtained after 1, 2, 5, 8 and 16 hours of RPE in a melt of KNO_3:$NaNO_3$:$LiNO_3$ with a proportion ratio 1:1:0.1 respectively and at the temperature of 300°C.

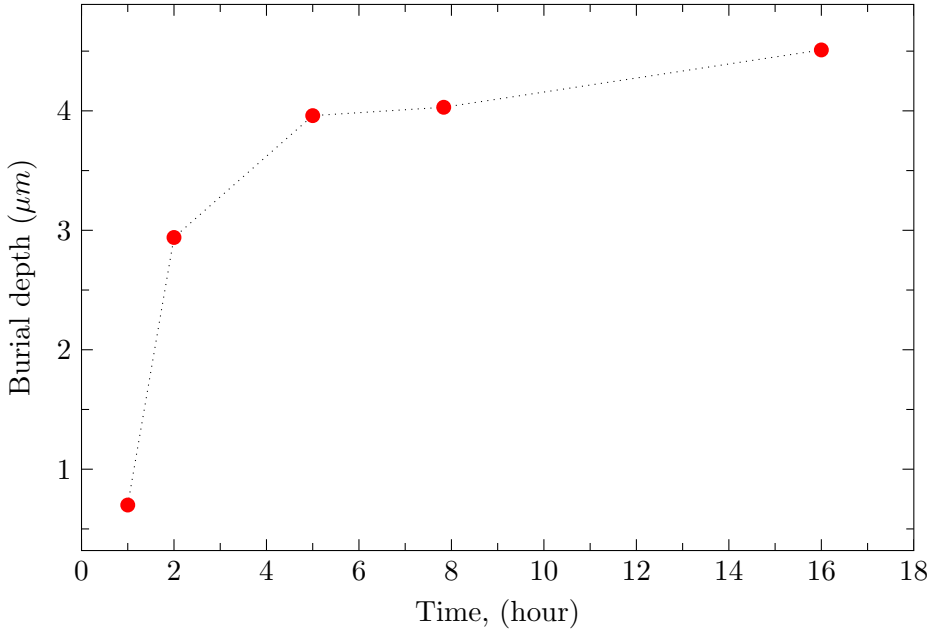

FIGURE 4.27: Depth of the reconstructed surface in funtion of RPE duration. RPE was carried out in a melt of KNO_3:$NaNO_3$:$LiNO_3$ with a proportion ratio 1:1:0.1 respectively and at the temperature of 300°C. The initial waveguide was fabricated with $\rho_{LB} = 2\%$ for 3 days at $T = 300$°C.

because it creates a waveguiding layer at the surface (in other words a planar waveguide) favoring the coupling between the channel waveguides. For this reason, the Ti-indiffusion

and the annealing of proton exchanged waveguides are usually carried out in oxygen-rich atmospheres in order to prevent any out-diffusion to take place.

However, there is no information concerning the out-diffusion effect during the proton exchanged process itself. In the past, when working on the choice of the best material to be used for the masks necessary for the realization of channel waveguides, our team in Nice observed some out-diffusion taking place during the SPE process. It was mainly observed using metallic masks such as Ti, and therefore SiO_2 was chosen. The group did not pay attention to this phenomenon until very recently in the frame of the study of the influence of the HISoPE process on the E-field poling mechanisms, which is carried out in collaboration with Prof. V. Shur as a part of the PhD work of Michael Dolbilov and Maxim Neradovskiy.

The observed results indicate that during the HISoPE process, the conductivity of the crystal is seriously modified, which can be explained by out-diffusion. Another characteristic of out-diffused layers is that they present a specific brown coloration associated with the presence of metallic Nb ions in the reduced layer. As the layers are thin, the color may be difficult to observe. Comparing my samples with a virgin $LiNbO_3$ substrate, I have been able to observe this coloration as shown in figure 4.28.

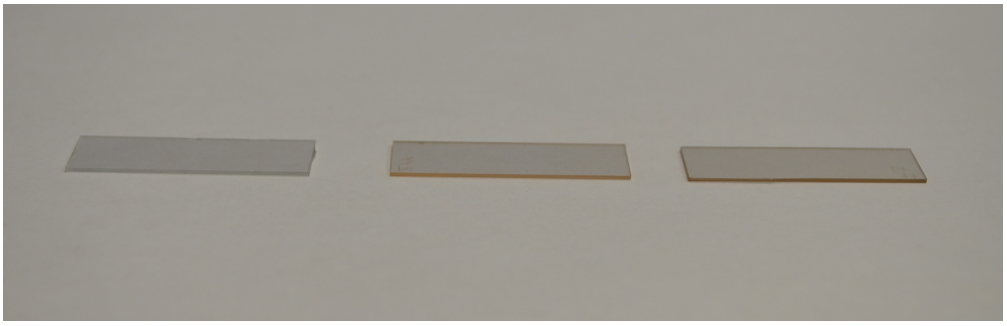

FIGURE 4.28: The coloration of the waveguides fabricated with the same concentration of LB but different exchange time. The samples on the photo are(from left to right): pure $LiNbO_3$, sample exchanged in 2.4% melt at 300°C for 24 hours, sample exchanged in the same melt and temperature for 48 hours.

The HISoPE waveguides were prepared using 2.4% LB in the melt at a temperature of 300°C. But the duration of the exchange was different: 24 and 48 hours. So one can see the difference in colors. The sample fabricated for 48 hours has the most intense brown tint.

Observing some other existing samples, it was verified that the coloration intensity mainly depends on the proton exchange duration but not on the exchange ratio, nor the thickness of the exchanged layer. This can indicate that the proton exchange is not the only process that can occur during waveguide fabrication. Moreover, the out-diffusion, which depends on the duration of the exchange, affects not only HISoPE waveguides.

Indeed, SPE waveguides also present a light brown coloration. Therefore, a detailed study of this phenomenon should be undertaken to determine its origin, its extension, its influence on the propagation, on the nonlinear interactions, etc., and see whether it can explain some strange behavior we have observed and how it can be cured, avoided or controlled.

Minimizing the deformations

The most important problem with HISoPE channel waveguides on Z-cut $LiNbO_3$ are losses. The main reason for that lies in the crystalline deformations induced by the proton exchange.

In order to minimize the strains at the interface between the waveguide and the substrate, I can propose two ideas.

The first proposition consists in fabricating the channel waveguides in a two-step process, consisting in a planar HISoPE process followed by a RPE process trough a mask. In this case, the mask should be made of SiO_2 stripes which will protect the area where a channel waveguide must be realized, the RPE process reconstructing the substrate all around the protected regions.

The first attempt to fabricate channel waveguides using such a combination of techniques was unsuccessful. It was found that the initial planar waveguide was not completely erased. One should use a longer RPE process, or change the composition of the RPE melt to make it faster and adjust the width of the stripes to take into account the lateral extension of the RPE process.

Another proposition is the same as for X-cut waveguides (see section 3.6) and consists in realizing the waveguides by double proton exchange. This approach should minimize the losses due to the hybrid nature of the propagating modes.

Conclusions

The HISoPE technique applied to Z-cut surface $LiNbO_3$ is more complicated than for X-cut. The presence of a high loss transition layer can be reduced in planar waveguides by reducing the percentage of lithium benzoate in the melt. But reducing this concentration increases the proton concentration and therefore the strains in the waveguiding layer. This becomes critical in channel waveguides, where the crystalline modifications of the waveguiding layer lead to the hybrid nature of the propagating modes and, thus, to high losses.

The reflected SHG profiles tend to show that the nonlinear coefficient is not affected, at least much less than in the case of PE waveguides. Nevertheless, the exact shape of the profile remains to be explained. Confocal linear and nonlinear microscopy will be used to determine with a great precision the exact linear and nonlinear profiles.

However, on the other hand, the results obtained by our colleagues in Russia, indicate that the HISoPE waveguides show a reduction of the electro-optical coefficients comparable to that experienced by PE waveguides. Therefore HISoPE waveguides still appear as a very interesting approach for nonlinear application, but one has to solve the losses issue.

Note that the evaluation of the electro-optical coefficient is based on the absorption properties of the proton exchanged waveguides in the UV region.[126] But the coloration of the outdiffused samples indicates that they can absorb the light and disturb the calculated result. Therefore, a precise measurement of the nonlinear coefficients in HISoPE waveguides remains to be performed.

Nevertheless, the HISoPE technique in combination with RPE process allowed fabricating nonlinear waveguides showing very promising results. A conversion efficiency of $160\%\,\mathrm{W}^{-1}\mathrm{cm}^{-2}$ has been obtained, and there are serious reasons to think that this number can be improved by a further development of the technique and get closer to the theoretical value of $300\%\,\mathrm{W}^{-1}\mathrm{cm}^{-2}$.[36,37]

This improvement mainly relies on a better control of the speed of the RPE process in the different proton exchanged layers in order to avoid fabricating directional couplers instead of channel waveguides.

Finally, we can conclude that the HISoPE technique needs further development. The fabrication of Nonlinear Quantum Wires in $LiNbO_3$ is not yet solved and during this work we may have raised more questions than we brought answers.

General conclusions

This work started with a great enthusiasm to finish a long battle to fabricate waveguides with high optical confinement and preserved nonlinear properties in $LiNbO_3$. Usually one had to make a compromise between them, and most often, the choice was to sacrifice the confinement in favor of the nonlinearities.

We proposed, developed and studied a new method of waveguide fabrication, which aimed to solve this problem. This technique, called HISoPE, allows fabricating waveguides with a maximal index change $dn_e = 0.1$. The study of the nonlinearities showed that the nonlinear properties of these waveguides are not destroyed. Interesting results have been obtained with planar waveguides, but it remains several issues with channel waveguides, the main of these being the propagation losses.

Working with X-cut wafers of $LiNbO_3$, we tried to realize a highly efficient electro-optic intensity modulator combining photonic crystals with HISoPE waveguides in the framework of the ANR phoXcry project. The losses of the HISoPE channel waveguides realized on X-cut wafers are around 1.7 dB/cm. This value is not very good but could be acceptable for very short devices. Unfortunately, the nanostructurated HISoPE waveguides exhibit very high losses and no optical band gap. This combination did not succeed to demonstrate a modulator.

The fabricated HISoPE waveguides showed propagation losses that mainly come from the hybrid nature of the modes induced by the strains in the guiding layer. Further developments, using a combination of several exchanges, are in progress to try to reduce these losses.

On Z-cut wafers, the results are different since already planar HISoPE waveguides exhibit an unusual behavior. In multimode waveguides, the modes with intermediate effective indices present high propagation losses, while the fundamental mode and the low index modes are propagating well. This problem can be solved by increasing the acidity of the bath used for the exchange. We then succeeded in producing planar HISoPE waveguides with low losses. In the X-rays spectra, this modification reduces the signal

corresponding to an inhomogeneous transition layer, which appears between the substrate peak and the exchanged layer peak. We therefore concluded that this layer, lying in the middle of the guide, was responsible for the losses and choose to use a more acidic bath. This choice turned to be problematic when we fabricated channel waveguides. Indeed, using a more acidic bath, we obtained waveguides with a higher substitution ratio and therefore higher strain, and we observed hybrid modes in the channels, which, for symmetry reasons, were not expected. The best waveguides we fabricated exhibit propagation losses $\geq 5\,\mathrm{dB/cm}$ and are even worse than for X-cut waveguides, where hybrid modes were expected. Several options exists to reduce the lateral stresses responsible for the hybrid nature of the mode, but I had not enough time to implement them. For this reason no nonlinear device was fabricated on PPLN crystal.

But HISoPE on Z-cut wafers was successfully used in combination with RPE technique in order to fabricate buried waveguides in PPLN. As the RPE conditions were not sufficiently optimized, the first waveguides we fabricated have several problems such as losses around $2\,\mathrm{dB/cm}$ and a directional coupler configuration. Taking these defects into account, it was possible to show that these waveguides have a conversion efficiency of $160\%\,\mathrm{W^{-1}cm^{-2}}$, which is equal to the best value reported to date, and allows to hope that further improvement of the combination would allow reaching the $300\%\,\mathrm{W^{-1}cm^{-2}}$ predicted by the theory.

Finally, the study of the compatibility of the HISoPE process with the E-field polling revealed that depending on the fabrication conditions, more or less out-diffusion can be superimposed with the proton exchange. This opens a completely new way of explaining some of the observed results, and new perspectives to improve the quality of the fabricated devices, but as this was discovered at the very end of this PhD thesis work, it will be studied in a future work.

Appendix A

Characterization of the index profile of waveguides

A.1 M-lines technique

Prism coupling technique, or m-lines, is a simple non-destructive and efficient method, which allows an accurate measurement of the spectrum of propagating modes from which the refractive index profile of the layer can be determined.[130–134] Usually, this method is used to characterize slab waveguides but it can be adapted to channel waveguides. In case of buried waveguides the coupling of the light into the waveguide by the tunnel effect becomes less efficient and cannot be used when the waveguide is deeply embedded.

During this research work, a two prisms set-up was used with a 10 mW He-Ne laser working at $\lambda = 633$ nm. One prism was used to couple light into the waveguide and another to couple it out (figure A.1). The sample is pressed against the base of the prisms. An incident beam for certain angles called resonance angles can be coupled into the waveguide by tunnel effect. The out-coupled pattern of the transmitted beam is called *bright m-lines*.

The coupling efficiency mainly depends on the air gap thickness, as well as the incident beam profile and incident beam section at the base of the prism.[103]

A goniometer is used to measure the angle θ between coupled out light beams and the normal to the surface of the prism with a precision around 10^{-3} degrees (figure A.4). If one knows the refractive indices of both the prism and the substrate in which the waveguide was fabricated, it is sufficient to calculate the effective indices using the following equation:[30]

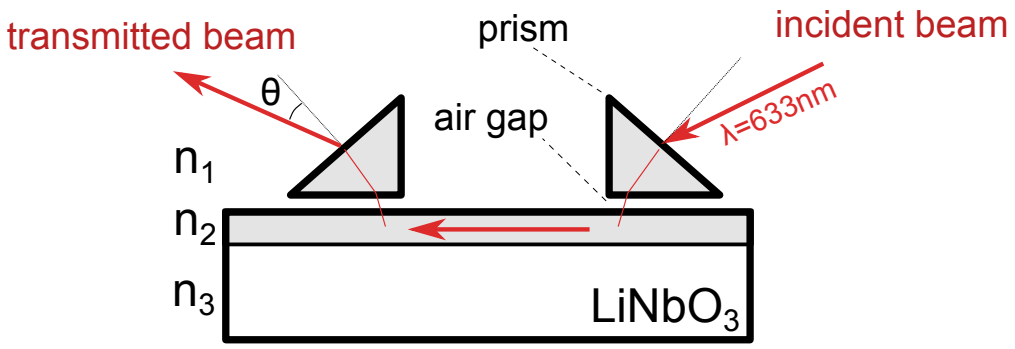

FIGURE A.1: Schematic principle of the m-line characterization. The indices n_1, n_2 and n_3 are those of air, the waveguide and the substrate, respectively.

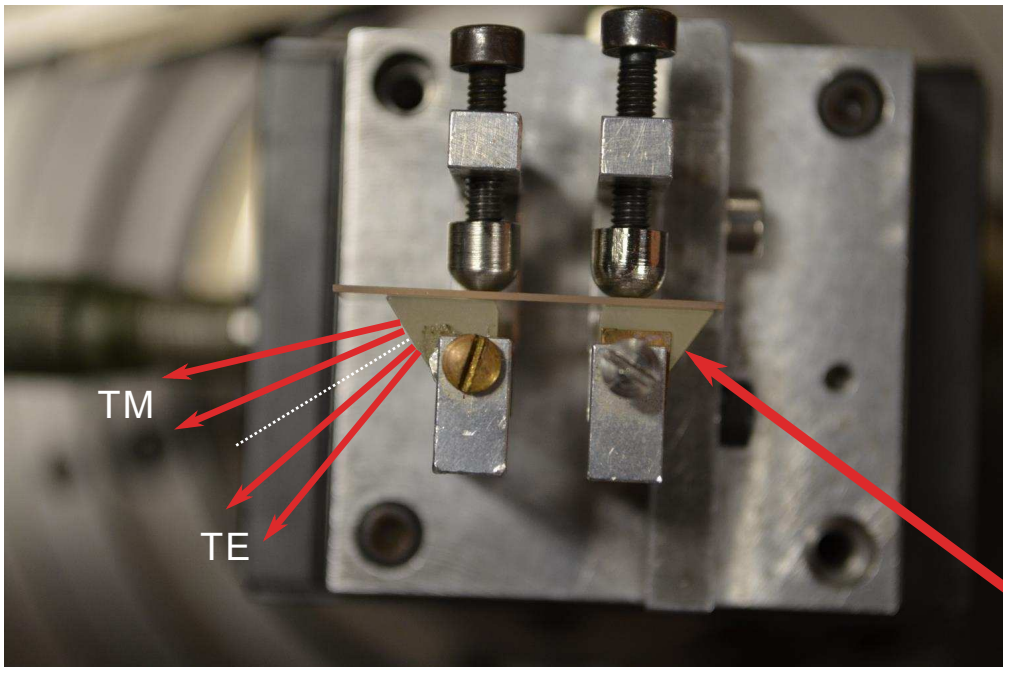

FIGURE A.2: Prisms used to couple the light in and out. The birefringence of the prisms results in different angles for TE and TM polarized light coupled out of a waveguide.

$$N_{eff} = n_p \sin\left(\theta_p \arctan\left(\frac{\sin(\theta)}{n_p\sqrt{1-(\sin(\theta)/n_p}}\right)\right), \tag{A.1}$$

where θ is the measured angle for the m-line, θ_p is the angle of the prism, which is equal to 55.032° for our set-up, and n_p corresponds to the refractive index of the prism. The prisms are birefringent with $n_o = 2.581$ and $n_e = 2.8618$, therefore the angles of the transmitted beams are different for TE and TM polarizations, even if the value of the effective index of the propagating mode is the same.

In our experimental set-up the values of N_{eff} were calculated automatically by appropriate software in order to save time.

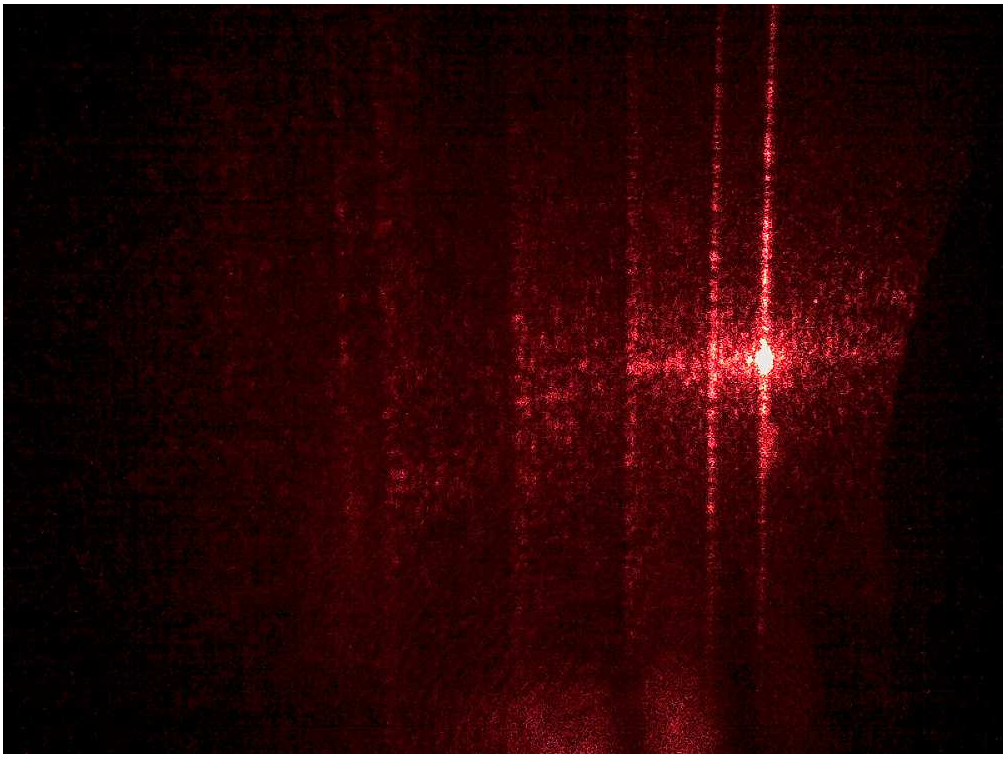

FIGURE A.3: Example of the m-lines result for a given planar waveguide.

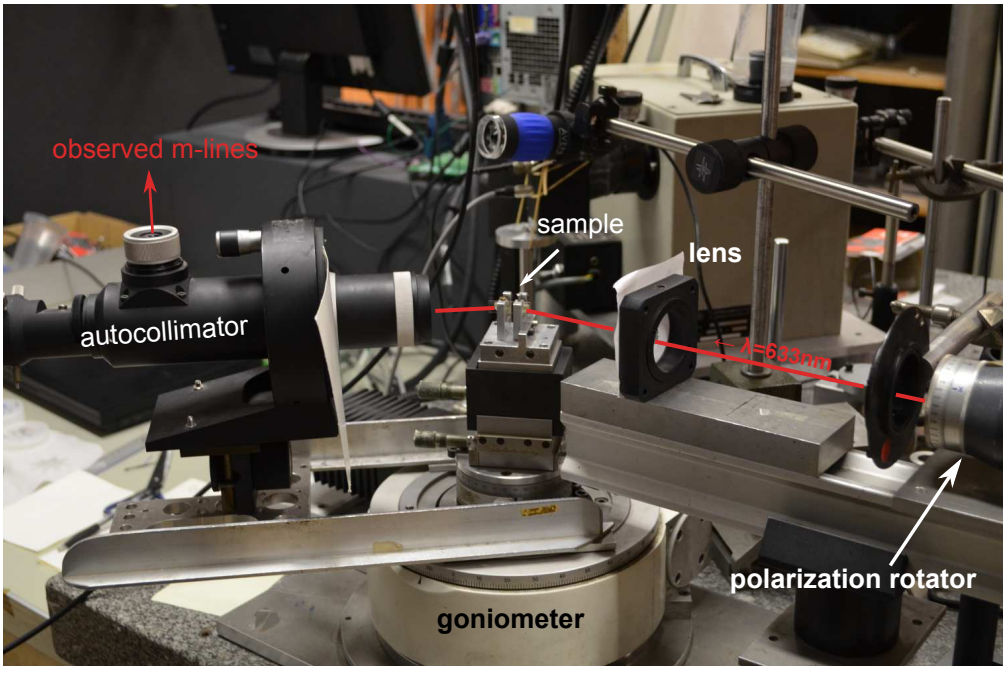

FIGURE A.4: The experimental set-up used for m-lines characterization.

By varying the distance between the two prisms, this set-up permits to observe light propagation in the waveguide and, therefore, to evaluate its optical quality. Nevertheless it does not allow precise measurement of the propagation losses, as contamination of the surface can dramatically affect the coupling efficiency.

Another important characteristics of the waveguide can be deduced from a careful analysis of the m-lines pattern. A thin light line with a bright spot in the center means that the propagating mode has practically no losses. Relatively broad and thick m-lines indicate high losses. Light diffusion also facilitates the intermodal coupling, and, as a result, several m-lines can be observed at the same time while one mode is excited.

In lossy waveguides, one can observe a light trace along the propagation direction, which attenuates quickly. Such behavior indicates losses on the order of $\geq 30\,\mathrm{dB/cm}$ (figure A.5(a)). Though qualitatively, the m-lines technique is very useful and can immediately reveal optical quality problems of the waveguides just after a fabrication process (figure A.5(c)).

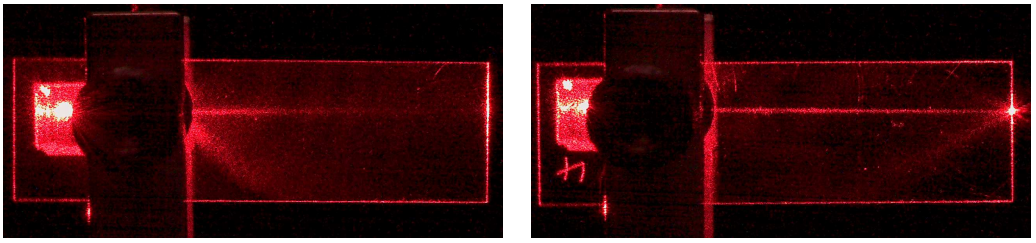

(a) Sample with high optical losses ($> 30\,\mathrm{dB/cm}$)

(b) Moderate losses ($< 5\,\mathrm{dB/cm}$)

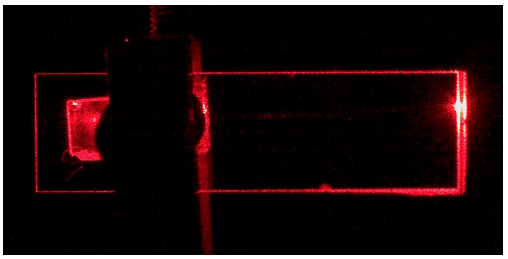

(c) A sample with low propagation losses

FIGURE A.5: Observation of light propagation in different planar proton exchanged waveguides.

M-lines of channel waveguides

In the case of the channel waveguides, it is difficult to couple a laser beam selectively in a certain waveguide. Therefore, end-fire coupling is used. The incident light beam is focused onto a polished cross-section of the waveguide (figure A.6). For all the rest the characterization steps are almost the same. However, the m-lines of channel waveguides

have a more complex image due to laterally confined modes: these modes give the 'interrupted' lines.

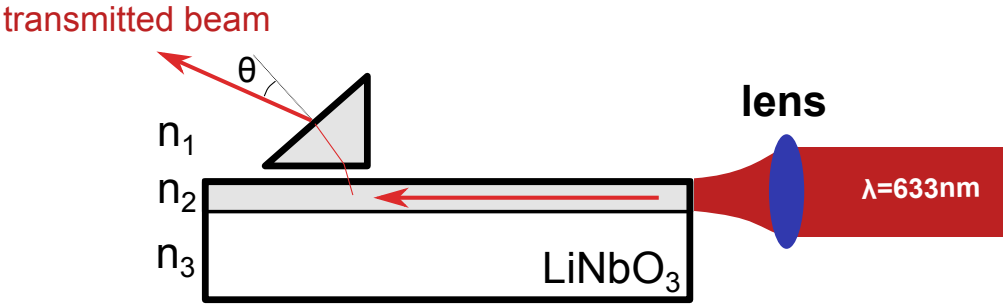

FIGURE A.6: Schematics of the m-lines method for characterizing channel waveguides.

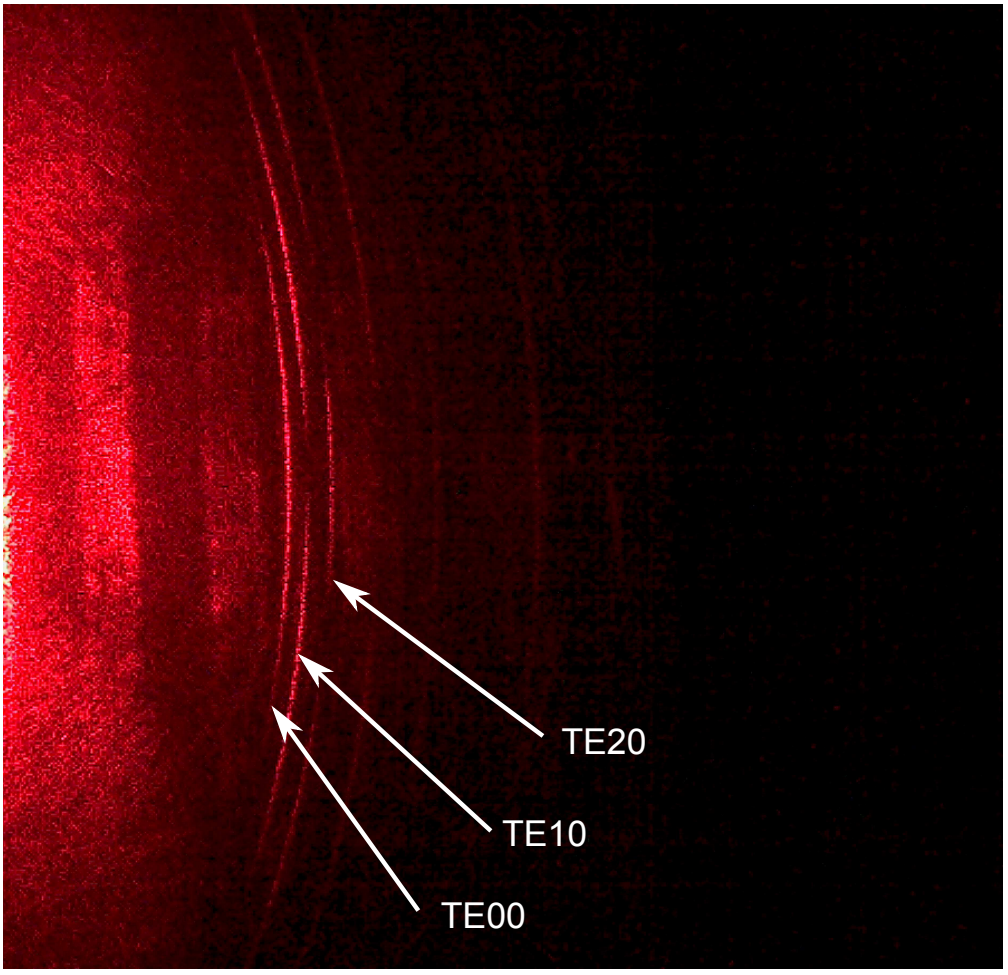

FIGURE A.7: Example of m-lines result for propagating modes confined in the lateral direction in a channel waveguide realized on X-cut $LiNbO_3$.

A.2 Index profile reconstruction

Knowing the values of N_{eff} for the different modes, it is possible to reconstruct a refractive index profile of the waveguide by applying the Inverse Wentzel-Kramers-Brillouin

(IWKB) numerical method.[135]

The inverse WKB method is based on certain approximations that each point is connected to its turning point by piecewise linear lines. This leads to some errors especially for high order modes.

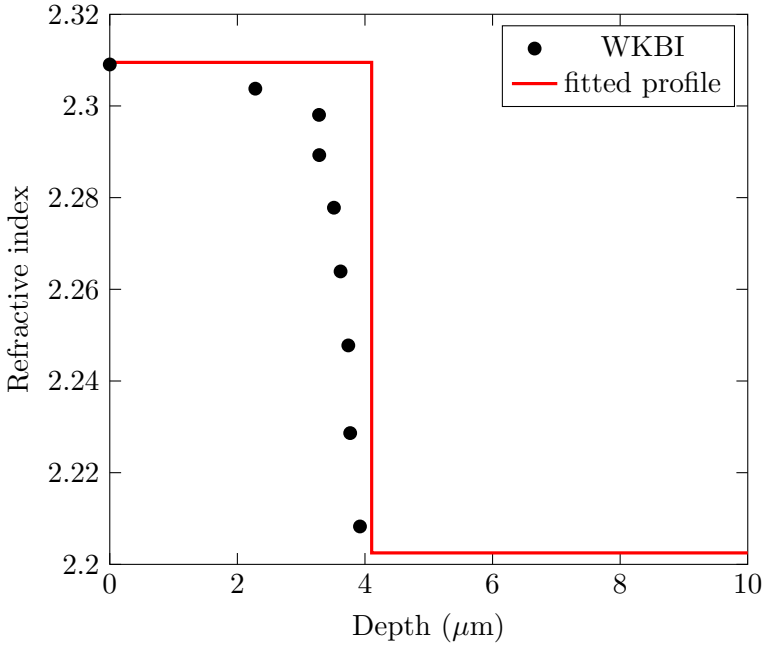

FIGURE A.8: Calculated index profile of the PE waveguide fabricated in pure benzoic acid at $T = 350°C$ during 30 minutes.

Another important point is that the approximation decreases in accuracy when abrupt changes occur in less than an optical wavelength. But, likewise, changes of this size are averaged out in their effect in determining the characteristics of the guided mode. For this reason, IWKB is not suitable for calculating step profiles as it tries to smooth the corner of the step (see an example in figure A.8).

For this reason, there is another approach for the calculation of the index profile of the waveguide. If one knows the shape of the waveguide in advance it is possible to fit the profile to the measured effective indices.[136–140] In case of PE and HISoPE waveguides this method was found to be more precise as it has no problem with the step profile shape.

Appendix B

Propagation losses measurements in waveguides

Using the m-lines technique, it is possible to estimate the optical quality and sometimes approximate propagation losses. However, more accurate losses measurement have to be carried out.

Generally speaking, total optical loss measurements are made by taking the logarithmic ratio of the input power P_{in} to the output power P_{out}:

$$\alpha = 10 \cdot log_{10}\left(\frac{P_{in}}{P_{out}}\right). \tag{B.1}$$

But such direct measurement is always problematic as one must take into account losses coming from scattering, mode mismatch, and reflection at the sample end facets. So another measurement technique is necessary.

The alternative characterization method is based on a Fabry-Perot cavity between two well polished waveguide extremities.[141] The waveguides in this case behave like a resonant cavity if their end facets are parallel to each other and perpendicular to the channel waveguides. The modes in these waveguides propagate in both directions and interfere in accordance with their relative phases. The transmitted intensity I_T is given by the following formula:[142]

$$I_T = \frac{T^2 \exp(-\alpha L)}{(1-\tilde{R})^2 + 4\tilde{R}\sin^2(\phi/2)} I_0 \eta, \tag{B.2}$$

where I_0 is the laser beam intensity in front of the waveguide, η the coupling efficiency to the waveguide mode, T the end facet mode transmittivity, and $\phi = 2\rho L$ the internal phase difference with the propagation constant β of the investigated mode in a sample

of length L. Here $\tilde{R}$ is the loss-reflection factor:

$$\tilde{R} = R\exp(-\alpha L), \tag{B.3}$$

The attenuation coefficient α can be expressed from previous equation B.3 as:

$$\alpha = \frac{4.34}{L}\left(\ln R - \ln \tilde{R}\right), \tag{B.4}$$

where α is given in dB/cm. The resonance conditions can be changed by heating the characterized sample modifying the cavity length or by tuning the laser wavelength. Then we can determine the contrast C of the Fabry-Perot resonances from the measured transmitted intensity:

$$C = \frac{I_{max} - I_{min}}{I_{max} + I_{min}}, \tag{B.5}$$

where I_{max} and I_{min} are the maximum and the minimum intensities, respectively. The contrast does not depend on I_0 and η (equation B.1), so

$$C = \frac{2\tilde{R}}{1 + \tilde{R}^2}, \tag{B.6}$$

and, therefore

$$\tilde{R} = \frac{1}{C}\left(1 - \sqrt{1 - C^2}\right). \tag{B.7}$$

On the other hand, the Fresnel reflection coefficient R can be approximated[143] to

$$R = \left(\frac{n_{eff} - 1}{n_{eff} + 1}\right)^2, \tag{B.8}$$

where $n_{eff} = \beta/k_0$ and $k_0 = 2\pi/\lambda$. Now, knowing R and simplifying the endface reflectivity to $\tilde{R} \sim C/2$ for small values of the contrast, we can use equation B.4 for measurement of the propagation losses.

Unfortunately, this method is valid only for characterizing low-loss optical waveguides as increasing losses reduce the contrast drastically.[142]

The Fabry-Perot cavity method is good and accurate for low-loss waveguides (≤ 1 dB/cm). But with higher losses, the contrast becomes small and the noise in the signal increases significantly the error obtained on the measured contrast.

Appendix C

Surface SHG probing technique

Scanning SHG microscopy technique is very useful for probing the nonlinear properties of a given nonlinear media.[144–146]

In case of proton exchanged waveguides, the reflected SHG signal permits to compare the nonlinear coefficient $\chi^{(2)}$ of the slab or channel waveguides fabricated on lithium niobate with $\chi^{(2)}$ of the substrate.[147–150] We used rather simple set-up, which allows to scan only the vertical position. Therefore we used only planar waveguides for this characterization. A schematic representation of the experimental set-up is described in figure C.1.

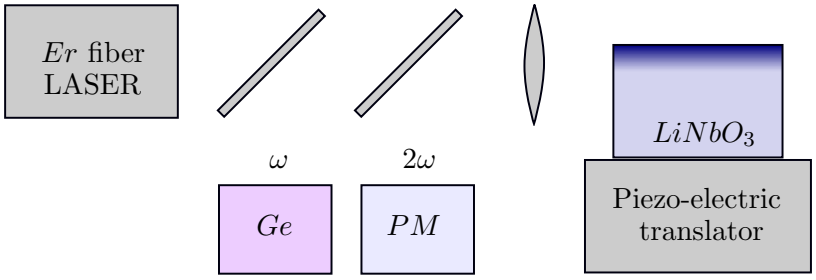

FIGURE C.1: Reflection SHG measurement set-up

A laser beam ($\lambda = 1.55\,\mu$m) out of a femtosecond erbium-doped fiber laser is focused on a well polished end facet of a $LiNbO_3$ sample using a lens to maximize the incident energy density in both time and space. The sample is placed on a piezoelectric translational support which can control a position of the sample. Then, two reflected signals at ω and 2ω are separated by a dichroic mirror and registered at the same time while moving the sample in the vertical direction. By scanning the end facet of the sample, we can plot the intensity profiles of the reflected ω and 2ω signals and compare SHG generated in the waveguide and in the substrate where the d_{33} was not changed by the proton exchange.

In figure C.2, we have the resulting profile of a slab waveguide fabricated in pure BA during 30 minutes at temperature 350°C. While the reflected fundamental light at ω helps to define the surface position, the index profile gives an idea about a depth of the sample waveguide. Contrary to I_ω the intensity $I_{2\omega}$ is very reduced in the waveguide depth. Thus we can identify an important degradation of the nonlinear coefficient inside the waveguide.

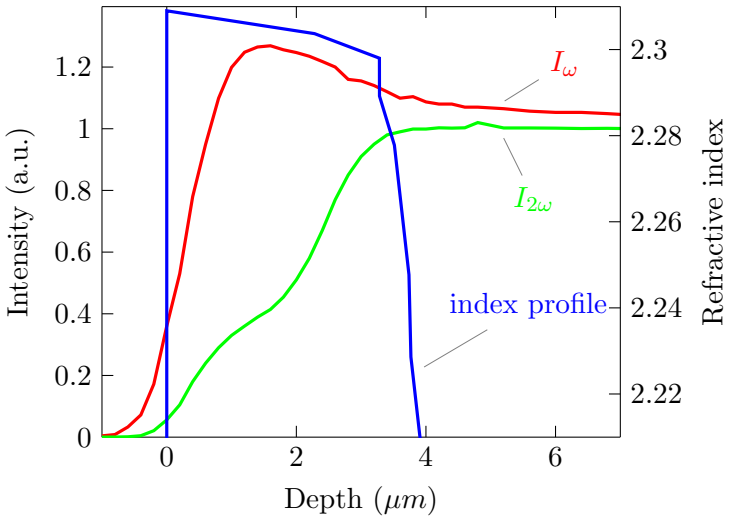

FIGURE C.2: In-depth SHG profiling of the plannar waveguide fabricated in pure benzoic acid. Refractive index calculated by IWKB method.

List of abbreviations

APE	—	Annealed Proton Exchange
BA	—	Benzoic Acid
EO	—	Electro-Optic
FIB	—	Focused Ion Beam
HISoPE	—	High Index Soft Proton Exchange
IO	—	Integrated Optics
IR	—	Infrared
LB	—	Lithium Benzoate
NL	—	Nonlinear
PC	—	Photonic Crystal
PE	—	Proton Exchange
PPLN	—	Periodically Poled Lithium Niobate
QPM	—	Quasi-Phase Matching
RBS	—	Rutherford Backscattering Spectrometry
RIE	—	Reactive-Ion Etching
RPE	—	Reverse Proton Exchange
SEM	—	Scanning Electron Microscopy
SHG	—	Second Harmonic Generation
SPDC	—	Spontaneous Parametric Down Conversion
SPE	—	Soft Proton Exchange
TE	—	Transverse Electric
TM	—	Transverse Magnetic
UV	—	Ultraviolet
VPE	—	Vapor-phase Proton Exchange
XRD	—	X-Ray Diffraction

Author's references

1. O. Stepanenko, E. Quillier, I. Krasnokutska, P. Baldi, and M. De Micheli. Nonlinear effects in lithium niobate proton exchanged embedded waveguides. In *Advanced Solid-State Lasers Congress*, paper AM4A.35, 2013.

2. O. Stepanenko, E. Quillier, I. Krasnokutska, P. Baldi, and M. De Micheli. Génération de second harmonique dans des guides enterrés sur niobate de lithium. In *Optique Paris 2013*, Paris, France, 2013.

3. O. Stepanenko, E. Quillier, I. Krasnokutska, P. Baldi, and M. De Micheli. Génération de second harmonique dans des guides enterrés sur niobate de lithium. In *Journées Nationales des Cristaux pour l'Optique*, Cherbourg, France, 2013.

4. O. Stepanenko, E. Quillier, H. Tronche, P. Baldi, P. Aschieri, S. Benchabane, and M. De Micheli. Towards nonlinear photonic wires in z-cut $LiNbO_3$. In *Laser Optics 2012*, Saint-Petersbourg, Russian Federation, 2012.

5. O. Stepanenko, E. Quillier, H. Tronche, P. Baldi, P. Aschieri, and M. De Micheli. Quantum wires in lithium niobate: first realizations and characterizations. In *9th International Conference on Physics of Advanced Materials*, Iasi, Romania, 2012.

6. M. De Micheli, O. Stepanenko, E. Quillier, H. Tronche, P. Baldi, P. Aschieri, and S. Benchabane. Towards proton exchanged photonic wires in $LiNbO_3$. In *Advances in Optical Materials (AIOM)*, paper IF1A.6, 2012.

7. O. Stepanenko, E. Quillier, H. Tronche, P. Baldi, P. Aschieri, S. Benchabane, J. Bourderionnet, and M. De Micheli. Modes hybrides dans les fils quantiques réalisés sur niobate de lithium en coupe X. In *Journées Nationales d'Optique Guidée*, Lyon, France, 2012.

8. O. Stepanenko, E. Quillier, H. Tronche, P. Baldi, P. Aschieri, S. Benchabane, and M. De Micheli. Premiers pas vers la réalisation de fils quantiques sur $LiNbO_3$. In *Journées Nationales d'Optique Guidée*, Marseille, France, 2011.

Bibliography

[1] M. Lawrence. Lithium niobate integrated optics. *Reports on Progress in Physics*, 56(3):363, 1993.

[2] M. N. Armenise. Fabrication techniques of lithium niobate waveguides. *Optoelectronics, IEE Proceedings J*, 135(2):85–91, 1988.

[3] R. L. Holman. The optical properties and processing of lithium niobate optical waveguides. In *Proceedins SPIE*, volume 0408, pages 14–20, 1983.

[4] S. Yin. Lithium niobate fibers and waveguides: fabrications and applications. *Proceedings of the IEEE*, 87(11):1962–1974, 1999.

[5] D. F. Clark, A. C. G. Nutt, K. K. Wong, P. J. R. Laybourn, and R. M. De La Rue. Characterization of proton-exchange slab optical waveguides in Z-cut $LiNbO_3$. *Journal of Applied Physics*, 54(11):6218–6220, 1983.

[6] W. K. Burns, P. H. Klein, E. J. West, and L. E. Plew. Ti diffusion in Ti:$LiNbO_3$ planar and channel optical waveguides. *Journal of Applied Physics*, 50(10):6175–6182, 1979.

[7] C. Canali, A. Carnera, P. Mazzoldi, and R. M. De La Rue. $LiNbO_3$ optical waveguide fabrication by Ti indiffusion and proton exchange: Process, performances and stability. In *Proceedings SPIE*, volume 0517, pages 119–127, 1985.

[8] J. L. Jackel, C. E. Rice, and J. J. Veselka. Proton exchange for high-index waveguides in $LiNbO_3$. *Applied Physics Letters*, 41(7):607–608, 1982.

[9] J. Jackel, A. M. Glass, G. E. Peterson, C. E. Rice, D. H. Olson, and J. J. Veselka. Damage-resistant $LiNbO_3$ waveguides. *Journal of Applied Physics*, 55(1):269–270, 1984.

[10] K.-K. Wong. Integrated optical waveguides and devices fabricated by proton exchange: A review. In *Proceedings SPIE*, volume 0993, pages 13–25, 1988.

[11] P. G. Suchoski, T. K. Findakly, and F. J. Leonberger. Stable low-loss proton-exchanged $LiNbO_3$ waveguide devices with no electro-optic degradation. *Optics Letters*, 13(11):1050–1052, 1988.

[12] R. A. Becker. Comparison of guided-wave interferometric modulators fabricated on $LiNbO_3$ via Ti indiffusion and proton exchange. *Applied Physics Letters*, 43 (2):131–133, 1983.

[13] M. Minakata, K. Kumagai, and S. Kawakami. Lattice constant changes and electrooptic effects in protonexchanged $LiNbO_3$ optical waveguides. *Applied Physics Letters*, 49(16):992–994, 1986.

[14] F. Laurell, M. G. Roelofs, and H. Hsiung. Loss of optical nonlinearity in proton-exchanged $LiNbO_3$ waveguides. *Applied Physics Letters*, 60(3):301–303, 1992.

[15] W.-Y. Hsu, C. S. Willand, V. Gopalan, and M. C. Gupta. Effect of proton exchange on the nonlinear optical properties of $LiNbO_3$ and $LiTaO_3$. *Applied Physics Letters*, 61(19):2263–2265, 1992.

[16] M. L. Bortz and M. M. Fejer. Annealed proton-exchanged $LiNbO_3$ waveguides. *Opt. Lett.*, 16(23):1844–1846, 1991.

[17] L. Chanvillard, P. Aschiéri, P. Baldi, D. B. Ostrowsky, M. de Micheli, L. Huang, and D. J. Bamford. Soft proton exchange on periodically poled $LiNbO_3$: A simple waveguide fabrication process for highly efficient nonlinear interactions. *Applied Physics Letters*, 76(9):1089–1091, 2000.

[18] D. Castaldini, P. Bassi, S. Tascu, P. Aschieri, M. P. De Micheli, and P. Baldi. Soft-proton-exchange tapers for low insertion-loss $LiNbO_3$ devices. *Lightwave Technology, Journal of*, 25(6):1588–1593, 2007.

[19] E. E. Robertson, R. W. Eason, Y. Yokoo, and P. J. Chandler. Photorefractive damage removal in annealed-proton-exchanged $LiNbO_3$ channel waveguides. *Applied Physics Letters*, 70(16):2094–2096, 1997.

[20] Y. Kondo and Y. Fujii. Photorefractive effect in proton-exchanged waveguiding layers formed on lithium niobate and lithium tantalate crystals. *Japanese Journal of Applied Physics*, 34(Part 2, No. 3A):L309–L311, 1995.

[21] E. Glavas, J. M. Cabrera, and P. D. Townsend. A comparison of optical damage in different types of $LiNbO_3$ waveguides. *Journal of Physics D: Applied Physics*, 22(5):611, 1989.

[22] J. L. Jackel and J. J. Johnson. Reverse exchange method for burying proton exchanged waveguides. *Electronics Letters*, 27(15):1360–1361, 1991.

[23] Yuri N. Korkishko, Vyacheslav A. Fedorov, S. V. Katin, and Andrey V. Kondrat'ev. Reverse proton exchange in $LiTaO_3$ and $LiNbO_3$ for buried optical waveguides. In *Proceeding SPIE*, volume 2401, pages 149–161, 1995.

[24] K. El Hadi, P. Baldi, M. P. De Micheli, D. B. Ostrowsky, Yu. N. Korkishko, V. A. Fedorov, and A. V. Kondrat'ev. Ordinary and extraordinary waveguides realized by reverse proton exchange on $LiTaO_3$. *Optics Communications*, 140(13):23 – 26, 1997.

[25] D. H. Tsou, M. H. Chou, P. Santhanaraghavan, Y. H. Chen, and Y. C. Huang. Structural and optical characterization for vapor-phase proton exchanged lithium niobate waveguides. *Materials Chemistry and Physics*, 78(2):474 – 479, 2003.

[26] J. Rams and J. M. Cabrera. Nonlinear optical efficient $LiNbO_3$ waveguides proton exchanged in benzoic acid vapor: Effect of the vapor pressure. *Journal of Applied Physics*, 85(3):1322–1328, 1999.

[27] J. Rams, F. Agullo-Rueda, and J. M. Cabrera. Structure of high index proton exchange $LiNbO_3$ waveguides with undegraded nonlinear optical coefficients. *Applied Physics Letters*, 71(23):3356–3358, 1997.

[28] P. J. Masalkar, M. Fujimura, T. Suhara, and H. Nishihara. Vapour phase proton-exchange: technique for waveguide fabrication in $LiNbO_3$. *Electronics Letters*, 33 (6):519–520, 1997.

[29] R. Osellame, R. Ramponi, M. Marangoni, and V. Russo. Waveguide fabrication in $LiTaO_3$ by vapour-phase proton-exchange. *Electronics Letters*, 36(5):431–433, 2000.

[30] L. Chanvillard. *Interactions parametriques guidees de grande efficacite : utilisation de l'échange protonique doux sur niobate de lithium inverse periodiquement.* PhD thesis, Université Nice Sophia Antipolis, 1999.

[31] M. Roussey, M.-P. Bernal, N. Courjal, and F.I. Baida. Experimental and theoretical characterization of a lithium niobate photonic crystal. *Applied Physics Letters*, 87(24):241101, 2005.

[32] H. Lu, F. I. Baida, G. Ulliac, N. Courjal, M. Collet, and M.-P. Bernal. Lithium niobate photonic crystal wire cavity: Realization of a compact electro-optically tunable filter. *Applied Physics Letters*, 101(15):151117, 2012.

[33] F. Chen. Photonic guiding structures in lithium niobate crystals produced by energetic ion beams. *Journal of Applied Physics*, 106(8):081101–081101–29, 2009.

[34] F. Schrempel, T. Gischkat, H. Hartung, T. Höche, E.-B. Kley, A. Tünnermann, and W. Wesch. Ultrathin membranes in x-cut lithium niobate. *Optics Letters*, 34 (9):1426–1428, 2009.

[35] N. Courjal, B. Guichardaz, G. Ulliac, J.-Y. Rauch, B. Sadani, H.-H. Lu, and M.-P. Bernal. High aspect ratio lithium niobate ridge waveguides fabricated by optical grade dicing. *Journal of Physics D: Applied Physics*, 44(30):305101, 2011.

[36] K. R. Parameswaran, R. K. Route, J. R. Kurz, R. V. Roussev, M. M. Fejer, and M. Fujimura. Highly efficient second-harmonic generation in buried waveguides formed by annealed and reverse proton exchange in periodically poled lithium niobate. *Optics Letters*, 27(3):179–181, 2002.

[37] K. Gallo, M. De Micheli, and P. Baldi. Parametric fluorescence in periodically poled $LiNbO_3$ buried waveguides. *Applied Physics Letters*, 80(24):4492–4494, 2002.

[38] R. A. Becker. Broad-band guided-wave electrooptic modulators. *Quantum Electronics, IEEE Journal of*, 20(7):723–727, 1984.

[39] G. Betts, L. M. Johnson, and III Cox, C. H. High-sensitivity lumped-element bandpass modulators in $LiNbO_3$. *Lightwave Technology, Journal of*, 7(12):2078–2083, 1989.

[40] W. K. Burns, A. B. Lee, and A. F. Milton. Active branching waveguide modulator. *Applied Physics Letters*, 29(12):790–792, 1976.

[41] P. S. Cross, R. A. Baumgartner, and B. H. Kolner. Microwave integrated optical modulator. *Applied Physics Letters*, 44(5):486–488, 1984.

[42] W. Sohler, H. Hu, R. Ricken, V. Quiring, C. Vannahme, H. Herrmann, D. Büchter, S. Reza, W. Grundkötter, S. Orlov, H. Suche, R. Nouroozi, and Y. Min. Integrated optical devices in lithium niobate. *Optics & Photonics News*, 19(1):24–31, 2008.

[43] K. Higuma, S. Oikawa, Y. Hashimoto, H. Nagata, and M. Izutsu. X-cut lithium niobate optical single-sideband modulator. *Electronics Letters*, 37(8):515–516, 2001.

[44] Y. A. Vlasov, M. O'Boyle, H. F. Hamann, and S. J. McNab. Active control of slow light on a chip with photonic crystal waveguides. *Nature*, 2005/11/30.

[45] F. Lacour, N. Courjal, M.-P. Bernal, A. Sabac, C. Bainier, and M. Spajer. Nanostructuring lithium niobate substrates by focused ion beam milling. *Optical Materials*, 27(8):1421 – 1425, 2005.

[46] L. E. Myers and W. R. Bosenberg. Periodically poled lithium niobate and quasi-phase-matched optical parametric oscillators. *Quantum Electronics, IEEE Journal of*, 33(10):1663–1672, 1997.

[47] D. H. Jundt, G. A. Magel, M. M. Fejer, and R. L. Byer. Periodically poled $LiNbO_3$ for high-efficiency second-harmonic generation. *Applied Physics Letters*, 59(21): 2657–2659, 1991.

[48] S. Tanzilli, W. Tittel, H. De Riedmatten, H. Zbinden, P. Baldi, M. DeMicheli, D.B. Ostrowsky, and N. Gisin. PPLN waveguide for quantum communication. *The European Physical Journal D - Atomic, Molecular, Optical and Plasma Physics*, 18(2):155–160, 2002. ISSN 1434-6060.

[49] K. Gallo, G. Assanto, K. R. Parameswaran, and M. M. Fejer. All-optical diode in a periodically poled lithium niobate waveguide. *Applied Physics Letters*, 79(3): 314–316, 2001.

[50] P. Gunter, J. P. Huignard, and P. Yeh. Photorefractive materials and their applications. *Applied Optics*, 28:3813, Sep 1989.

[51] K. Nassau, H. J. Levinstein, and G. M. Loiacono. Ferroelectric lithium niobate. 1. Growth, domain structure, dislocations and etching. *Journal of Physics and Chemistry of Solids*, 27(67):983 – 988, 1966.

[52] K. Nassau, H. J. Levinstein, and G. M. Loiacono. Ferroelectric lithium niobate. 2. Preparation of single domain crystals. *Journal of Physics and Chemistry of Solids*, 27(67):989 – 996, 1966.

[53] S. C. Abrahams, J. M. Reddy, and J. L. Bernstein. Ferroelectric lithium niobate. 3. Single crystal X-ray diffraction study at 24°C. *Journal of Physics and Chemistry of Solids*, 27(67):997 – 1012, 1966.

[54] S. C. Abrahams, W. C. Hamilton, and J. M. Reddy. Ferroelectric lithium niobate. 4. Single crystal neutron diffraction study at 24°C. *Journal of Physics and Chemistry of Solids*, 27(67):1013 – 1018, 1966.

[55] S. C. Abrahams, H. J. Levinstein, and J. M. Reddy. Ferroelectric lithium niobate. 5. Polycrystal X-ray diffraction study between 24°C and 1200°C. *Journal of Physics and Chemistry of Solids*, 27(67):1019 – 1026, 1966.

[56] L. Arizmendi. Photonic applications of lithium niobate crystals. *Physica Status Solidi (A)*, 201(2):253–283, 2004.

[57] S. C. Abrahams, E. Buehler, W. C. Hamilton, and S. J. Laplaca. Ferroelectric lithium tantalate. 3. Temperature dependence of the structure in the ferroelectric phase and the para-electric structure at 940°K. *Journal of Physics and Chemistry of Solids*, 34(3):521 – 532, 1973.

[58] R. S. Weis and T. K. Gaylord. Lithium niobate: Summary of physical properties and crystal structure. *Applied Physics A*, 37(4):191–203, 1985.

[59] E. Y. B. Pun, K. K. Loi, and P. S. Chung. Index profile of proton-exchanged waveguides in lithium niobate using cinnamic acid. *Electronics Letters*, 27(14): 1282–1283, 1991.

[60] J. T. Cargo, A. J. Filo, M. C. Hughes, V. C. Kannan, F. A. Stevie, J. A. Taylor, and R. J. Holmes. Characterization of sulfuric acid proton-exchanged lithium niobate. *Journal of Applied Physics*, 67(2):627–633, 1990.

[61] G. A. Bogert and D. T. Moser. Sulfuric acid proton exchanged channel waveguides fabricated in $LiNbO_3$. *Photonics Technology Letters, IEEE*, 2(9):632–633, 1990.

[62] E. Y.-B. Pun, K. L. Kwok, and S. C. Po. Proton-exchanged optical waveguides in Z-cut $LiNbO_3$ using phosphoric acid. *Lightwave Technology, Journal of*, 11(2): 277–284, 1993.

[63] Y.-S. Son, H.-J. Lee, Y.-K. Jhee, S.-Y. Shin, and B.-G. Kim. Fabrication of $LiNbO_3$ channel waveguides using water. *Photonics Technology Letters, IEEE*, 4 (5):457–459, 1992.

[64] E. Y.-B. Pun, S. A. Zhao, K. K. Loi, and P.S. Chung. Proton-exchanged $LiNbO_3$ optical waveguides using stearic acid. *Photonics Technology Letters, IEEE*, 3(11): 1006–1008, 1991.

[65] A. Loni, R. W. Keys, R. M. De La Rue, M. A. Foad, and J. M. Winfield. Optical characterisation of Z-cut proton-exchanged $LiNbO_3$ waveguides fabricated using orthophosphoric and pyrophosphoric acid. *Optoelectronics, IEE Proceedings J*, 136 (6):297–300, 1989.

[66] C. E. Rice and J. L. Jackel. Structural changes with composition and temperature in rhombohedral li1xhxnbo3. *Materials Research Bulletin*, 19(5):591 – 597, 1984.

[67] Yu N. Korkishko and V. A. Fedorov. Relationship between refractive indices and hydrogen concentration in proton exchanged $LiNbO_3$ waveguides. *Journal of Applied Physics*, 82(3):1010–1017, 1997.

[68] J. M. Zavada, H. C. Casey, C.-H. Chen, and A. Loni. Correlation of refractive index profiles with substitutional hydrogen concentrations in annealed proton-exchanged $LiNbO_3$ waveguides. *Applied Physics Letters*, 62(22):2769–2771, 1993.

[69] J. L. Jackel, C. E. Rice, and J. J. Veselka. Composition control in proton-exchanged $LiNbO_3$. *Electronics Letters*, 19(10):387–388, 1983.

[70] M. L. Bortz, S. J. Field, M. M. Fejer, D. W. Nam, R. G. Waarts, and D. F. Welch. Noncritical quasi-phase-matched second harmonic generation in an annealed proton-exchanged $LiNbO_3$ waveguide. *Quantum Electronics, IEEE Journal of*, 30(12):2953–2960, 1994.

[71] X. F. Cao, R. V. Ramaswamy, and R. Srivastava. Characterization of annealed proton exchanged $LiNbO_3$ waveguides for nonlinear frequency conversion. *Lightwave Technology, Journal of*, 10(9):1302–1313, 1992.

[72] A. Loni, G. Hay, R. M. De La Rue, and J. M. Winfield. Proton-exchanged $LiNbO_3$ waveguides: the effects of post-exchange annealing and buffered melts as determined by infrared spectroscopy, optical waveguide measurements, and hydrogen isotopic exchange reactions. *Lightwave Technology, Journal of*, 7(6):911–919, 1989.

[73] Y. N. Korkishko, V. A. Fedorov, and F. Laurell. The SHG-response of different phases in proton exchanged lithium niobate waveguides. *Selected Topics in Quantum Electronics, IEEE Journal of*, 6(1):132–142, 2000.

[74] K. El Hadi, M. Sundheimer, P. Aschieri, P. Baldi, M. P. De Micheli, D. B. Ostrowsky, and F. Laurell. Quasi-phase-matched parametric interactions in proton-exchanged lithium niobate waveguides. *Journal of the Optical Society of America B*, 14(11):3197–3203, 1997.

[75] Yu. N. Korkishko, V. A. Fedorov, E. A. Baranov, M. V. Proyaeva, T. V. Morozova, F. Caccavale, F. Segato, C. Sada, and S. M. Kostritskii. Characterization of α-phase soft proton-exchanged $LiNbO_3$ optical waveguides. *Journal of the Optical Society of America A*, 18(5):1186–1191, 2001.

[76] Yu. N. Korkishko, V. A. Fedorov, T. M. Morozova, F. Caccavale, F. Gonella, and F. Segato. Reverse proton exchange for buried waveguides in $LiNbO_3$. *Journal of the Optical Society of America A*, 15(7):1838–1842, 1998.

[77] J. Olivares and J. M. Cabrera. Guided modes with ordinary refractive index in proton exchanged $LiNbO_3$ waveguides. *Applied Physics Letters*, 62(20):2468–2470, 1993.

[78] I. P. Kaminow and J. R. Carruthers. Optical waveguiding layers in $LiNbO_3$ and $LiTaO_3$. *Applied Physics Letters*, 22(7):326–328, 1973.

[79] J. R. Carruthers, I. P. Kaminow, and L. W. Stulz. Diffusion kinetics and optical waveguiding properties of outdiffused layers in lithium niobate and lithium tantalate. *Applied Optics*, 13(10):2333–2342, 1974.

[80] C.-S. Lau, P.-K. Wei, C.-W. Su, and W.-S. Wang. Fabrication of strip loaded outdiffusion guides on lithium niobate substrate. *Microwave and Optical Technology Letters*, 5(7):309–313, 1992.

[81] R. V. Schmidt and I. P. Kaminow. Metal-diffused optical waveguides in $LiNbO_3$. *Applied Physics Letters*, 25(8):458–460, 1974.

[82] G. Griffiths and R. Esdaile. Analysis of titanium diffused planar optical waveguides in lithium niobate. *Quantum Electronics, IEEE Journal of*, 20(2):149–159, 1984.

[83] R. J. Holmes and D. M. Smyth. Titanium diffusion into $LiNbO_3$ as a function of stoichiometry. *Journal of Applied Physics*, 55(10):3531–3535, 1984.

[84] R. C. Alferness. Titanium-diffused lithium niobate waveguide devices. In Theodor Tamir, editor, *Guided-Wave Optoelectronics*, volume 26 of *Springer Series in Electronics and Photonics*, pages 145–210. Springer Berlin Heidelberg, 1988.

[85] M. Fukuma, J. Noda, and H. Iwasaki. Optical properties in titanium-diffused $LiNbO_3$ strip waveguides. *Journal of Applied Physics*, 49(7):3693–3698, 1978.

[86] G. L. Destefanis, J. P. Gailliard, E. L. Ligeon, S. Valette, B. W. Farmery, P. D. Townsend, and A. Perez. The formation of waveguides and modulators in $LiNbO_3$ by ion implantation. *Journal of Applied Physics*, 50(12):7898–7905, 1979.

[87] S. Mailis, C. Riziotis, I. T. Wellington, P. G. R. Smith, C. B. E. Gawith, and R. W. Eason. Direct ultraviolet writing of channel waveguides in congruent lithium niobate single crystals. *Optics Letters*, 28(16):1433–1435, 2003.

[88] J. E. Midwinter. Lithium niobate: Effects of composition on the refractive indices and optical second-harmonic generation. *Journal of Applied Physics*, 39(7):3033–3038, 1968.

[89] Van E. Wood, N. F. Hartman, A. E. Austin, and C. M. Verber. Stoichiometry dependence of lithium outdiffusion in $LiNbO_3$. *Journal of Applied Physics*, 52(2): 1118–1120, 1981.

[90] D. Delacourt, F. Armani, and M. Papuchon. Second-harmonic generation efficiency in periodically poled $LiNbO_3$ waveguides. *Quantum Electronics, IEEE Journal of*, 30(4):1090–1099, 1994.

[91] G. T. Reed and B. L. Weiss. Electro-optic effect in He^+-implanted optical waveguides in $LiNbO_3$. *Electronics Letters*, 23(8):424–425, 1987.

[92] M. De Micheli, J. Botineau, P. Sibillot, D. B. Ostrowsky, and Papuchon M. Fabrication and characterization of titanium indiffused proton exchanged (TIPE) waveguides in lithium niobate. *Optics Communications*, 42(2):101 – 103, 1982. ISSN 0030-4018.

[93] J. Heibei and E. Voges. Strip waveguides in $LiNbO_3$ fabricated by combined metal diffusion and ion implantation. *Quantum Electronics, IEEE Journal of*, 18 (5):820–825, 1982.

[94] G. R. Paz-Pujalt, D. D. Tuschel, G. Braunstein, Thomas Blanton, S. T. Lee, and L. M. Salter. Characterization of proton exchange lithium niobate waveguides. *Journal of Applied Physics*, 76(7):3981–3987, 1994.

[95] M. De Micheli, D. Ostrowsky, J. Barety, C. Canali, A. Carnera, G. Mazzi, and M. Papuchon. Crystalline and optical quality of proton exchanged waveguides. *Lightwave Technology, Journal of*, 4(7):743–745, 1986.

[96] C. E. Rice. The structure and properties of $Li_{1-x}H_xNbO_3$. *Journal of Solid State Chemistry*, 64(2):188 – 199, 1986.

[97] Y. N. Korkishko, Vyacheslav A. Fedorov, V. V. Nosikov, S. M. Kostritskii, and M. P. De Micheli. Phase diagram of $H_xLi_{1-x}NbO_3$ optical waveguides. In *Proceedins SPIE*, volume 2997, pages 188–200, 1997.

[98] Yu. N. Korkishko and V. A. Fedorov. Relationship between refractive indices and hydrogen concentration in proton exchanged $LiNbO_3$ waveguides. *Journal of Applied Physics*, 82(3):1010–1017, 1997.

[99] Yu. N. Korkishko, V. A. Fedorov, M. P. De Micheli, P. Baldi, K. El Hadi, and A. Leycuras. Relationships between structural and optical properties of proton-exchanged waveguides on Z-cut lithium niobate. *Appl. Opt.*, 35(36):7056–7060, 1996.

[100] Yu. N. Korkishko, V. A. Fedorov, and S. M. Kostritskii. Optical and x-ray characterization of $H_xLi_{1-x}NbO_3$ phases in proton-exchanged $LiNbO_3$ optical waveguides. *Journal of Applied Physics*, 84(5):2411–2419, 1998.

[101] Harry J. Levinson. *Principles of Lithography*, volume PM198. SPIE Press, 2011.

[102] K. Okamoto. *Fundamentals of Optical Waveguides*. Academic Press, 2006.

[103] A. Boudrioua. *Photonic Waveguides*. Wiley-ISTE, 2009.

[104] Robert W. Boyd. *Nonlinear Optics*. Academic Press, 2008.

[105] A. W. Warner, M. Onoe, and G. A. Coquin. Determination of elastic and piezoelectric constants for crystals in class (3m). *The Journal of the Acoustical Society of America*, 42(6):1223–1231, 1967.

[106] R. T. Smith and F. S. Welsh. Temperature dependence of the elastic, piezoelectric, and dielectric constants of lithium tantalate and lithium niobate. *Journal of Applied Physics*, 42(6):2219–2230, 1971.

[107] R. V. Damie. Elastic constants of lithium niobate. *Journal of Physics D: Applied Physics*, 25(7):1091, 1992.

[108] S. Chen. *Modes hybrides dans des guides realisés par échange protonique sur* $LiNbO_3$. PhD thesis, Université Nice Sophia Antipolis, 1992.

[109] A. Knoesen, T. K. Gaylord, and M. G. Moharam. Hybrid guided modes in uniaxial dielectric planar waveguides. *Lightwave Technology, Journal of*, 6(6):1083–1104, 1988.

[110] G. Tartarini, P. Bassi, S. Chen, M. P. De Micheli, and D. B. Ostrowsky. Calculation of hybrid modes in uniaxial planar optical waveguides: application to proton exchange lithium niobate waveguides. *Optics Communications*, 101(5):424–431, 1993.

[111] G. Tartarini, P. Bassi, P. Baldi, M. P. De Micheli, and D. B. Ostrowsky. Characteristics of hybrid modes in proton-exchanged lithium niobate waveguides. *Applied Optics*, 34(18):3441–3448, 1995.

[112] G. Tartarini, P. Bassi, P. Baldi, M. P. De Micheli, and D. B. Ostrowsky. Biaxial characteristics of planar proton exchanged lithium niobate waveguides. *Lightwave Technology, Journal of*, 15(5):821–826, 1997.

[113] S. Chen, P. Baldi, M. P. De Micheli, D. B. Ostrowsky, A. Leycuras, G. Tartarini, and P. Bassi. Loss mechanisms and hybrid modes in high-δn_e proton-exchanged planar waveguides. *Optics Letters*, 18(16):1314–1316, 1993.

[114] S. Chen, P. Baldi, M. P. De Micheli, D. B. Ostrowsky, A. Leycuras, G. Tartarini, and P. Bassi. Hybrid modes in proton exchanged waveguides realized in $LiNbO_3$, and their dependence on fabrication parameters. *Lightwave Technology, Journal of*, 12(5):862–871, 1994.

[115] Y. Shizhuo. Fabrication of high-aspect-ratio submicron-to-nanometer range microstructures in $LiNbO_3$ for the next generation of integrated optoelectronic devices by focused ion beams (FIB). *Microwave and Optical Technology Letters*, 22 (6):396–398, 1999.

[116] C. Restoin, S. Massy, C. Darraud-Taupiac, and A. Barthelemy. Fabrication of 1D and 2D structures at submicrometer scale on lithium niobate by electron beam bombardment. *Optical Materials*, 22(3):193 – 199, 2003.

[117] H. Hu, A. P. Milenin, R. B. Wehrspohn, H. Hermann, and W. Sohler. Plasma etching of proton-exchanged lithium niobate. *Journal of Vacuum Science and Technology A: Vacuum, Surfaces, and Films*, 24(4):1012–1015, 2006.

[118] L. Gui, B. Xu, and T. Chong Chong. Microstructure in lithium niobate by use of focused femtosecond laser pulses. *Photonics Technology Letters, IEEE*, 16(5): 1337–1339, 2004.

[119] M.-J. Li, M. De Micheli, Q. He, and D. B. Ostrowsky. Cerenkov configuration second harmonic generation in proton-exchanged lithium niobate guides. *Quantum Electronics, IEEE Journal of*, 26(8):1384–1393, 1990.

[120] S. Nouh, A. C. Cino, P. Aschieri, P. Baldi, M. P. De Micheli, D. B. Ostrowsky, and K. El Hadi. Proton exchanged waveguides in $LiNbO_3$ and $LiTaO_3$ for integrated lasers and nonlinear frequency converters. *Optical Engineering*, 37(4):1193–1202, 1998.

[121] A. Méndez, G. de la Paliza, A. García-Cabañes, and J.M. Cabrera. Comparison of the electro-optic coefficient r_{33} in well-defined phases of proton exchanged $LiNbO_3$ waveguides. *Applied Physics B*, 73(5-6):485–488, 2001.

[122] R. H. Nielsen and G. Wilfing. *Zirconium and Zirconium Compounds*. Wiley-VCH Verlag GmbH & Co. KGaA, 2000.

[123] K. El Hadi. *Interactions paramétriques dans des guides d'ondes réalisés par échange protonique sur niobate de lithium polarisé périodiquement*. PhD thesis, Université Nice Sophia Antipolis, 1996.

[124] Yu. N. Korkishko, V. A. Fedorov, and S. M. Kostritskii. Optical and x-ray characterization of $H_xLi_{1-x}NbO_3$ phases in proton-exchanged $LiNbO_3$ optical waveguides. *Journal of Applied Physics*, 84(5):2411–2419, 1998.

[125] A. Boudrioua, J. C. Loulergue, F. Laurell, and P. Moretti. Nonlinear optical properties of (H^+, He^+)-implanted planar waveguides in z-cut lithium niobate:

annealing effect. *ournal of the Optical Society of America B*, 18(12):1832–1840, 2001.

[126] S. M. Kostritskii, S. V. Rodnov, Yu. N. Korkishko, V. A. Fedorov, and O. G. Sevostyanov. Electro-optical properties of different $H_xLi_{1-x}NbO_3$ phases in proton-exchanged $LiNbO_3$ waveguides. *Ferroelectrics*, 440(1):47–56, 2012.

[127] S. M. Kostritskii, Yu. N. Korkishko, V. A. Fedorov, M. V. Proyaeva, and E. A. Baranov. Spontaneous polarization and nonlinear susceptibility in various protonated $H_xLi_{1x}NbO_3$ phases. *Technical Physics*, 47(1):74–79, 2002.

[128] J. Olivares and J. M. Cabrera. Modification of proton exchanged $LiNbO_3$ layers for guiding modes with ordinary polarization. *Fiber and Integrated Optics*, 12(3): 277–285, 1993.

[129] T. Wang, D. Mantha, and R. G. Reddy. Thermal stability of the eutectic composition in $LiNO_3$:$NaNO_3$:KNO_3 ternary system used for thermal energy storage. *Solar Energy Materials and Solar Cells*, 100(0):162 – 168, 2012. Photovoltaics, Solar Energy Materials, and Technologies: Cancun 2010.

[130] P. K. Tien and R. Ulrich. Theory of prism-film coupler and thin-film light guides. *Journal of the Optical Society of America*, 60(10):1325–1337, Oct 1970.

[131] S. Monneret, P. Huguet-Chantôme, and F. Flory. M-lines technique: prism coupling measurement and discussion of accuracy for homogeneous waveguides. *Journal of Optics A: Pure and Applied Optics*, 2(3):188, 2000.

[132] R. Petit and M. Cadilhac. Electromagnetic theory of prism coupler (tutorial approach). *Journal of Optics*, 8(1):41, 1977.

[133] P. K. Tien, R. Ulrich, and R. J. Martin. Modes of propagating light waves in thin deposited semiconductor films. *Applied Physics Letters*, 14(9):291–294, 1969.

[134] P. K. Tien and R. J. Martin. Experiments on light waves in a thin tapered film and a new light-wave coupler. *Applied Physics Letters*, 18(9):398–401, 1971.

[135] J. M. White and P. F. Heidrich. Optical waveguide refractive index profiles determined from measurement of mode indices: a simple analysis. *Applied Optics*, 15 (1):151–155, Jan 1976.

[136] P. K. Tien. Integrated optics and new wave phenomena in optical waveguides. *Reviews of Modern Physics*, 49:361–420, 1977.

[137] L. G. Ferreira and M. A. A. Pudensi. Waveguiding in a dielectric medium varying slowly in one transverse direction. *Journal of the Optical Society of America*, 71 (11):1377–1380, 1981.

[138] H. Wang and J. Hurtado-Ramos. Guided waves in thin films consisting of tilted columns deposited on anisotropic substrates: excited by a birefringent coupler. *Pure and Applied Optics: Journal of the European Optical Society Part A*, 5(2): 239, 1996.

[139] R. Baets, P. Kaczmarski, and P. Vankwikelberge. Design and modelling of passive and active optical waveguide devices. In JohnH. Marsh and Richard M. Rue, editors, *Waveguide Optoelectronics*, volume 226 of *NATO ASI Series*, pages 21–71. Springer Netherlands, 1992.

[140] E. A. J. Marcatili. Dielectric rectangular waveguide and directional coupler for integrated optics. *Bell System Technical Journal*, 48(7):2071–2102, 1969.

[141] G. Tittelbach, B. Richter, and W. Karthe. Comparison of three transmission methods for integrated optical waveguide propagation loss measurement. *Pure and Applied Optics: Journal of the European Optical Society Part A*, 2(6):683, 1993.

[142] R. Regener and W. Sohler. Loss in low-finesse Ti:$LiNbO_3$ optical waveguide resonators. *Applied Physics B*, 36(3):143–147, 1985.

[143] W. Sohler and H. Suche. Frequency conversion in Ti:$LiNbO_3$ optical waveguides. In *Proceedings of SPIE*, volume 0408, pages 163–171, 1983.

[144] C. Sheppard, J. Gannaway, R. Kompfner, and D. Walsh. The scanning harmonic optical microscope. *Quantum Electronics, IEEE Journal of*, 13(9):912–912, 1977.

[145] R. Carriles, D. N. Schafer, Kraig E. Sheetz, Jeffrey J. Field, R. Cisek, V. Barzda, A. W. Sylvester, and J. A. Squier. Invited review article: Imaging techniques for harmonic and multiphoton absorption fluorescence microscopy. *Review of Scientific Instruments*, 80(8), 2009.

[146] J. F. McGilp. A review of optical second-harmonic and sum-frequency generation at surfaces and interfaces. *Journal of Physics D: Applied Physics*, 29(7):1812, 1996.

[147] M. L. Bortz, L. A. Eyres, and M. M. Fejer. Depth profiling of the d_{33} nonlinear coefficient in annealed proton exchanged $LiNbO_3$ waveguides. *Applied Physics Letters*, 62(17):2012–2014, 1993.

[148] M. Flörsheimer, R. Paschotta, U. Kubitscheck, C. Brillert, D. Hofmann, L. Heuer, G. Schreiber, C. Verbeek, W. Sohler, and H. Fuchs. Second-harmonic imaging of ferroelectric domains in $LiNbO_3$ with micron resolution in lateral and axial directions. *Applied Physics B*, 67(5):593–599, 1998.

[149] I. I. Smolyaninov, H. Y. Liang, C. H. Lee, and C. C. Davis. Local crystal analysis using near-field optical second harmonic microscopy: Application to thin ferroelectric films. *Journal of Applied Physics*, 89(1):206–211, 2001.

[150] J. Kaneshiro, Y. Uesu, and T. Fukui. Three-dimensional observations of $LiNbO_3$ and $LiTaO_3$ quasi-phase matching devices using transmission-type scanning second-harmonic generation interference microscope. *Japanese Journal of Applied Physics*, 48(9):09KF09, 2009.

Abstract

Up to now a tight optical confinement in waveguides realized on $LiNbO_3$ was always achieved to the detriment of the nonlinear properties of the substrate. The present work aimed to develop and to study a new method of waveguide fabrication, High Index Soft Proton Exchange (HISoPE), which allows realizing highly confining waveguides in $LiNbO_3$ ($\delta n_e = 0.1$). Characterizations by localized SHG experiments showed that the nonlinear properties of the HISoPE waveguides are not destroyed, but modes with high propagation loss were observed for planar HISoPE waveguides on Z-cut wafers. These losses can be eliminated by performing the exchange in more acidic bath, but this results in more important deformations in channel waveguides and in the hybrid nature of the propagating modes. In the frame of the project PhoXcry, we tried to realize a highly efficient electro-optical modulator by combining photonic crystals and HISoPE waveguides on X-cut wafers of $LiNbO_3$. The losses of the waveguides fabricated on X-cut, attributed to the hybrid nature of the propagating modes, were estimated to be around 1.75 dB/cm. The nanostructured waveguides exhibited high losses and it was not possible to identify clear optical band gap. HISoPE in combination with reverse proton exchange (RPE) showed a great potential for buried waveguide fabrication. We used them in a SHG experiment and despite elevated losses of 2 dB/cm, the conversion efficiency was estimated as high as $160\%\,W^{-1}cm^{-2}$. A directional coupler behavior was observed in the buried waveguides due to different RPE kinetics in different parts of the waveguide. A further development of the HISoPE+RPE process will improve the quality of the buried waveguides.

Keywords: Proton exchange, Nonlinear optics, Integrated optics, Lithium niobate

Résumé

Jusqu'à présent, un fort confinement optique dans des guides d'onde réalisés sur LiNbO3 n'a pu être obtenu qu'au détriment des propriétés non linéaires du substrat. Le présent travail visait à développer et à étudier une nouvelle méthode de fabrication des guides d'onde, "High Index Soft Proton Exchange" (HISoPE), qui permet de réaliser des guides d'onde trs confinés ($\delta n_e = 0.1$). Des caractérisations en génération d'harmonique localisée ont montré que les propriétés non linéaires de ces guides ne sont pas détruites mais les guides HISoPE réalisés sur coupe Z peuvent présenter des modes ayant des pertes élevées. Ces pertes peuvent être éliminés en utilisant des bains plus acides pour l'échange, mais cela implique des déformations plus importante dans les guides d'onde canal et la nature hybride des modes propageant. Dans le cadre du projet PhoXcry, nous avons essayé de réaliser un modulateur électro-optique trs efficace en combinant des cristaux photoniques et des guides HISoPE sur coupe X. Dans les meilleurs guides d'onde fabriqués sur coupe X, les pertes à la propagation, expliquées par la nature hybride des modes sont de 1.75 dB/cm, mais dans les guides d'ondes nanostructurés il n'a pas été possible d'identifier clairement une bande interdite photonique. HISoPE en combinaison avec l'échange protonique inverse (Reverse Proton Exchange, RPE) a montré un grand potentiel pour la fabrication de guides d'onde enterrés. Dans une expérience de SHG et malgré des pertes élevées de 2 dB/cm, nous avons pu estimer une efficacité de conversion de 160% $W^{-1}cm^{-2}$. Un comportement du coupleur directionnel a été observé dans les guides d'onde enterrés fabriqué en raison d'une cinétique RPE différente dans les différentes parties du guide d'onde. Un développement ultérieur de la méthode HISoPE+RPE devrait permettre d'améliorer sensiblement la qualité des guides enterrés.

Mots-clés : Echange protonique, Optique non linéaire, Optique Intégrée, Niobate de lithium